Modeling of Fatigue Behavior in Fillet Welded Connections in Lightweight Ship Structures

by

Shizhu Xing

A dissertation submitted in partial fulfillment
of the requirements for the degree of
Doctor of Philosophy
(Naval Architecture and Marine Engineering)
in The University of Michigan
2016

Doctoral Committee:

Professor Pingsha Dong, Chair
Assistant Professor Matthew Collette
Associate Professor Jason P. McCormick
Professor Yinlu Young.

Acknowledgement

First and foremost, I would like to express my sincere gratitude to my advisor Prof. Pingsha Dong for the continuous support of my Ph.D. study and related research, for his patience, motivation, and immense knowledge. His guidance helped me in all the time of research and writing of this thesis. I could not have imagined having a better advisor and mentor for my Ph.D. study.

Besides my advisor, I would like to thank the rest of my thesis committee: Prof. Yinlu Young, Prof. Matthew Collette, and Prof Jason P. McCormick., for their insightful comments and encouragement.

My sincere thanks also go to my pre-coworker Alina Shrestha for the great help while we were working together on lots of fatigue tests. Also, I would like to thank all my colleagues in our group for the stimulating discussions.

Last but not the least, I would like to thank my family for supporting me spiritually throughout writing this thesis and my life in general.

Table of Contents

List of Figures

List of Tables

List of Symbols

(Chapter 1)

s	fillet weld size
t	base plate thickness
R_1	the ultimate tensile strength of weaker plate
R_2	the ultimate transverse shear strength of weld metal
θ	angle between a failure plane and horizontal weld leg plane

(Chapter 2)

a_θ	weld throat size along a hypothetical cut angle
f	fatigue life scaling factor
$f_{x'}$	line force in x' direction
$f_{y'}$	line force in y' direction
$f_{z'}$	line force in z' direction
$m_{z'}$	line moment about z'
$m_{y'}$	line moment about y'
$f_{\theta y'}$	line force in y' direction at a hypothetical cut angle
$f_{\theta x'}$	line force in x' direction at a hypothetical cut angle
$m_{\theta z'}$	line moment about z' at a hypothetical cut angle
p	weld penetration
r	bending ratio

r^A	bending ratio corresponding to weld toe failure
r^B	bending ratio corresponding to weld root failure
s	fillet weld size (weld leg length)
t	thickness of intercostal plate
t_e	effective crack path length
t_e^A	crack path length corresponding to weld toe failure
t_e^B	crack path length corresponding to weld root failure
x_i'	local coordination of node i
$F_{x'i}, F_{y'i}$	nodal forces at node i in local coordinate system
T	thickness of continuous plate
$I(r)$	dimensionless life integral as a function of bending ratio r
σ_N	total normal traction stress
σ_m	membrane component of normal traction stress
σ_b	bending component of normal traction stress
$\sigma_N(\theta)$	analytical expression of total normal traction stress
$\sigma_m(\theta)$	analytical expression of membrane component of normal traction stress
$\sigma_b(\theta)$	analytical expression of bending component of normal traction stress
$\sigma_e(\theta)$	analytical expression of effective traction stress
$\Delta\sigma_e$	effective traction stress range
$\Delta\sigma_b$	bending component of normal traction stress range
$\Delta\sigma_m$	membrane component of normal traction stress range

$\Delta\sigma_e^A$	effective traction stress range corresponding to weld toe failure
$\Delta\sigma_e^B$	effective traction stress range corresponding to weld throat failure
ΔS_s	equivalent traction stress range
ΔS_s^A	equivalent stress range corresponding to weld toe failure
ΔS_s^B	equivalent stress range corresponding to weld root failure
ΔS_n	nominal stress
τ_T	transverse shear traction stress
τ_L	longitudinal shear traction stress
τ_m	membrane component of transverse shear traction stress
τ_{Lm}	membrane component of longitudinal shear traction stress
τ_{Lb}	bending component of longitudinal shear traction stress
$\tau_T(\theta)$	analytical expression of transverse shear traction stress
θ	angle between a hypothetical cut and horizontal weld leg plane
θ_c	critical failure angle

(Chapter 3)

c_A , c_B	constants associated with dimensions of structural members
$d(X)$	displacement due to griping
e	axial misalignment
$e(X)$	updated eccentricity after griping
k_e	axial misalignment-induced SCF for lab specimen
k_α	angular misalignment-induced SCF for lab specimen

$k_{e+\alpha}$	total SCF for lab specimen
l	constant length dimension
m	reaction moment due to fatigue loading
m_1, m_2	moment distribution under fatigue loading
p	fatigue loading
r	bending ratio
s	fillet weld size
t	thickness of specimen
t_e	effective thickness
t_1, t_2, t_3, t_4	thickness of structural members
v	reaction shear force due to fatigue loading
A	section area of specimen
A_1, A_2, A_3, A_4	area of cross section of structural members
E	Young's modulus
F	dummy force
I	moment of inertia of cross section of test specimen
I_1, I_2, I_3, I_4	moment of inertia of cross section of structural members
$I(r)$	dimensionless life integral as a function of bending ratio r
L	total length of specimen
L_c	coordinate of critical location
L_1, L_2, L_3, L_4	length of structural members
M	reaction moment due to gripping

M_I , M_{III} , M_{IV}	reaction moments
M_1 , M_2 , M_3 , M_4	moment distribution along structural members
P_{III} , P_{IV}	reaction tensile forces
P_1 , P_2 , P_3 , P_4	axial force distribution
U	potential energy
$U_{bending}$	potential bending energy
$U_{tensile}$	potential tensile energy
V	reaction shear due to gripping
V_I , V_{III} , V_{IV}	reaction shear forces
X	location of dummy force
α	angular misalignment
σ_b	misalignment induced bending stress
σ_p	membrane stress due to fatigue loading
σ_{p1}	membrane stress in structural member 1
κ	scaling parameter
$\Delta\sigma_b$	structural bending stress range
$\Delta\sigma_m$	structural membrane stress range
$\Delta\sigma_s$	structural stress range
ΔS_s	equivalent structural stress
$\Delta\sigma_p$	nominal stress range

(Chapter 4)

a	crack size

a'	relative crack size a/t
a_i'	initial crack size
a_f'	final crack size
f_1 , .. f_n	line forces
$f_{y'}$	line forces in y' direction
$f_m(a'),\ \ f_b(a')$	dimensionless compliance functions
h	slope of S-N curve
m	slope of $da/dN-\Delta K$ curve
$m_{x'}$	line moment about x'
n_i	loading cycles of the i^{th} loading block
s	fillet weld size
t	base plate thickness
t_c	thickness correction
t_e	effective thickness
$A(a_i', a_f', r, C)$	a constant
C	a constant
F_1 , .. F_n	nodal forces
F_{xi}	nodal forces in x direction
M_1 , .. M_n	nodal moments
N	fatigue life
R	radius of TIG weld shape

σ_m	structural membrane stress
σ_b	structural bending stress
σ_s	normal stress
τ_L	in-plane shear stress
τ_T	transverse shear stress
ΔK	stress intensity factor
$\Delta\sigma_b$	structural bending stress range
$\Delta\sigma_m$	structural membrane stress range
$\Delta\sigma_s$	structural stress range
$\Delta\sigma_e$	effective stress range
$\Delta\sigma_{e-i}$	effective stress range wrt i^{th} loading block

(Chapter 5)

e	axial misalignment
p	weld penetration
$p\left(\frac{s}{t}\right)$	probability of a developing weld toe cracking
s	fillet weld size
t	base plate thickness
N^A	fatigue life of weld toe cracking
N^B	fatigue life of weld root cracking
R	load ratio
α	angular misalignment

β_0 , β	coefficient to be determined

Abstract

Fillet welded connections are most commonly for construction of marine structures that are often subjected to various forms of cyclic loading in service. Due to its complexity in stress concentration, today's fatigue design rules are empirical and mostly based on test data from 1970's, often resulting in significantly oversized welds or overwelding. As structural lightweighting becomes increasingly important, there is an urgent need for more quantitative fatigue-based fillet weld sizing criterion.

In this work, by taking advantage of recent developments in mesh-insensitive method for dealing with stress singularity at weld root and weld toe, a closed-form weld throat traction stress solution has then been developed for analytically determining weld throat stress state as a function of weld throat plane angle. This closed form solution enables a formulation of an equivalent traction stress parameter that can be used to determine the critical fillet weld size that separates weld root failure mode from weld toe failure mode. In dealing with fatigue test specimens produced in representative shipyard production environment, it is found that both weld penetration and joint misalignments must be taking into account in order to effectively interpret fatigue test data generated as a part of this study. Along this line, the analytical traction stress method developed is further expanded to take into account of weld penetration and joint misalignments. In the latter, a series of new analytical solutions for calculating stress concentration factors caused by joint misalignments are developed. With these new developments, analytically determined fatigue failure mode transition in terms of relative weld

fillet size with respect to base plate thickness is proposed and validated by fatigue test data. Then, a quantitative weld sizing is proposed based on a detailed data analysis through a logistic regression method.

Aluminum fillet-welded cruciform specimens are also considered for confirming the applicability of the failure mode transition criteria developed based on steel weldments. Non-load carrying fillet-welded cruciform specimens are also tested and analyzed using the traction stress method for developing baseline information for supporting the development of fatigue design curve for titanium hull structures.

Chapter 1
Introduction

1.1 Research Background

1.1.1 Fillet Welded Connections and Fatigue Failure Modes

In ship and offshore structures, fillet welded connections (or fillet joints) are common for connecting secondary structures to main structures as illustrated in Figure 1.1 a typical mid-ship of bulk carrier. Fillet welded connections are classified into two categories i.e. load carrying joints (Figure 1.2a) and non-load carrying joints (Figure 1.2b) based on load transfer considerations. For load-carrying cruciform joints (Figure 1.2a), a fatigue crack may initiate at either weld toe or weld root, depending upon loading conditions and fillet weld size. The fatigue crack which initiates at weld toe and propagates through the loaded plate thickness is termed as weld toe cracking (Figure 1.2a), and the one which initiates at weld root and propagates through the weld metal is referred to as weld root cracking (Figure 1.2a). Moreover, for a non-load-carrying cruciform joint (Figure 1.2b), there is only one possible fatigue cracking mode i.e. weld toe cracking since the fillet welds do not carry any remote load carried by the continuous member.

Weld root fatigue cracking mode has always been a concern in design and analysis of load-carrying fillet welded connections. The reason is that fatigue lives associated with weld root cracking tend to be significantly lower than that associated with weld toe cracking under the same nominal loading [1], which can be attributed to the fact

that defects are often trapped at weld root in addition to inherent variability in weld throat size and penetration status among other factors. The other reason is that weld root cracking mode is particularly challenging for performing fatigue evaluation since most of the existing fatigue evaluation procedures based on nominal stress or surface extrapolation based hot spot stress methods are not applicable for treating weld root cracking. As discussed by Hobbacher [2], "the hot spot stress method is limited to the assessment of the weld toe".

1.1.2 Existing Fillet Weld Sizing Criteria

Fillet weld sizing criteria for load-carrying connections has remained the same since 1970's both for commercial and military applications. For instance, fillet weld sizing for naval ships has been based on MIL-STD-1628 [3], which was developed based on static shear strength testing using standard transverse and longitudinal shear fillet-welded specimens. The design equation is given as:

$$\frac{s}{t} = \frac{R_1}{1.414R_2} \tag{1.1}$$

where *s* is fillet weld size, *t* is weaker plate thickness, R_1 is the ultimate tensile strength of weaker plate, and R_2 is the ultimate transverse shear strength of weld metal. The failure plane is presumed along the shortest weld throat ($\theta = 45^\circ$ see Figure 1.3). In 1984, Krumpen and Jordan [4] proposed six shear equations considering two loading conditions (longitudinal and transverse) and assumed three failure planes i.e. the shortest weld throat $\theta = 45^\circ$ and two heat affected zones with respect to $\theta = 0^\circ$ and $\theta = 90^\circ$. These six shear equations have been adopted by AWS [5] as fillet weld sizing criteria. Recently, Nie and Dong [6] has proven that the most potential static shear failure plane is the weld throat

plane with respect to $\theta = 22.5^{\circ}$ (see Figure 1.3) instead of $\theta = 45^{\circ}$ for conventional shear strength test specimen under transverse loading. It was then validated by Lu et al. [7] via a large amount of static shear test. This suggests that the empirical assumption $\theta = 45^{\circ}$ may cause unfavorable fillet size design. This is one of the issues for current fillet weld sizing criteria. The other one is that fillet sizing equations e.g. Eq. (1.1) are solely based on static strength without considering fatigue behavior of fillet joints i.e. avoiding weld root fatigue cracking. The latter is what this study focuses on.

To our best knowledge, a quantitative fatigue-based fillet weld sizing criterion for preventing weld root fatigue cracking has not been established yet. However, there exists a great deal of experimental evidence [e.g. 8-12] that once a fillet weld size reaches beyond a critical size, fatigue failure mode tends to transition from weld root cracking mode to weld toe cracking mode. Thus, to prevent weld root cracking from occurring, both design and shop floor practices tend to encourage oversized welds as discussed recently by Nie and Dong [6] and Huang et al. [13]. Huang et al. [13] also reported that there is no upper limit for oversized fillet welds for quality assessment. Oversized weld severely increases weight, materials cost, and welding induced distortion, especially for lightweight ship structure.

In recent years, to achieve higher payload, faster-sailing speed, and reduction of fuel consumption, an increase of application of lightweight ship structure in both civilian and military vessels has been evident [14-16]. Huang et al. [15-16] reported that the light weight, thinner gauge, and high strength materials are increasingly utilized in ship structure construction to reduce topside weight. From 1990 to 2000, the thinner gauge (*10mm* or less) plate has risen to 90%. For lightweight ship construction, welding induced

distortion is the major challenge since the thinner gauge plate has much less distortion resistance. Overwelding causes severe distortion problem (see Figure 1.4). Huang et al. [15] also reported that an estimation of 30% of ship building fabrication costs can be attributed to rework to reduce the distortion caused by welding (Figure 1.4), for using the thinner gauge and high strength plate. Therefore, it is in urgent to develop a quantitative fatigue-based fillet sizing criterion, based on fatigue failure mode transition (from weld root cracking to weld toe cracking), beyond which weld root cracking is deemed as impossible.

1.2 Noted Research Efforts on Fatigue Failure Mode Transition

In pursuing an improved fillet weld sizing criterion, there have been numerous studies [e.g. 8-9] in the past. Gurney [8] suggested a family of curves that relate critical weld size to base metal plate thickness, derived by equating the fatigue lives of weld toe cracking to weld root cracking based on fracture mechanics calculations. The results [8] suggest that the critical relative weld size *s/t* (*s* denotes weld leg size and *t* denotes plate thickness) varies with base plate thickness and relative weld penetration to plate thickness ratio. For instance, the critical relative weld size (*s/t*) varies from *0.85-1.1* as base plate thickness varies from *10mm-50mm* without considering the weld penetration.

Recently, Maddox [9], after performing a review of fatigue performance of fillet welds, proposed a relationship of optimum fillet weld size (*s/t*) and plate thickness by equating the fatigue life of weld toe failure (DNV Class F3 [17]) and weld root failure (DNV Class W3, [17]). The results indicate that the optimum weld size increases as plate thickness decreases, which is contradictory to Gurney's findings [8] as illustrated in Figure 1.5.

Furthermore, Gurney [8] assumed the crack initiated at weld root propagating along the vertical weld leg i.e. $\theta = 90^{\circ}$ (see Figure 1.2a) without any theoretical or experimental evidence. Maddox [9] used nominal stress based S-N curves for evaluating the critical weld size. Obviously, nominal stress can not characterize the weld throat stress state. Then, the critical weld sizes provided in both Refs. [8-9] are questionable to be considered as a design reference.

1.3 Major Challenges

1.3.1 An Effective Stress Definition

As briefly mentioned in Sec. 1.1.1, both nominal stress method and hot spot stress method are not applicable for weld root cracking analysis. Then, one of the major challenges for investigating the fatigue failure mode transition becomes to find and adopt a proper effective stress definition and associated calculation method for consistently characterizing the stress state relevant to both weld root fatigue cracking behavior and weld toe fatigue cracking behavior.

1.3.2 Critical Weld Root Cracking Plane

To precisely determine the fatigue failure mode transition point, the critical failure plane of weld root cracking mode is essential to be determined first. However, most of the researchers [e.g. 8-12] intuitively assumed vertical leg plane [8-10, 12] with respect to $\theta = 90^{\circ}$ (see Figure 1.2) as failure plane, or assumed the shortest weld throat plane [11] with respect to $\theta = 45^{\circ}$. This will result in unexpected errors on the determination of critical weld size based on failure mode transition. Due to complex stress state at weld root, determination of critical failure plane is a challenging task.

1.3.3 Weld Penetration

The weld penetration effect on fatigue failure mode transition had been investigated by numerous researchers [e.g. 8, 10]. In Refs. [8, 10], weld penetration is only treated as a reduction of initial crack size. However, weld penetration might also influence critical root cracking plane and stress state associated to weld toe cracking. To investigate fatigue failure mode transition, weld penetration effects have to be comprehensively studied.

1.3.4 Joint Misalignments

Jakubczak and Glinka [18] noticed that axial misalignments had much more influence on weld toe cracking than on weld root cracking. More importantly, an increase in axial misalignment seemed to promote failure mode transition from weld root cracking to weld toe cracking for similar fillet weld sizes. The failure mode transition due to axial misalignment was then observed in their experimental study [18] using a set of cruciform specimens designed in the same weld size ($s/t \approx 1.0$), but with various amount of axial misalignments.

Due to poor fit-up conditions prior to or welding induced distortions during welding assembly, load carrying fillet welded connections are very prone to both axial and angular misalignments. Then, joint misalignment effect on fatigue failure mode transition has to be taken into account while investigating fatigue failure mode transition behavior in fillet welded connections in lightweight ship structures. However, the major challenge is that no effective misalignment-induced SCF solutions are available for demonstrating and interpreting joint misalignment effect.

1.3.5 Comprehensive Experimental Study

In addition to the theoretical study, a comprehensive experimental study is also essential for understanding and validating theoretical findings. However, there are no comprehensive tests available in the literature. Most of the researchers [e.g. 8-12] focus on theoretical studies. Therefore, a large amount of fatigue testing has to be carried out using load-carry fillet joints (see Figure 1.2a) reflecting typical shop floor practices in lightweight ship construction. Then, choosing effective test data analysis methods is also crucial for making the best use of test results to facilitate the development of fillet sizing criterion.

1.4 Objectives of this research

With knowing the issues and needs in lightweight ship construction, we are motivated to investigate fatigue failure mode transition behavior from weld root cracking to weld toe cracking in load carrying fillet welded connections, and develop comprehensive fatigue based fillet sizing criteria. To achieve the objectives, the challenges and hurdles summarized in the previous section have to be dealt with. Then, the following tasks need to be accomplished:

- Introduce an effective stress definition, which can consistently characterize weld throat stress and weld toe stress.
- Determine critical weld root cracking plane taking advantage of the adopted effective stress definition.
- Identify the weld penetration effect on stress state relevant to both weld root cracking mode and weld cracking mode. Investigate weld penetration effect on fatigue failure mode transition.

- Propose an analytical solution method for evaluating misalignment-induced SCFs, and investigate the misalignment effect on fatigue failure mode transition.
- Perform a comprehensive fatigue testing, and choose effective test data analysis procedures to validate the theoretical findings and facilitate developing fatigue-based fillet sizing criterion.

1.5 Outline of Present Work

The five tasks proposed in Sec. 1.4 are addressed in four chapters in this thesis. A traction based structural stress definition is first introduced in Chap. 2. Then, an analytical weld throat stress model is proposed, and a closed-form solution is developed for characterizing the weld throat stress state. Using the closed-form weld throat stress solution, weld penetration can be directly introduced in, and then the critical weld root cracking plane can be analytically determined for a given joint geometry and weld penetration. Furthermore, two traction stress based failure mode transition criteria are then examined and compared with experimental test data.

Chapter 3 presents an analytical misalignment-induced SCF solution method by means of a potential energy formulation. With such a solution method, misalignment-induced SCFs can be precisely evaluated for both as-assembled structures and lab specimens. The effectiveness of proposed solution method is then validated by both FE solutions and by interpreting fatigue test data.

In Chapter 4, Non-load carrying fillet-welded cruciform titanium specimens are tested and analyzed using the traction stress method for investigation into fatigue behavior and developing baseline information and for supporting the development of

fatigue design curve for titanium hull structures.

In Chapter 5, with the closed-form weld throat stress solution and misalignment-induced SCF solutions developed in Chapter 2 and Chapter 3, both weld penetration and joint misalignment effects are incorporated into fatigue failure mode transition analysis. A theoretical critical weld size is then determined considering measured weld penetrations and joint misalignments. It is validated by the fatigue life based test data analysis result. Furthermore, the same set of data is analyzed by logistic regression method. As a result, the probability for developing weld toe cracking can be estimated for a given fillet weld size. In addition, fatigue failure mode transition behaviors among different materials such as steels, aluminum alloys, and titanium alloys are also discussed. Finally, comprehensive quantitative fatigue-based fillet weld sizing criteria are proposed in conjunction with all the results from theoretical analysis and test data analysis.

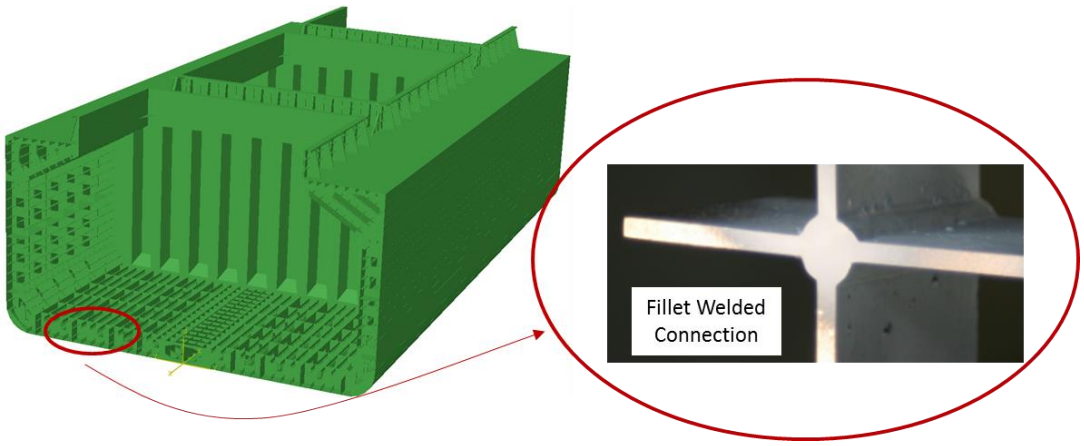

Figure 1.1: Fillet welded connections in a typical bulk carrier ship structures

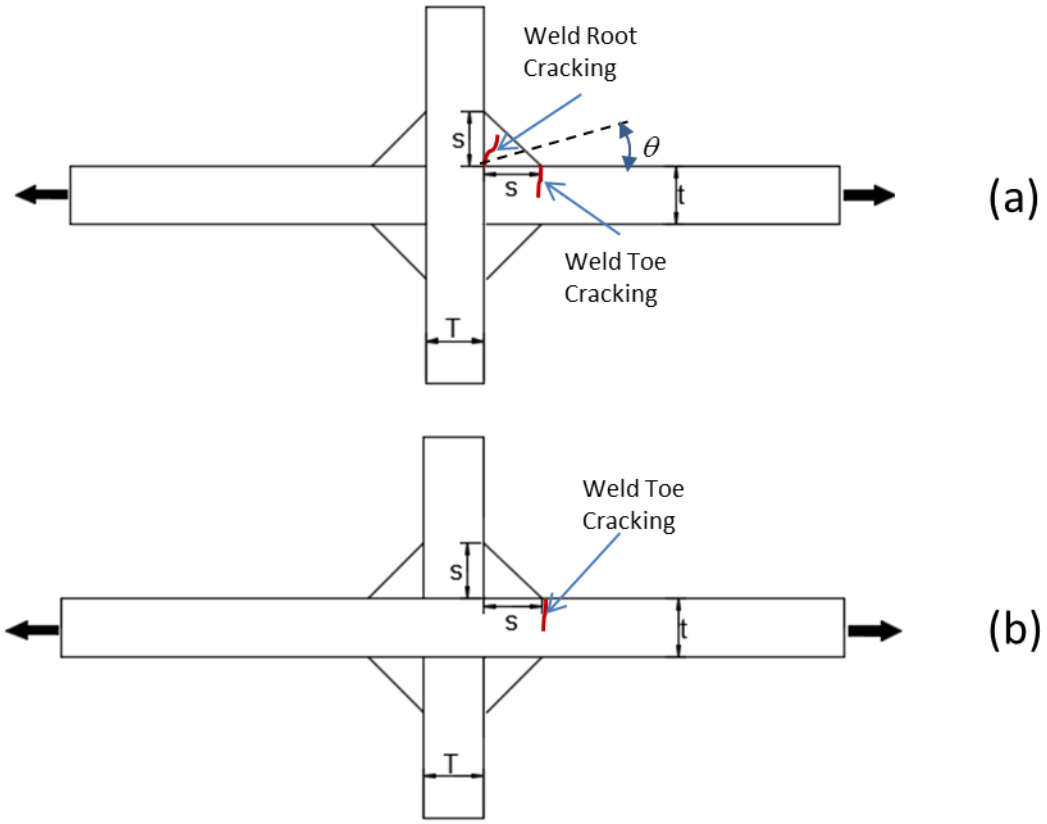

Figure 1.2: Fillet welded connections: (a) load-carrying cruciform joint; (b) Non-load-carrying cruciform joint

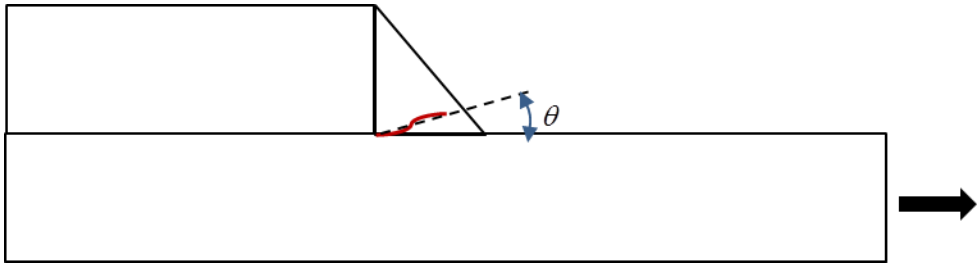

Figure 1.3: Static shear failure angle on conventional shear strength testing specimen

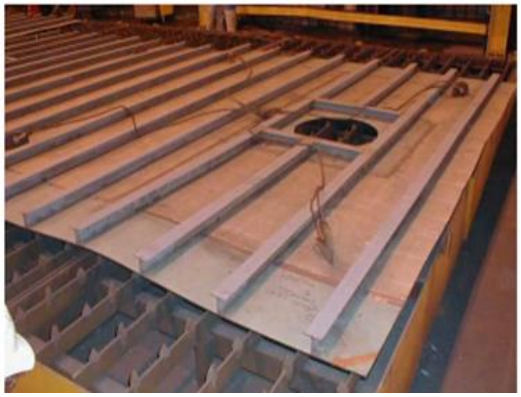

Figure 1.4: welding-induced distortion on a ship panel

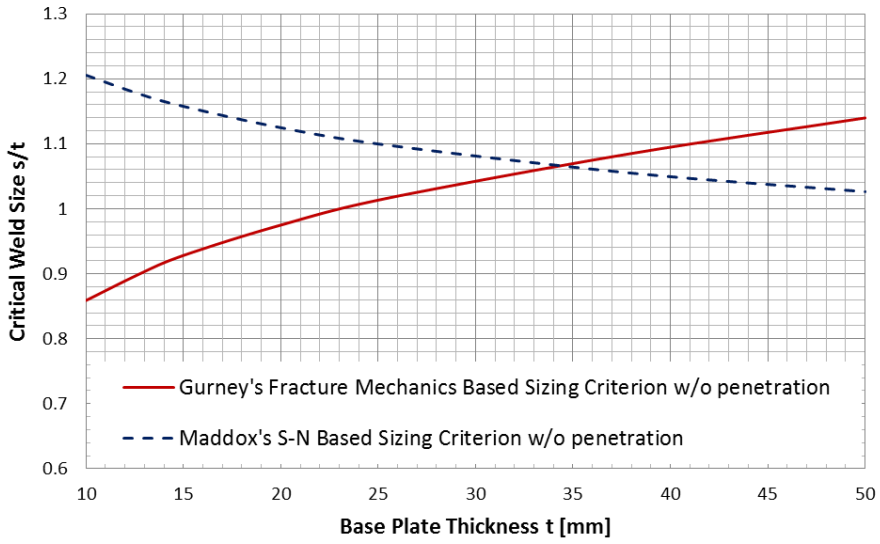

Figure 1.5: Comparison of critical weld size criterion by Gurney and Maddox

References

[1] BS7608, British Standard. "Code of practice for fatigue design and assessment of steel structures." British Standards Institution (1993).

[2] Hobbacher, Adolf, ed. Fatigue design of welded joints and components: Recommendations of IIW Joint Working Group XIII-XV. Woodhead Publishing, 1996.

[3] MIL-STD-1628. 1974 Department of Defense Test Method: Fillet Weld Size, Strength, and Efficiency Determination, June 28

[4] Krumpen, R. P., and C. R. Jordan. "Reduced fillet weld sizes for naval ships." Welding Journal 63.4 (1984): 34-41.

[5] AWS Design Handbook for Calculating fillet weld size

[6] Nie, Chunge, and Pingsha Dong. "A traction stress based shear strength definition for fillet welds." The Journal of Strain Analysis for Engineering Design 47.8 (2012): 562-575.

[7] Lu, Hanqing, Pingsha Dong, and Srimanth Boppudi. "Strength analysis of fillet welds under longitudinal and transverse shear conditions." Marine Structures 43 (2015): 87-106.

[8] Gurney, Timothy Russell. Fatigue of welded structures. CUP Archive, 1979.

[9] Maddox, Stephen J. "Status review on fatigue performance of fillet welds." Journal of Offshore Mechanics and Arctic Engineering 130.3 (2008): 031006.

[10] Noblett, J. E., and R. M. Andrews. "A stress intensity factor solution for root defects in fillet and partial penetration welds." Fatigue: Core Research from TWI (2000): 120.

[11] Hong, Jeong K. "Evaluation of weld root failure using battelle structural stress method." Journal of offshore mechanics and Arctic engineering 135.2 (2013).

[12] Kainuma, Shigenobu, and Takeshi Mori. "A study on fatigue crack initiation point of load-carrying fillet welded cruciform joints." International Journal of Fatigue 30.9 (2008): 1669-1677.

[13] Huang, T. D., et al. "Reduction of Overwelding and Distortion for Naval Surface Combatants, Part 1: Optimized Weld Sizing for Lightweight Ship Structures." Journal of Ship Production and Design 30.4 (2014): 184-193.

[14] Noury, P., et al. "Lightweight construction for advanced shipbuilding–recent development." Det Norske Veritas, Norway (2002).

[15] Huang, T. D., et al. "Fabrication and engineering technology for lightweight ship structures, part 1: distortions and residual stresses in panel fabrication."Journal of ship production 20.1 (2004): 43-59.

[16] Huang, T. D., et al. "Engineering and production technology for lightweight ship structures, Part II: Distortion mitigation technique and implementation."Journal of ship production 23.2 (2007): 82-93.

[17] DNV, Det Norske Veritas. "Recommended practice DNV-RP-C203 fatigue design of offshore steel structures." (2005).

[18] Jakubczak, H., and G. Glinka. "Fatigue analysis of manufacturing defects in weldments." International journal of fatigue 8.2 (1986): 51-57.

Chapter 2
Analysis of Fatigue Failure Mode Transition in Load-Carrying Fillet-Welded Connection

Abstract

In load-carrying fillet welded connections, two distinct fatigue failure modes are possible depending upon fillet weld leg size and loading conditions. One is weld toe cracking through base plate thickness and the other is through weld metal, often referred to as weld root cracking. Based on a recent comprehensive fatigue testing program in support of construction of lightweight ship structures, this paper examines a number of stress based fatigue parameters that can be used to formulate an effective criterion for determining failure mode transition from weld root to weld toe. A closed form solution has been developed for analytically determining the weld throat critical plane on which a traction stress based fatigue parameter attains its maximum and can be compared with that corresponding to weld toe cracking. It is found that both an effective weld throat stress based criterion by combining normal and shear traction stresses and an equivalent effective stress based criterion based on the master S-N curve formulation can be used for the determination of the minimum fillet weld leg size beyond which weld toe fatigue failure dominates. The proposed fillet weld sizing criteria are then validated using a large amount of fatigue test data on load-carrying cruciform fillet welded specimens.

Keywords: Load-carrying fillet welds; traction stresses; finite element; weld root cracking; weld toe cracking; fatigue failure

2.1 Introduction

Fatigue crack development through weld metal originating at weld root, often referred to as weld root cracking or throat cracking, has always been a concern in design and analysis of load-carrying fillet welded connections [1-8]. Such a fatigue failure mode should be avoided for a number of reasons. Chief among them are: (a) Fatigue lives associated with weld root cracking tend to be significantly lower than that associated with weld toe cracking, which can be attributed to the fact that defects are often present at weld root, in addition to inherent variability in weld throat size and penetration status among other factors [5, 6]; (b) Weld root cracking is particularly problematic for computer-based structural fatigue life evaluation since most of the existing fatigue analysis procedures, such as nominal stress and hot spot stress methods [9-13], are not developed for treating throat cracking, as discussed by Dong et al. [14-15]. There exists a great deal of experimental evidence that once a fillet weld size reaches beyond a critical size, fatigue failure mode tends to transition from weld root to weld toe failure [3, 5-6]. As a result, to prevent weld root cracking from occurring, both existing weld sizing criteria and shop floor practices tend to encourage over-sized welds as discussed recently by Nie and Dong [16] and Huang et al. [17], among others.

As structural light-weighting receives an increasing attention in recent years, particularly for some military applications (Huang [17] and Dong et al. [18]), eliminating over-welding in construction of high-performance and lightweight structures has been identified as a key problem area for mitigating welding-induced buckling distortions in thin plate structures. Then, the question becomes: how to quantitatively determine what minimum fillet weld size is needed to ensure, with a reasonable confidence level, that fatigue crack would not occur in weld metal. Being able to determine such a critical weld

size would provide a theoretical basis for establishing proper weld sizing criteria for use in both structural design and shop floor monitoring in construction for avoiding weld oversizing while preventing weld throat fatigue failure mode.

In pursuing an improved fillet weld sizing criterion, there have been numerous studies in the past. Maddox [1] proposed a weld sizing procedure by equating the ratio of weld throat area to base plate area to the fatigue strength ratio (weld root cracking to weld toe cracking) at 2×10^6 cycles to failure. Two assumptions are implied in this approach: one is that weld throat is assumed subjected to a uniform stress state that can be represented by its stress resultant and the other is that fatigue strengths at 2×10^6 cycles are known a priori. In general applications, both assumptions can become questionable. More recently, Maddox [2], after performing a review of fatigue performance of fillet welds, proposed a relationship of optimum fillet weld size and plate thickness by equating the fatigue life of weld toe failure (DNV Class F3 [19]) and weld root failure (DNV Class W3, [19]). The results indicate that the optimum weld size increases as plate thickness decreases.

Gurney [3] suggested a family of curves that relate critical weld size to base metal plate thickness, derived by equating the fatigue lives of weld toe cracking to weld root cracking based on fracture mechanics calculations. The results suggest that the critical relative weld size *s/t* (*s* denotes weld leg size and *t* denotes plate thickness) varies with base plate thickness and relative weld penetration to plate thickness ratio. For instance, the critical relative weld size (*s/t*) varies from *0.85-1.1* as base plate thickness varies from *10mm-50mm* without considering the weld penetration. However, it is important to note that the experimental results reported by Gurney [3] did not show a definite base plate

thickness effect on the critical relative weld size, as his fracture mechanics calculations suggested. Further theoretical and experimental investigations seem needed to clarify the plate thickness effects discussed in [3]. Incidentally, Gurney's experiment results [3] also showed that the critical relative weld size under remote cyclic bending was smaller than that under remote cyclic tension. Using a similar approach, Noblett [4] performed fracture mechanics based crack propagation calculations for both weld toe and weld root cracking in fillet welded specimens under remote cyclic tension and bending. By equating the fatigue lives calculated for weld root cracking and weld toe cracking, the critical relative weld sizes obtained were presented as two set of curves, depending on both base plate thickness and weld penetration. The results indicate that critical relative weld sizes (s/t) vary from 0.875-0.95 for remote cyclic tension, and from 0.53-0.55 for remote cyclic bending, as plate thickness varies from 15*mm*-60*mm*, therefore indicating a rather minor thickness effects in contrast to Gurney's findings [3].

More recently, Lahti et al. [20] studied a series of fillet-welded rectangular hollow section tests and proposed the use of FAT 36 Class design curve in Eurocode for characterizing weld root failure using a nominal stress method. Lotsberg [21] reviewed weld throat fatigue concerns in the context of offshore structures with a focus on tube to plate fillet-welded connections and proposed weld throat nominal stress, also termed as an averaged engineering shear method. However, the proposed method cannot be readily applied for analyzing complex structures since relevant finite element based procedures were not provided. Petinov et al. [22] evaluated a series of ship detail tests exhibiting weld throat failure using fracture mechanics based crack propagation method to correlate test data among different structural details. Along a similar line, Balasubramanian and

Guha [7] investigated a series of cruciform load-carrying fillet welds and suggested that a definition of stress intensity factor at weld root and weld toe should be used for failure mode determination. One major issue with these fracture mechanics based methods is that an initial crack size at weld toe would have to be assumed in order to perform failure mode determination. Kainuma and Mori [6] performed a series of load-carrying cruciform fillet weld specimen testing and fracture mechanics based crack propagation analysis with different fillet sizes and a constant plate thickness of 20*mm*. By defining fatigue strength as the stress range at 2×10^6, the authors proposed a critical fillet weld size to base plate thickness ratio (*s/t*) as 1.2 which corresponds to the intersection point of two calculated fatigue strength curves, of which one represents weld toe failure and the other represents weld throat failure.

Most recently, Hong [8] reported an evaluation of some existing load-carrying fillet weld fatigue test data using a mesh-insensitive structural stress method as discussed by Dong [14-15, 23-26], also referred to as master S-N curve method. Although the results seem promising for S-N data correlation purpose, a weld sizing criterion for determining failure mode transition remains to be addressed. For instance, Hong [8] used an equivalent structural stress based stress concentration factor (SCF) and compared the SCFs at two assumed weld throat sections (i.e., at 45^0 and 90^0) with the SCF at weld toe to qualitatively illustrate the existence of a critical relative fillet weld size. In addition to the fact that critical weld throat plane may very well not be at 45^0, or at 90^0, there are no test data provided for validating the critical weld size illustrated in [8]. More recent investigations into weld root cracking are given by Frick [34] and Turlier et al. [35], but without addressing failure mode transition criteria.

In this study, we start with a traction based stress definition for characterizing weld throat stress state along an arbitrary cut plane originating from weld root, as introduced by Nie and Dong [16] in the context of a general three dimensional load-carrying fillet welded connection. Once three linear traction stress components are obtained using the mesh-insensitive structural stress method as described by Dong et al. [14-15, 23-26], an analytical weld throat stress model is then introduced so that a closed-form solution can be developed for describing traction stress components on any given weld throat plane. With these analytical developments, critical weld throat plane based on a traction stress based fatigue parameter can be precisely determined for a given joint geometry and weld penetration amount. Two traction stress based failure mode transition criteria are then examined and compared with experimental test data obtained from load-carrying fillet welded cruciform specimens involving both weld throat and weld toe failure modes, as fillet size varies. As it turns out, the two criteria are both applicable to fatigue failure mode transition determination purposes, with one being more closely related to a lower bound estimation of critical weld size and the other to an upper bound estimation. Finally, applications of these two criteria in determining critical fillet weld size for preventing weld root cracking in load-carrying connections will be discussed.

2.2 Traction Stress Method for Weld Root Cracking

To examine weld root cracking behavior, a proper stress definition and associated calculation method need to be first introduced for consistently characterizing the stress state relevant to weld root fatigue cracking behaviors as observed in various experimental observations discussed in the previous section. The mesh-insensitive structural stress method, later reframed as a traction stress method by Nie and Dong [16] and Lu and

Dong [27], has been proven effective for correlating static shear strengths in load-carrying fillet welds under both transverse and longitudinal shear loading conditions. It is then natural to examine the applicability of the same stress definition for characterizing weld root fatigue cracking in this work. There are two additional reasons why the traction stress method is considered here. One is that this method is formulated by enforcing equilibrium conditions through the use of relevant nodal forces available from typical FE methods. In doing so, the stress singularity at both weld root and weld toe is suppressed, resulting in mesh-size and mesh-type insensitivity [16] in traction stress determinations at either weld root or weld toe. The second is that the method has already been demonstrated to be effective for correlating a large number of fatigue tests of various component geometries and loading modes into a single master S-N curve and adopted by the 2007 ASME Div2 Code [28] and API 579 RP-1/ASME FFS-1 [29] as discussed in [24-25] for weld toe failure mode.

2.2.1 Traction Stress Definition

Along any hypothetical cut plane emanating from weld root at an angle θ (shown in Figure 2.1a) from the horizontal plate, three traction stress components are exposed, as shown in Figure 2.1b, which are in equilibrium with external loads applied to the horizontal plate. These three components are referred to as normal traction stress σ_N, transverse stress τ_T, and in-plane shear stress τ_L throughout this paper. These traction stresses typically exhibit a complex distribution due to the presence of weld root. As described by Nie and Dong [16], the linear forms of the three traction stress components on the cut plane through weld metal in Figure 2.1 can be extracted in a statically equivalent manner, as depicted in Figure 2.2 and expressed as follows, in terms of their

membrane and bending parts:

$$\sigma_N = \sigma_m + \sigma_b = \frac{f_{y'}}{a_\theta} - \frac{6m_{z'}}{a_\theta^2} \tag{2.1}$$

$$\tau_T = \frac{f_{x'}}{a_\theta} \tag{2.2}$$

$$\tau_L = \tau_{Lm} + \tau_{Lb} = \frac{f_{z'}}{a_\theta} + \frac{6m_{y'}}{a_\theta^2} \tag{2.3}$$

where, $f_{x'}$, $f_{y'}$, $f_{z'}$ are line forces, and $m_{y'}$, $m_{z'}$ are line moments with the local coordinate (x'- y'-z') given in Figure 2.1. The line forces and line moments can be solved by using a matrix equation (Dong [23] and Dong and Nie [16]) with respect to corresponding nodal forces and moments available from typical finite element analysis results along the cut plane shown in Figure 2.1a in a fillet welded component modeled with three dimensional (3D) solid elements with respect to the same local coordinate system. The detailed calculation procedure is given in Dong [23] and Dong and Nie [16].

For the present study in which load-carrying cruciform fillet welded test specimens are considered, only in-plane traction stress components, i.e., normal component σ_N and transverse shear component τ_T are present. Note that the transverse shear stress component τ_T contains only the membrane part, consistent with the transverse shear stress definition in structural mechanics, referred to τ_m hereafter.

2.2.2 Analytical Fillet Weld Model

In order to clearly establish a critical fatigue failure plane on which a stress based fatigue parameter can be extracted and compared with that corresponding to weld toe failure mode, an analytical fillet weld model is proposed here by taking advantage of the

earlier developments presented by Dong [14-15, 23]. Consider the fillet weld of equal fillet size of *s*, but without penetration (*p*) in Figure 2.3a, for which traction stresses ($\sigma_m + \sigma_b$ and τ_m) at $\theta = 90^0$ are already obtained using Eqs.(2.1) and (2.2) in which line forces and moments are solved by a matrix equation given in [16] for the 3D component shown in Figure 2.1a. The traction conditions in terms of line forces ($f_{\theta x'}$, $f_{\theta y'}$) and line moment ($m_{\theta z'}$) on the hypothetical cut plane at any given angle θ must satisfy the equilibrium conditions within the context of elementary structural mechanics theory, resulting in:

$$\sum F_x = 0: \qquad f_{\theta y'} \cdot \sin\theta + f_{\theta x'} \cdot \cos\theta - \sigma_m \cdot s = 0 \tag{2.4}$$

$$\sum F_y = 0: \qquad - f_{\theta y'} \cdot \cos\theta + f_{\theta x'} \cdot \sin\theta + \tau_m \cdot s = 0 \tag{2.5}$$

$$\sum M_z = 0: \qquad - m_{\theta z'} - \frac{\sigma_b s^2}{6} + \frac{\sigma_m s^2}{2} - \frac{f_{\theta y'} a_\theta}{2} = 0 \tag{2.6}$$

in which weld throat size a_θ can be expressed as a function of θ, as:

$$a_\theta = s / \left(\sin\theta + \cos\theta\right)$$

Note that for unequal leg size fillet welds, a_θ expression is given in [16]. Then, the normal traction stress $\sigma_N(\theta)$ in terms of membrane $\sigma_m(\theta)$ and bending $\sigma_b(\theta)$, and $\tau_T(\theta)$ can be analytically expressed as,

$$\sigma_N(\theta) = \sigma_m(\theta) + \sigma_b(\theta) \tag{2.7}$$

$$\sigma_m(\theta) = \frac{f_{\theta y'}}{a_\theta} = \frac{\sigma_m \cdot s \cdot \sin\theta + \tau_m \cdot s \cdot \cos\theta}{a_\theta} \tag{2.8}$$

$$\sigma_b(\theta) = \frac{-6m_{\theta z'}}{{a_\theta}^2} = \frac{\sigma_b s^2 - 3\sigma_m \cdot s^2 + 3a_\theta(\sigma_m \cdot s \cdot \sin\theta + \tau_m \cdot s \cdot \cos\theta)}{{a_\theta}^2} \tag{2.9}$$

$$\tau_T(\theta) = \frac{f_{\theta x'}}{a_\theta} = \frac{\sigma_m \cdot s \cdot \cos\theta - \tau_m \cdot s \cdot \sin\theta}{a_\theta} \tag{2.10}$$

as a function of angle θ. Note that the combined normal stress components has the form of $\sigma_N(\theta) = \sigma_m(\theta) + \sigma_b(\theta)$. The above expressions are also valid for load-carrying fillet weld with a given amount of penetration, designated as *p* in Figure 2.3b, by simply replacing fillet leg size *s* by *s*+*p* in above equations.

2.2.3 Analysis of Fatigue Test Specimens

All fatigue test specimens involved in this study are cruciform load-carrying fillet joints and tested under cyclic tension loading conditions, as shown in Figure 2.4, where *t* represents the loaded base plate thickness, *T* is thickness of the continuous member, and *s* is fillet weld size. As indicated in Figure 2.4b, an equal-leg sized fillet weld is considered here. Base plate length, width and attachment plate height are 300*mm*, 90*mm* and 100*mm*, respectively. A representative two dimensional (2D) cross-section model with symmetric conditions is used as indicated in Figure 2.4b-Figure 2.4c. With such a 2D model, line forces and line moments given in Eq. (2.1)-(2.2) can be further simplified and expressed as :

$$f_{y'} = \sum_{i=1}^{n} F_{y'i} \tag{2.11}$$

$$m_{z'} = \sum_{i=1}^{n} F_{y'i}(x_i' - \frac{a_\theta}{2}) \tag{2.12}$$

$$f_{x'} = \sum_{i=1}^{n} F_{x'i} \tag{2.13}$$

where, $F_{x'i}$, $F_{y'i}$ are the nodal forces at node *i* with respect to the local coordinate system (*x'- y '-z'*) shown in Figure 2.1. The traction stress components on the vertical leg plane ($\theta = 90^0$) are evaluated by submitting Eqs. (2.11)-(2.13) into Eqs. (2.1)-(2.2). Then, the traction stresses at any cut plane within the fillet weld are analytically expressed by Eqs. (2.7)-(2.10). Similarly, traction stresses corresponding to weld toe failure can be calculated in the same manner by setting a cut plane at weld toe into horizontal plate thickness as shown in Figure 2.4 c.

To accommodate the presence of both normal and shear traction stresses, an effective traction stress (ETS) definition proposed by Dong and Hong [30] and Wei and Dong [31] is adopted here and can be expressed as, after inserting component stress expressions given in Eqs. (2.7)-(2.10),

$$\sigma_e(\theta) = \sqrt{\sigma_N{}^2(\theta) + \beta\tau_T{}^2(\theta)} = \sqrt{\begin{array}{l}\left(\begin{array}{l}\left(\sigma_m\cos\theta - \tau_m\sin\theta\right)\left(\cos\theta + \sin\theta\right) + \\ 6\left(\dfrac{\sigma_b}{6} - \dfrac{\sigma_m}{2} + \dfrac{1}{2}\dfrac{\sigma_m\cos\theta - \tau_m\sin\theta}{\cos\theta + \sin\theta}\right)\left(\cos\theta + \sin\theta\right)^2\end{array}\right)^2 \\ + \beta\left(\sigma_m\sin\theta + \tau_m\cos\theta\right)^2\left(\cos\theta + \sin\theta\right)^2\end{array}} \tag{2.14}$$

which has the same functional form as von Mises criterion by taking β=3. However, it should be noted that since fatigue behavior of welded joints is governed by stress range [30-31], all component stresses in the above equation should be replaced by respective component ranges for fatigue data correlation purpose.

The closed form weld throat stress solutions given by Eqs. (2.7), (2.10), and (2.14) are plotted as a function of θ for a load-carrying cruciform specimen with fillet leg size (*s*) to plate thickness (*t*) ratio of *s/t=0.9* in Figure 2.5 (dashed lines). Finite element solutions (symbols) based on the nodal force method [30] along a series of pre-selected cut planes are also shown in Figure 2.5, as a validation for the analytical solutions developed. Note that all stresses shown in Figure 2.5 are normalized by remotely applied stress. Both solutions give essentially the same results for all stress components shown, as one would expect since both solutions are obtained by enforcing equilibrium conditions at a cut plane. However, there are two major disadvantages in the finite element solutions using the nodal force method [30] for the present applications: One is that it requires an elaborate mesh design within the fillet weld so that nodal forces along a set of pre-determined radial lines can be extracted; the other is that those pre-sets radial lines may miss the critical plane on which a relevant stress component (see Eqs. (2.7), (2.9) and (2.10)) reaches its maximum for establishing a failure mode transition criterion from weld root to weld toe stress (see horizontal dash line).

It is interesting to note that both the effective traction stress (σ_e) and normal traction stress (σ_N) attain essentially the same peak values at about $\theta = 70^0$, referred to as θ_c in Figure 2.5. This finding directly contradicts the assumptions made by Gurney [3], Noblett [4] and Kainuma[6] by assuming a critical weld throat failure angle at . .and by Hong by assuming two possible critical weld throat failure angles at $\theta_c = 90^0$ and $\theta_c = 45^0$. The results in Figure 2.5 suggest that this particular load carrying cruciform specimen would very likely develop fatigue failure at weld root through the fillet weld at about $\theta = 70^0$, along which effective traction stress significantly exceeds the stress value at

weld toe (horizontal dashed lines).

It is worth noting that the shear stress is essentially negligible at the angular position where peak values of effective and normal traction stresses occur for the case with relative weld size *s/t=0.9*, shown in Figure 2.5. To examine if this phenomenon is generally true, the analytical solution procedure described above is exercised for various *s/t* ratios of interest in this study. The results are shown in Figure 2.6. It is clear that shear traction stress remains below *4%* of normal traction stresses as *s/t* ratio varying from *s/t=0.4* to *1.6*. Note that the effective traction stress is not shown in Figure 2.6 since it won't be distinguishable from the normal traction stress. Although both effective and normal traction stresses share very similar peak values in cruciform specimens studied here, the effective traction stress definition including shear traction stress should be used since in general shear stress cannot be assumed negligible such as under pure shear or multi-axial loading conditions, as discussed in Dong and Wei [31].

Another interesting finding through the analytical weld throat stress solutions shown in Figure 2.5 is that the maximum transverse shear stress occurs about $\theta = 14^0$ in this type of cruciform specimens, rather than $\theta = 22.5^0$ reported for standard transverse shear specimens by Nie and Dong [16] and Lu and Dong [27]. A detailed comparison for transverse shear traction stresses as a function of θ is given in Figure 2.7. This difference in critical angles as far as transverse shear stress is concerned is due to the presence of vertical restraints by the continuous member of thickness *T* in cruciform specimens while there are no vertical restraints in standard transverse shear specimens at fillet welds. Furthermore, at $\theta = 90^0$ (i.e., along the vertical leg of fillet weld), transverse shear stresses cannot be ignored (see Figure 2.7), as proposed by Hong [8].

2.3 Failure Mode Transition Criteria

Based on the analytical developments presented in Section 2, it seems tempting at this point to suggest the effective traction stress as a criterion for determining under what conditions a fatigue crack would develop from weld root through weld metal, rather than at weld toe or vice versa. Further investigations are warranted, because it is well known that fatigue lives in welded joints exhibit a strong size effect. For weld throat failure, a relevant size parameter is the fillet weld throat size a_θ given in Section 2, depending upon critical failure angle θ_c. In addition, the master S-N curve method [23, 25-26] adopted by various Codes and Standards [28-29] clearly indicates that fatigue lives of welded joints are also related to membrane and bending composition in a traction stress component in addition to size effects. These considerations including weld penetration effects will be addressed in this section in order to arrive at an appropriate fatigue failure mode transition criterion that can be used to determine if a fatigue failure would occur at weld root or weld toe, which is a primary objective of this study.

2.3.1 Effective Traction Stress (ETS)

Naturally, as discussed in Section 2, the effective traction stress given in Eq. (2.14) is a plausible stress definition for establishing a failure mode transition criterion, since it has been used successfully in correlating a large amount of fatigue data tested under multi-axial loading conditions [30-31]. As such, the maximum effective stress and corresponding failure angle θ_c can be evaluated by setting its first derivative with respect to θ being zero, i.e.,

$$\frac{d}{d\theta}\sigma_e(\theta) = 0 \tag{2.15}$$

Since $\sigma_e(\theta)$ is differentiable and possess only one root within the angular section from $\theta = 0^\circ$ to $\theta = 90^\circ$, Eq. (2.15) can be conveniently solved for critical angle θ_c at which $\sigma_e(\theta_c)$ attains its maximum value for each given *s/t* ratio of interest in this study. The full expression of Eq. (2.15) is given in Appendix A for completeness. Note that at each *s/t* value, finite element method using the nodal force method (Eqs. (2.11)-(2.13)) is used to extract traction stresses at $\theta = 90^\circ$. Then Eq. (2.15), through substitution of Eq. (2.14), is completely defined by performing differentiation, as given in Appendix 2-A.

2.3.1.1 Weld with Zero Penetration

The results are summarized in Figure 2.8 for a wide range of *s/t* and *T/t* of interest in this study. It can be seen that ETS based critical failure angle θ_c varies with relative weld size (*s/t*), increasing from $\theta_c = 63^\circ$ at $s/t = 0.4$ to $\theta_c = 73^\circ$ at $s/t = 1.6$, while the corresponding maximum effective stress $\sigma_e(\theta_c)$ rapidly decreases from a normalized value of about *4.5* to about *1*. It is important to note that plate thickness ratio *T/t* has negligible effects on critical failure angle θ_c and no noticeable effects on ETS over the entire range of *s/t* and *T/t* considered. Therefore, both critical plane angle and the resulting maximum effective traction stresses can be argued to be independent, not only, of base plate thickness, but also of the attachment plate thickness (*T*) as long as the relative fillet weld size (*s/t*) is considered. It is worth mentioning here that all past studies [1-4, 6, 8] had not addressed any attachment thickness (*T*) on failure mode transition. From this point on, only cases for *T/t=1* will be considered further, unless otherwise specifically stated.

2.3.1.2 Weld with Penetration

In practice, some level of weld penetration tends to be present in load-carrying fillet-welded connections and can have significant effects on determination of the critical fillet weld size beyond which weld toe failures dominate, as demonstrated by Gurney [3] and Noblett [4] using a fracture mechanics model. As for the fatigue test specimens used in this study, both fillet weld size specification and manufacture of the specimens were based on typical shipyard practices [17], in which weld penetration effects on fillet weld load carrying capacity is not considered for design evaluation purpose. However, the weld penetration effects must be evaluated in order to demonstrate the effectiveness of a proposed weld root failure criterion, particularly for an effective interpretation of test data to be discussed in the next section. Weld macro examinations from samples extracted from the fatigue test specimens used in this study indicate that relative penetration *p/t* varies from *p/t=0* to *p/t=0.4* as to be discussed shortly.

As shown in Figure 2.9, as relative penetration ratio (*p/t*) varies from *0* to *0.4*, critical failure angle θ_c predicted according to effective traction stress definition as a function of *s/t* increases significantly as *p/t* increases, particularly when *s/t* becomes small. The overall trend clearly suggest as penetration ratio *p/t* increases, a critical failure angle becomes increasingly closer to a failure angle of 90^0, as one would intuitively expect. The maximum effective stresses corresponding to critical failure angle θ_c are plotted as a function of relative leg size in Figure 2.10. As the relative penetration *p/t* increases, effective traction stress acting on the critical weld throat plane decreases more significantly (Figure 2.10a) than the stress responsible for weld toe cracking (Figure 2.10b). Therefore, weld penetration can have a significant effect on failure mode

transition from weld root to weld toe cracking.

2.3.1.3 Critical Fillet Weld Size

An effective traction stress based fatigue failure mode transition criterion can be stated as follows:

$$\Delta\sigma_e^A(s/t) \geq \Delta\sigma_e^B(s/t, \theta_c(s/t)) \quad (2.16)$$

where $\Delta\sigma_e^A$ represents the effective traction stress range corresponding to weld toe failure mode (designated as Mode A) as a function of *s/t* and $\Delta\sigma_e^B$ corresponding to weld root failure mode (designated as Mode B) at critical plane angle θ_c. In seeking the critical *s/t* value beyond which Eq. (2.16) is satisfied (i.e., weld root failure mode transitions into weld toe failure mode), both stress parameters in Eq. (2.16) are plotted in Figure 2.11. Two weld penetration cases, *p/t =0* and *0.2*, are considered here, which represent approximate lower and upper bounds for load-carrying fillet weld specimens tested in this study, as discussed in the following section. At *p/t = 0*, weld root cracking (Mode B) along critical weld throat plane dominates when *s/t* ratio is small (i.e., $s/t << 1$) since the effective stress corresponding to weld throat failure is significantly higher than that corresponding to weld toe failure. A theoretical failure transition position (or critical weld size) can be defined as $s/t \approx 1$. Beyond this $s/t \approx 1$, the effective traction stress at weld toe becomes higher than that at weld throat, resulting in dominantly weld toe cracking (Mode A). When an average amount of weld penetration (*p/t = 0.2*) is considered, the theoretical critical weld size is reduced to $s/t \approx 0.7$. Therefore, if a set of fatigue test specimens with weld penetration varying from *p/t =0* to about *0.2*, failure mode transition from weld root cracking to weld toe cracking is expected to occur between *s/t =0.7* and *s/t=1*, if the effective traction stress based criterion (Eq. (2.16) is

considered. Its validation against actual test data will be discussed in the next section. To facilitate test data interpretation, theoretical critical relative weld size (*s/t*) as a function of relative penetration (*p/t*) is given in Figure 2.12, reducing almost linearly as *p/t* increases.

2.3.2 Equivalent Effective Traction Stress (EETS)

It should be noted that the ETS base criterion discussed above is based on the theory of traction stress method [14-15, 23-26] by recognizing the fact that traction stress ranges can be related to fatigue lives. Such a consideration, although reasonable in trend, ignores some other important factors that also contribute to fatigue lives and therefore to failure mode transition behavior. These factors include plate thickness associated with weld toe cracking and weld throat size associated with weld throat cracking, as well as membrane and bending composition along a hypothetical weld throat cut plane.

To do so, it is assumed that the equivalent structural stress parameter defined by Dong et al. [23-26] for demonstrating the existence of a master S-N curve for weld toe cracking can be used here for characterizing weld root cracking. Then, an effective weld throat traction stress range parameter can be written as:

$$\Delta S_s = \frac{\Delta\sigma_e}{t_e^{\frac{2-m}{2m}} I(r)^{\frac{1}{m}}} \tag{2.17}$$

In Eq.(2.17), $\Delta\sigma_e$ represents an effective traction stress range corresponding to either weld root cracking or weld toe cracking, as appropriate, t_e represents crack path length, depending upon failure mode and failure angle, and *m=3.6* is given in [23]. Effects of membrane and bending content on fatigue life are captured in dimensionless polynomial $I(r)^{\frac{1}{m}}$,

$$I(r)^{\frac{1}{m}} = 0.0011r^6 + 0.0767r^5 - 0.0988r^4 + 0.0946r^3 + 0.0221r^2 + 0.014r + 1.2223. \quad (2.18)$$

and membrane and bending content is measured by introducing a bending ratio r, defined as [23]:

$$r = \frac{|\Delta\sigma_b|}{|\Delta\sigma_b| + |\Delta\sigma_m|} \quad (2.19)$$

2.3.2.1 Critical Failure Angle

The EETS based critical failure angle θ_c for weld root cracking can be calculated by setting,

$$\frac{d}{d\theta}\Delta S_s(\theta) = 0 \quad (2.20)$$

in which $\Delta S_s(\theta)$ is given in Eq. (2.17) and $t_e = a_\theta$ as described in section 2.2. Since the bending ratio term $I(r)^{\frac{1}{m}}$ (Eq. (2.18) shows little variation over the angular span containing the critical failure angle, it is treated as a constant in solving Eq. (2.20). Again, Eq. (2.20) is analytically solved and the resulting expression after differentiation is given in Appendix 2-B for completeness.

The resulting critical plane angle θ_c computed for different *s/t* and *p/t* are summarized in Figure 2.13 and corresponding equivalent effective traction stresses (ΔS_s according to Eq. (2.17)) are given at critical angle in Figure 2.14a and at weld toe in Figure 2.14b, respectively. The results share a great deal of similarity with respect to the results shown in Figure 2.9-Figure 2.10 in which effective traction stress $\Delta\sigma_e$ is used. A close examination shows the EETS parameter predicts a somewhat larger critical angle than ETS parameter does under the same *s/t* and *p/t* conditions.

The results shown in Figure 2.9 through Figure 2.14 clearly suggest that weld penetration can have significant effects on weld throat critical failure angle and therefore must be taken into account when interpreting experimental test data. To illustrate this point, a typical macrograph of weld root fatigue cracking from a load-carrying fillet weld cruciform joint after testing, reported by Knight [32], is shown in Figure 2.15. The macrograph indicates a relative fillet $s/t \approx 0.65$ and the penetration $p/t \approx 0.2$. Then, an ETS based failure angle prediction gives $\theta_c \approx 74^\circ$ (see Figure 2.9) and an EETS based failure angle prediction gives $\theta_c \approx 76^\circ$ (see Figure 2.13). The actual failure angles are estimated at $\theta_c \approx 74^\circ$ for the top fillet weld and at $\theta_c \approx 78^\circ$ for the bottom fillet weld, respectively, as shown in Figure 2.15.

2.3.2.2 Critical Fillet Weld Size

An EETS (Eq. (2.17)) based failure mode transition criterion can be stated as:

$$\Delta S_s^A(\Delta\sigma_e{}^A(s/t),\ \mathrm{t}_e{}^A(\mathrm{t}), \mathrm{r}^A(\mathrm{s}/\mathrm{t})) \geq \Delta S_s^B(\Delta\sigma_e{}^B(s/t, \theta_c), t_e{}^B(\mathrm{s}, \theta_c), \mathrm{r}^B(\mathrm{s}/\mathrm{t}, \theta_c)) \qquad (2.21)$$

The criterion stated in Eq. (2.21) can be more clearly illustrated by plotting ΔS_s^A corresponding to weld toe failure (Mode A) and ΔS_s^B corresponding weld root failure (Mode B) along its critical throat plane (θ_c) as shown in Figure 2.17. Two intersection points can be found at $s/t \approx 1.16$ without penetration ($p/t = 0$) and $s/t \approx 0.85$ corresponding to $p/t = 0.2$, respectively. Within the transition region ($s/t \approx 0.85 - 1.16$), Mode A failure mode becomes increasingly dominant over Mode B, as a relative penetration varies from $p/t = 0$ to $p/t = 0.2$.

It is important to note that the EETS based criterion in Eq. (2.21) contains only two terms, i.e., $\mathrm{t}_e{}^A(\mathrm{t})$ and $t_e{}^B(\mathrm{s}, \theta_c)$ that can be identified as a function of t and s,

respectively. Although both terms contribute to EETS shown in Figure 2.16, as *t* and *s* vary, it can be shown that dividing both sides of Eq. (2.21) by $t_e^A(t)$ leads to a combined term $t_e(s/t, \theta_c)$ in place of $t_e^B(s, \theta_c)$ on the right. It then follows that critical relative weld size according to EETS based criterion is independent of any other length dimensions such as weld size or base plate thickness.

2.4 Experimental Study

2.4.1 Test Specimens and fillet size measurements

All fatigue test specimens were manufactured as cruciform load-carrying fillet welded specimens as illustrated in Figure 2.3 by adopting typical shop-floor practices [17] so that the test data reflect typical variability in a typical production environment. A test matrix summarizing specimen details are given in Table 1. Note that base plate and attachment plate are of the same thicknesses (5*mm* and 10*mm*). Specimen width is 90*mm* to ensure sufficient structural restraints to remain full-strength weld residual stresses. To examine weld size effects on failure mode transition, different target (or design) weld fillet sizes (see Table 2-1) were specified on specimen design drawings that were presented to a shipyard production floor [17] which was responsible construction of all test specimens. Further specimen fabrication details can be found in Huang et al. [17].

Actual weld fillet sizes in each test specimen were measured by a laser scanning device prior to fatigue testing. Figure 2.18 illustrates the weld size measurement procedure used in this study with fillet weld definitions for treating actual variations in weld bead shape according to AWS B4 [33]. Each fillet weld in a specimen was measured at four locations along weld length. An averaged leg size over the four positions along each weld is used as the final weld leg size for examining fatigue lives as

a function of relative weld size. Typical variation between target weld size and the measured among four fillet welds (one cruciform specimen) are shown in Figure 2.18b in which the target weld is 8*mm*. Note that all test results from this point on will be presented with respect to an averaged weld size over four measurements over a fillet weld length. Figure 2.19a-Figure 2.19c shows three fillet weld macrographs extracted from weld macro samples cut from each cruciform from which nine fatigue test specimens were extracted including a varying degree of weld penetration *p*.

In fatigue design for filleted welded connections, weld penetration is typically not accounted for due to difficulties in its reliable estimation in practical applications. For the purpose of interpreting fatigue test data in terms failure mode transition, particularly in view of the analytical results discussed in Sec. 2.3.1.2, attempts were made here for estimating an average amount of weld penetration involved in the fatigue specimens involved in this study. In doing so, weld penetration was characterized at two levels in approximate upper and lower bounds on average values of penetration possibly present in test specimens:

(a) At cruciform block level: In manufacturing test specimens, fillet welding was first performed using typical shipyard processes to produce a series of cruciform blocks from which a total of nine cruciform fatigue test specimens were then extracted through cutting process along with one narrow weld macro specimen for examining fillet weld profile as well as the amount of penetration [17]. At such a block level, the weld penetration examined on weld macro specimens (such as those shown in Figure 2.19) serve only as a rough estimate of weld penetration for specimens contained in a block since the nine specimens

extracted from each block can have their own variations both among the nine specimens and within each weld length of slightly longer than 3.5″ (~90*mm*) of a total four fillet welds within each specimen. As a result, the observations on weld macro specimens showed, at block level, that *p/t* can vary from about 0 to about to 0.4.

(b) At specimen level: Each cruciform fillet weld test specimen after exaction from a block described above was then machined to attain a consistent edge condition. Visual examinations were then performed on ends of the four fillet welds in a test specimen to visually examine any presence of anomalies and penetration status. It should be pointed out here that a precise measurement of weld penetration was not possible on such machined surfaces. The intention was to establish a rough indication of weld penetration through these visual examinations. As a result, an averaged penetration among four fillet welds contained in a test specimen can vary approximately from $p/t \approx 0$ to $p/t \approx 0.2$ among all specimens considered, even though the variation at block levels varies from $p/t \approx 0$ to 0.4 from macro specimen to specimen at block level.

2.4.2 Test Procedure

All fatigue tests were performed using an MTS test machine with a load capacity *200 KIPs (890 KN)*, and equipped with MTS 647 Hydraulic wedge grips. Figure 2.20 shows a test specimen in a loaded configuration. In each group of specimens in Table 2-1, one half of the specimens were tested with a remote load range of *30Ksi* (*207MPa*) and the other half with a load range of *60Ksi* (*414MPa*). A stress ratio of *R=-1* was used for all specimens under load-controlled conditions. It should be noted that finite element

calculations under -30Ksi (*-207MPa*) remote stress under minimum possible root gap conditions (about 0.2*mm* through weld macro based measurements) showed that there is no contact occurring along weld root gap. A few pre-test trials indicated that a test frequency of *7-8 Hz* can be used in order to maintain load-controlled conditions while maximizing test efficiency. During testing, both peak load range and displacement range were monitored and recorded. In all test specimens, final failure is defined as when stiffness is reduced by *50%* or complete separation, whichever occurs first.

In addition to documenting cycle to failure for each specimen according to the final failure definition given in the previous section, failure path and origin are carefully examined and documented by separating test data into two failure categories: weld toe failure (Mode A) and weld root failure (Mode B). A representative Mode A failure is illustrated in Figure 2.21a and Mode B failure is shown in Figure 2.21b.

2.4.3 Test Results and Data Analysis

All test data are plotted in terms of fatigue lives (*N*) against measured relative fillet size (s/*t*) in Figure 2.22. Two failure modes, Modes A and B, are identified as square symbols and diamond symbols, respectively. Empty symbols signify test data from *5mm* base plate thickness and filled symbols from *10mm* base late thickness. Figure 2.22a shows the test results for specimens tested under stress range of *30Ksi* (*207MPa*) and Figure 2.22b show the results for specimens tested under nominal stress range *60Ksi* (*414MPa*). The predicted failure mode transition regions corresponding to *p/t=0* and *0.2* according to both ETS and EETS discussed in Section 3 are also superimposed in Figure 2.22.

It can be seen from Figure 2.22 that most weld root failures have relative weld

sizes less than the critical weld size $s/t \approx 1$ according to ETS based without considering weld penetration. The fact that none of weld root failures occur at a relative fillet size beyond $s/t \approx 1.16$, as predicted by the EETS based criterion (without considering penetration) suggests that EETS based criterion is rather conservative. Furthermore, EETS based transition region estimation, i.e., $s/t \approx 0.85-1.16$, seems more reasonably cover the test data transition behavior. A few exceptions (weld toe failures with $s/t < 0.85$) could be attributed to the presence of a larger weld penetration than $p/t \approx 0.2$.

An alternative means of presenting the data in Figure 2.22a and Figure 2.22b can be done by taking advantage of the equivalent traction stress range parameter given in Eq. (2.17), so that different loading conditions and base plate thicknesses can be normalized and plotted in one graph. Then, a fatigue life scaling parameter can be introduced as:

$$f = \left(\frac{\Delta S_n}{(t_s)^{\frac{2-m}{2m}}} \right)^m \tag{2.22}$$

where, ΔS_n is nominal stress, t_s is plate thickness for weld toe cracking and crack path length with respect to critical failure angle for weld root cracking. With this scaling parameter given in Eq. (2.22), the all test data shown in Figure 2.22a and Figure 2.22b can now be presented in one single plot as shown in Figure 2.23. It can be seen that Eq. (2.22) is indeed effective in correlating data with different nominal stress ranges and base plate thicknesses. As a result, the transition behaviors observed in Figure 2.22a and Figure 2.22b can now be more clearly confirmed regardless of applied stress range levels and base plate thickness reflected in the test data. It should be pointed out that the present study covers only two base plate thicknesses, i.e., 5*mm* and 10*mm* and with applied stress ratio of *R=-1*, as specified by sponsor. Further experimental validations with plate

thicknesses beyond 10*mm* may be needed before generalizing the finding on plate thickness effects seen in Figure 2.22. and Figure 2.23can also greatly facilitate statistical analysis of the test data by allowing all test data being treated as one population, which will be reported in a separate publication.

2.5 Conclusions

By taking advantage of the analytical weld throat stress model, two traction stress based failure mode transition criteria, i.e., ETS and EETS, have been examined in detail and compared with a large number of test data involving failure mode transition from weld throat and weld toe failures as fillet weld size varies. The following conclusions can be drawn:

1) The critical weld throat failure plane angle θ_c (with respect to base plate) increases with increasing weld size (*s/t*) and penetration depth (*p/t*) according to both ETS and EETS based criteria. The differences between the two criteria are insignificant, considering inherent variability in fatigue test data.
2) The critical weld size and failure transition region when considering expected variations in weld penetration according ETS seem to provide a good estimation of the lower bound transition behavior of actual test data, while those according to EETS seems to provide a good estimation of the upper bound, see Figure 2.23. Therefore, it is reasonably conservative to adopt the critical weld size according to the EETS based criterion, which gives a critical relative weld size of $s/t = 1.16$ with no penetration ($p/t = 0$) and $s/t = 0.85$ for an averaged relative penetration of $p/t = 0.2$

3) The analytical developments presented in this paper seem to suggest that base plate thickness should not have any noticeable effects on failure mode transition behavior, as long as a relative fillet weld size (s/t) is used, unlike some of the previous studies suggest. However, it should be noted that the present experimental validation effort has been focused on plate thicknesses of 5*mm* and 10*mm* with an applied stress ratio of R=-1. Before generalizing our finding, further validations using test data with plate thickness larger than 10*mm* and applied stress ratio larger than R=0 may be required.

Appendix 2-A: Detailed Expression of Eq. (2.15)

$$\frac{d}{d\theta}\sigma_e(\theta) = \frac{1}{2}\left(2\left(\left(\sigma_m\cos(\theta) - \tau_m\sin(\theta)\right)\left(\cos(\theta) + \sin(\theta)\right) + 6\left(-\frac{1}{6}\sigma_b - \frac{1}{2}\sigma_m - \frac{1}{2}\frac{\sigma_m\cos(\theta) - \tau_m\sin(\theta)}{\cos(\theta) + \sin(\theta)}\right)\left(\cos(\theta) + \sin(\theta)\right)^2\right)\left(\left(-\sigma_m\sin(\theta) - \tau_m\cos(\theta)\right)\left(\cos(\theta) + \sin(\theta)\right) + \left(\sigma_m\cos(\theta) - \tau_m\sin(\theta)\right)\left(-\sin(\theta) + \cos(\theta)\right) + 6\left(-\frac{1}{2}\frac{-\sigma_m\sin(\theta) - \tau_m\cos(\theta)}{\cos(\theta) + \sin(\theta)} + \frac{1}{2}\frac{\left(\sigma_m\cos(\theta) - \tau_m\sin(\theta)\right)\left(-\sin(\theta) + \cos(\theta)\right)}{\left(\cos(\theta) + \sin(\theta)\right)^2}\right)\left(\cos(\theta) + \sin(\theta)\right)^2 + 12\left(-\frac{1}{6}\sigma_b - \frac{1}{2}\sigma_m - \frac{1}{2}\frac{\sigma_m\cos(\theta) - \tau_m\sin(\theta)}{\cos(\theta) + \sin(\theta)}\right)\left(\cos(\theta) + \sin(\theta)\right)\left(-\sin(\theta) + \cos(\theta)\right)\right) + 6\left(\sigma_m\sin(\theta) + \tau_m\cos(\theta)\right)\left(\cos(\theta) + \sin(\theta)\right)^2\left(\sigma_m\cos(\theta) - \tau_m\sin(\theta)\right) + 6\left(\sigma_m\sin(\theta) + \tau_m\cos(\theta)\right)^2\left(\cos(\theta) + \sin(\theta)\right)\left(-\sin(\theta) + \cos(\theta)\right)\Bigg) \Bigg/ \left(\left(\left(\sigma_m\cos(\theta) - \tau_m\sin(\theta)\right)\left(\cos(\theta) + \sin(\theta)\right) + 6\left(-\frac{1}{6}\sigma_b - \frac{1}{2}\sigma_m - \frac{1}{2}\frac{\sigma_m\cos(\theta) - \tau_m\sin(\theta)}{\cos(\theta) + \sin(\theta)}\right)\left(\cos(\theta) + \sin(\theta)\right)^2\right)^2 + 3\left(\sigma_m\sin(\theta) + \tau_m\cos(\theta)\right)^2\left(\cos(\theta) + \sin(\theta)\right)^2\right)^{1/2}$$

Appendix 2-B: Detailed Expression of Eq. (2.20)

$$\frac{d}{d\theta}\Delta Ss(\theta) = \frac{1}{2}\left(\left(\frac{s}{\cos(\theta)+\sin(\theta)}\right)^{-\frac{1}{2}\frac{2-m}{m}}\left(2\left(\left(\cos(\theta)\,\sigma_m-\sin(\theta)\,\tau_m\right)\left(\cos(\theta)+\sin(\theta)\right)+6\left(-\frac{1}{6}\,\sigma_b-\frac{1}{2}\,\sigma_m-\frac{1}{2}\,\frac{\cos(\theta)\,\sigma_m-\sin(\theta)\,\tau_m}{\cos(\theta)+\sin(\theta)}\right)\left(\cos(\theta)+\sin(\theta)\right)^2\right)\left(\left(-\sin(\theta)\,\sigma_m-\cos(\theta)\,\tau_m\right)\left(\cos(\theta)+\sin(\theta)\right)+\left(\cos(\theta)\,\sigma_m-\sin(\theta)\,\tau_m\right)\left(-\sin(\theta)+\cos(\theta)\right)+6\left(-\frac{1}{2}\,\frac{-\sin(\theta)\,\sigma_m-\cos(\theta)\,\tau_m}{\cos(\theta)+\sin(\theta)}+\frac{1}{2}\,\frac{\left(\cos(\theta)\,\sigma_m-\sin(\theta)\,\tau_m\right)\left(-\sin(\theta)+\cos(\theta)\right)}{\left(\cos(\theta)+\sin(\theta)\right)^2}\right)\left(\cos(\theta)+\sin(\theta)\right)^2+12\left(-\frac{1}{6}\,\sigma_b-\frac{1}{2}\,\sigma_m-\frac{1}{2}\,\frac{\cos(\theta)\,\sigma_m-\sin(\theta)\,\tau_m}{\cos(\theta)+\sin(\theta)}\right)\left(\cos(\theta)+\sin(\theta)\right)\left(-\sin(\theta)+\cos(\theta)\right)\right)+6\left(\cos(\theta)\,\tau_m+\sin(\theta)\,\sigma_m\right)\left(\cos(\theta)+\sin(\theta)\right)^2\left(\cos(\theta)\,\sigma_m-\sin(\theta)\,\tau_m\right)+6\left(\cos(\theta)\,\tau_m+\sin(\theta)\,\sigma_m\right)^2\left(\cos(\theta)+\sin(\theta)\right)\left(-\sin(\theta)+\cos(\theta)\right)\right)\Bigg/\left(\left(\left(\left(\cos(\theta)\,\sigma_m-\sin(\theta)\,\tau_m\right)\left(\cos(\theta)+\sin(\theta)\right)+6\left(-\frac{1}{6}\,\sigma_b-\frac{1}{2}\,\sigma_m-\frac{1}{2}\,\frac{\cos(\theta)\,\sigma_m-\sin(\theta)\,\tau_m}{\cos(\theta)+\sin(\theta)}\right)\left(\cos(\theta)+\sin(\theta)\right)^2\right)^2+3\left(\cos(\theta)\,\tau_m+\sin(\theta)\,\sigma_m\right)^2\left(\cos(\theta)+\sin(\theta)\right)^2\right)^{1/2}+\frac{1}{2}\left((2-m)\left(\left(\left(\cos(\theta)\,\sigma_m-\sin(\theta)\,\tau_m\right)\left(\cos(\theta)+\sin(\theta)\right)+6\left(-\frac{1}{6}\,\sigma_b-\frac{1}{2}\,\sigma_m-\frac{1}{2}\,\frac{\cos(\theta)\,\sigma_m-\sin(\theta)\,\tau_m}{\cos(\theta)+\sin(\theta)}\right)\left(\cos(\theta)+\sin(\theta)\right)^2\right)^2+3\left(\cos(\theta)\,\tau_m+\sin(\theta)\,\sigma_m\right)^2\left(\cos(\theta)+\sin(\theta)\right)^2\right)^{1/2}s\left(-\sin(\theta)+\cos(\theta)\right)\right)\Bigg/\left(m\left(\frac{s}{\cos(\theta)+\sin(\theta)}\right)^{\frac{1}{2}\frac{2+m}{m}}\left(\cos(\theta)+\sin(\theta)\right)^2\right)$$

Table 2-1: Cruciform fatigue specimen test matrix

Base plate Materials	Attachment Materials	Welding Process	Weld Wire	Thickness [*mm*]	Target Weld Size [*mm*]
DH-36	DH-36	FCAW	71T1-C	5	3, 5, 8
DH-36	DH-36	FCAW	71T1-C	10	5, 6, 8, 10, 12
HSLA-80	HSLA-80	FCAW	101T-C	5	3, 5, 8
HSLA-80	HSLA-80	FCAW	101T-C	10	5, 6, 8, 10, 12
DH-36	HSLA-80	FCAW	MIL 71T-1C	5	3, 5, 8
DH-36	HSLA-80	FCAW	MIL 71T-1C	10	5, 6, 8, 10, 12
DH-36	HSLA-80	SAW	MIL 100S	5	3, 5, 8
DH-36	HSLA-80	SAW	MIL 100S	10	5, 6, 8, 10, 12

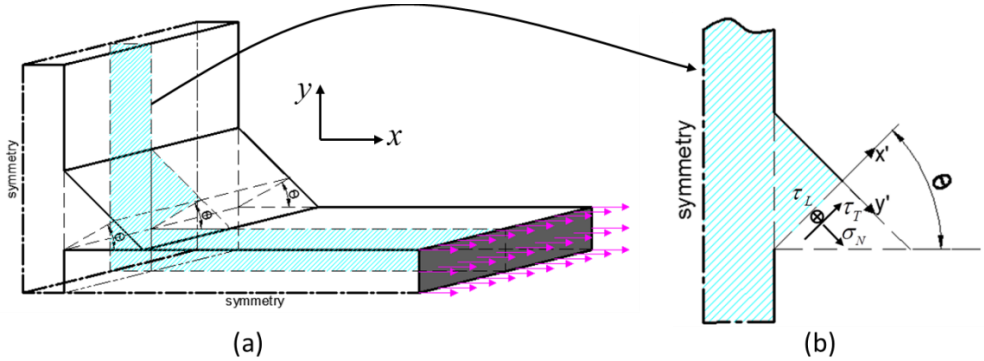

Figure 2.1: Traction stresses on a hypothetical cut plane across fillet weld in a load-carrying fillet weld: (a) A representative cross-section along fillet weld; (b) free body diagram representation after a hypothetical cut through weld root at an angle θ

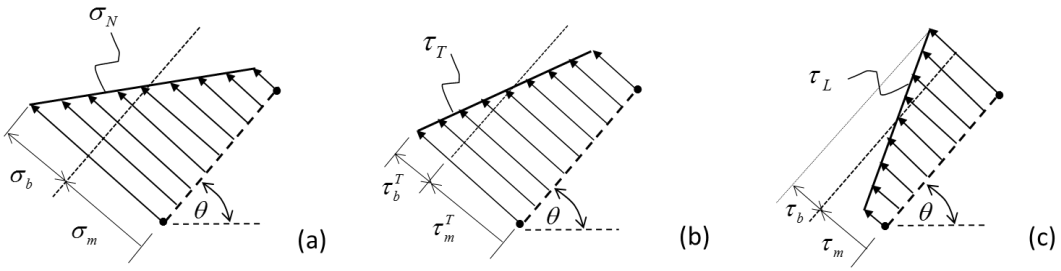

Figure 2.2: Linear representation and decomposition of three traction stress components: (a) linear form of normal component; (b) transvers shear component; (c) in plane shear component

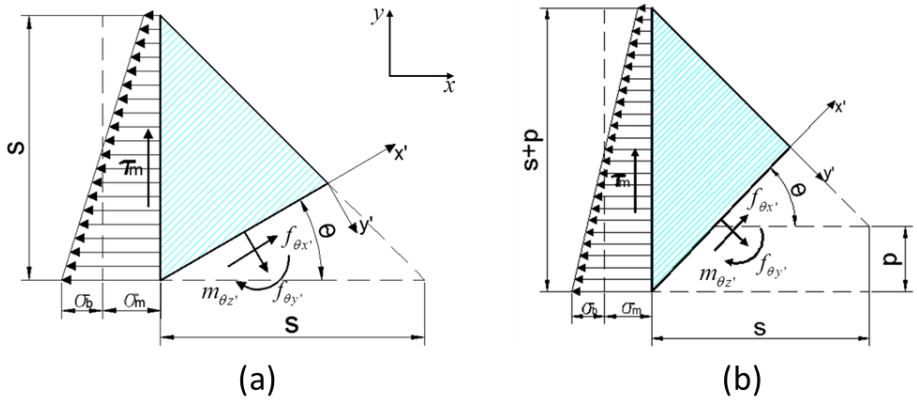

Figure 2.3: Analytical fillet weld model: (a) fillet weld without penetration; (b) fillet weld with penetration, *p*

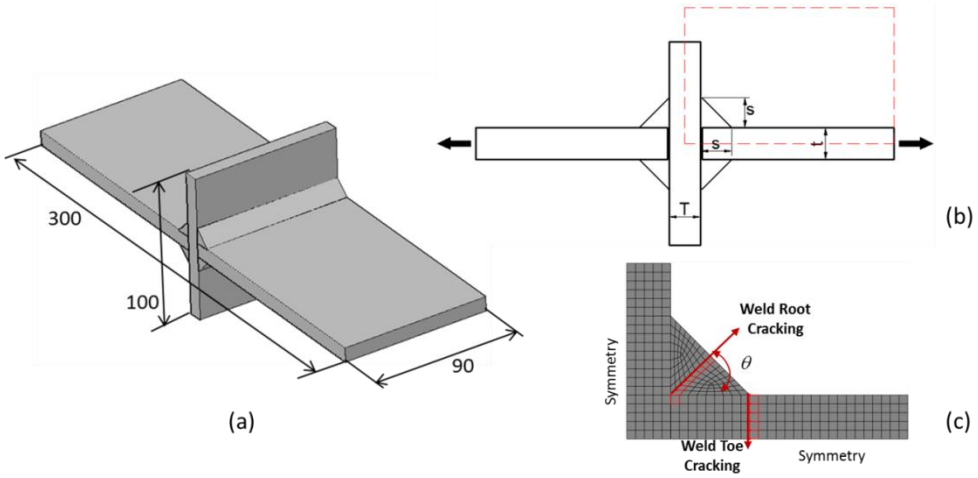

Figure 2.4: Load-carrying cruciform fillet specimen geometry: (a) 3D view; (b) 2D cross section; (c) 2D FE model taking advantage of quarter-symmetries

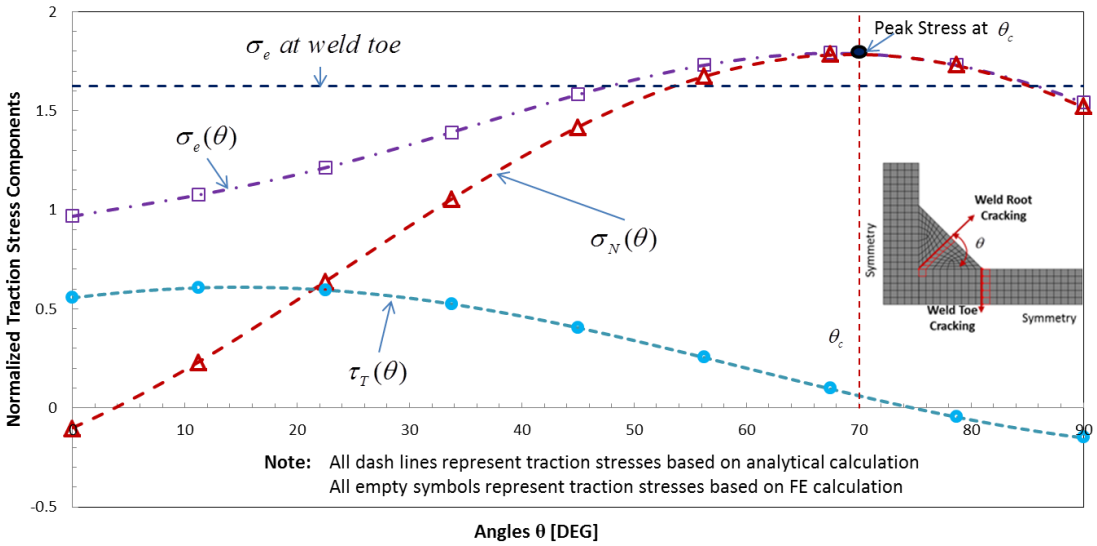

Figure 2.5: Comparison of analytical and finite element (nodal force method) solutions of weld throat effective stress σ_e, normal traction stress or opening stress σ_N, and transverse shear τ_T as a function of θ (*s/t=0.9, t=T*)

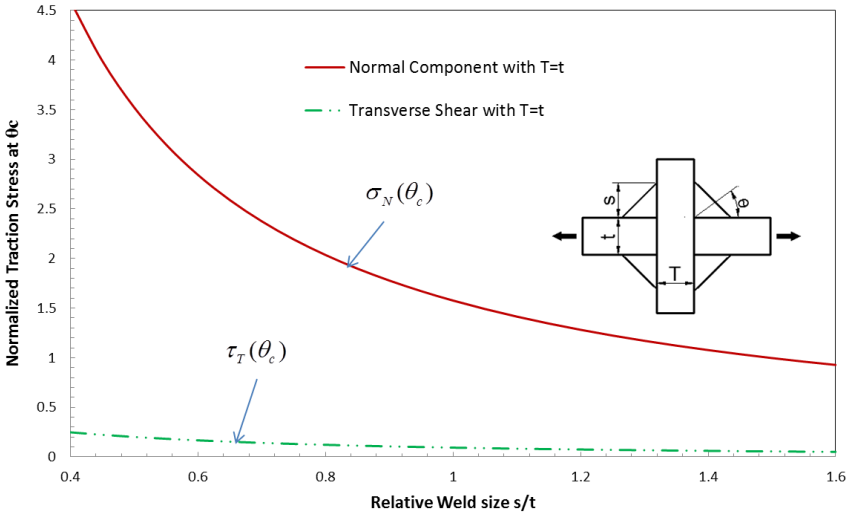

Figure 2.6: Normal and shear traction stresses at critical plane as a function of relative fillet size *s/t*

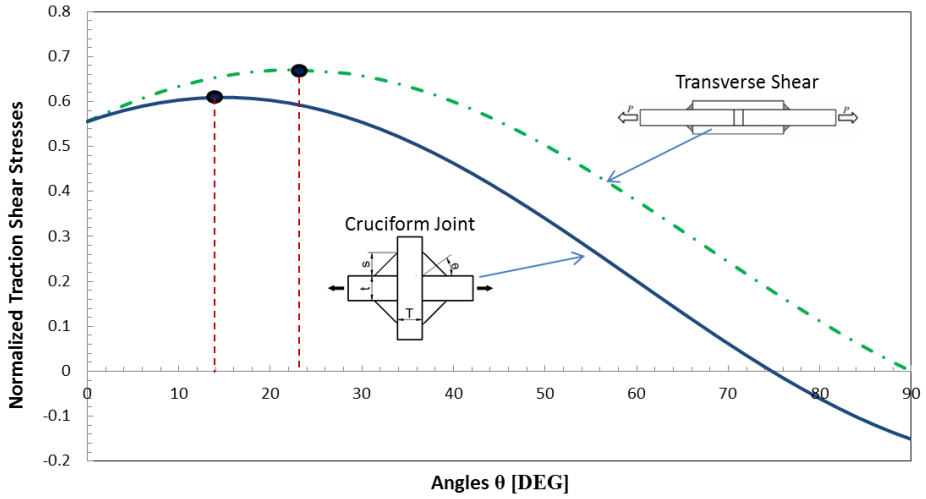

Figure 2.7: Comparison of transverse shear traction stress between cruciform joint and standard transverse shear specimen [16, 27]

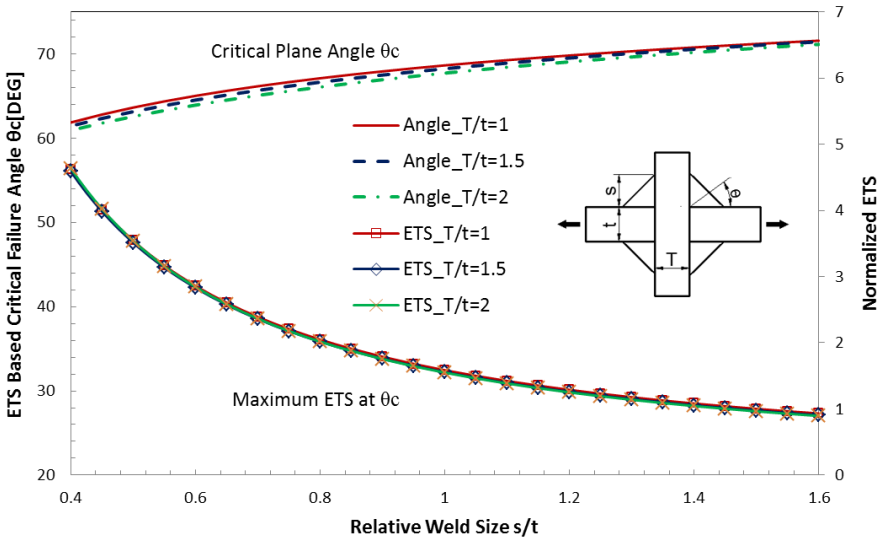

Figure 2.8: Dependency of predicted critical failure angle θ_c and corresponding normalized effective stress (ETS) on *s/t* and *T/t*

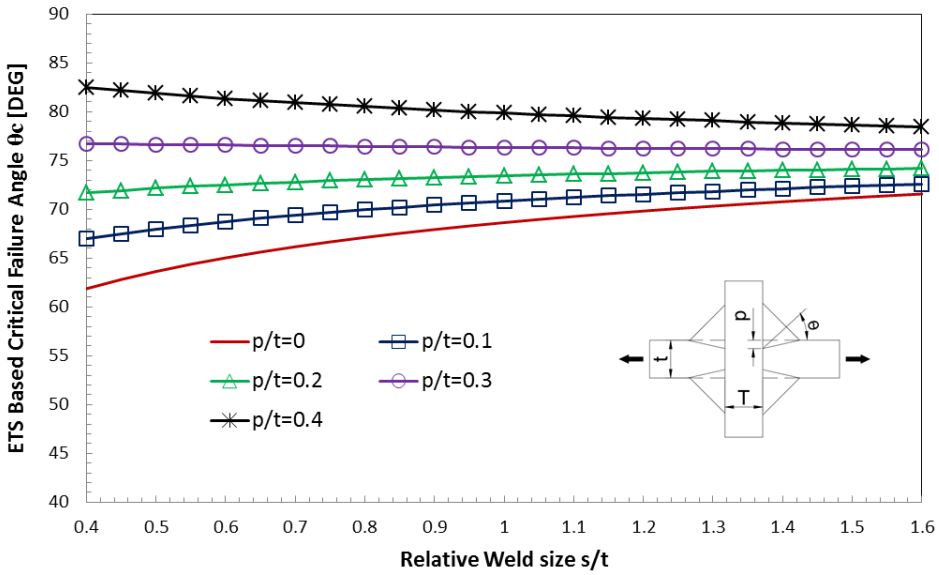

Figure 2.9: Penetration effect on ETS based critical failure angle θ_c

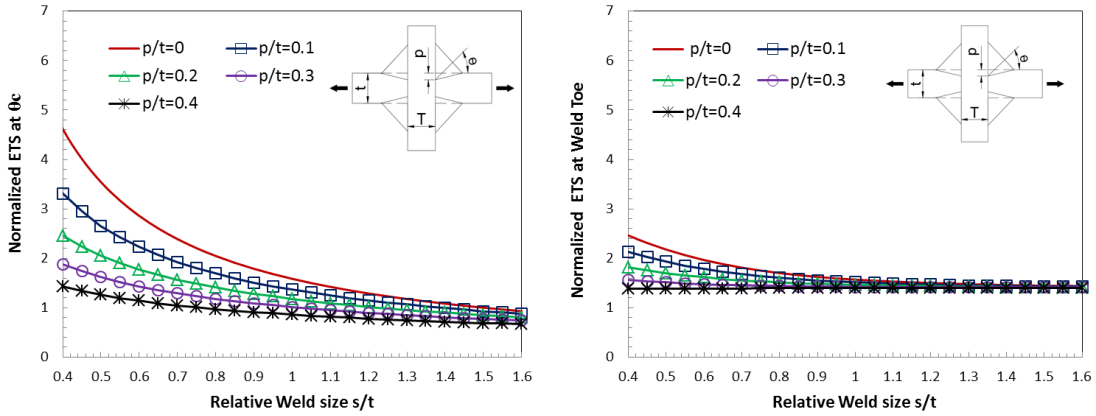

Figure 2.10: Weld penetration effect on ETS: (a) weld throat ETS at θ_c; (b) weld toe ETS

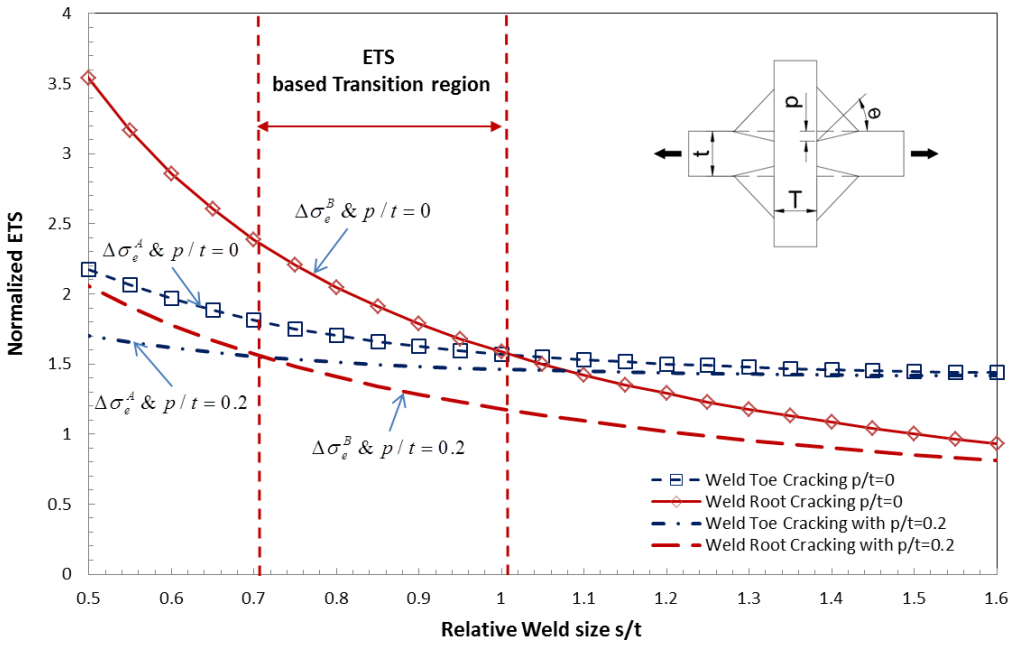

Figure 2.11: ETS based critical weld size as a function of p/t and transition region

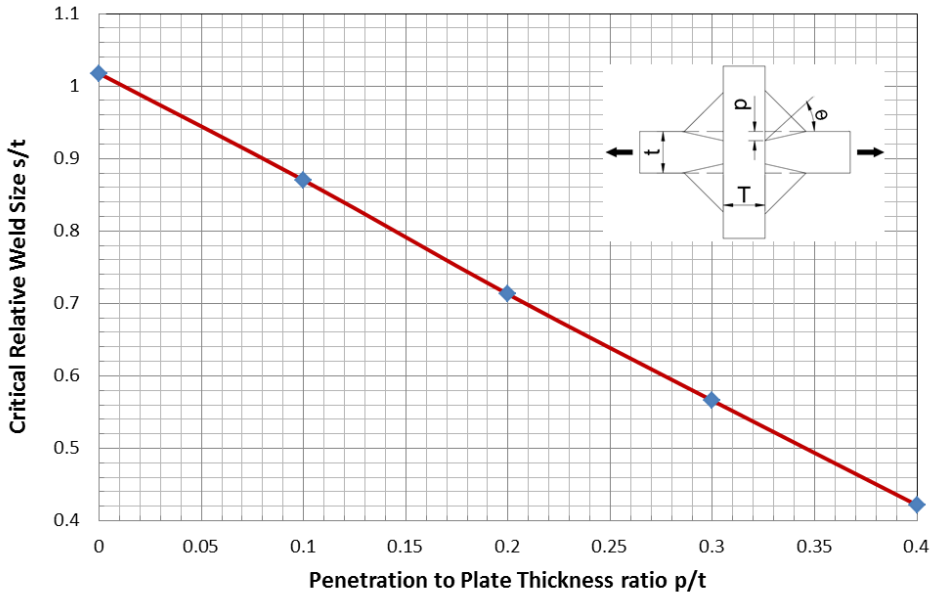

Figure 2.12: Penetration effect on ETS based critical weld size

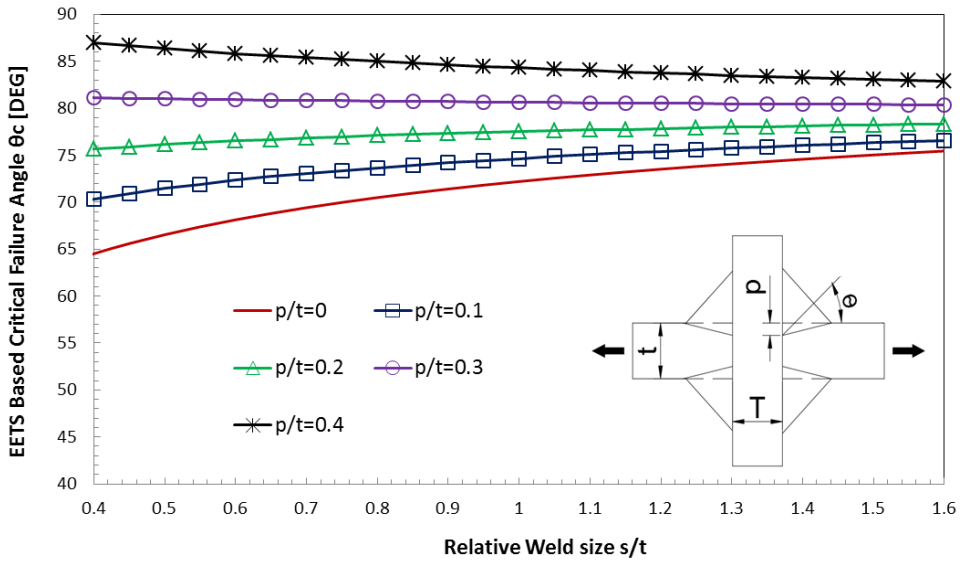

Figure 2.13: Relative weld penetration (*p/t*) effects on critical failure angle predicted according to EETS parameter

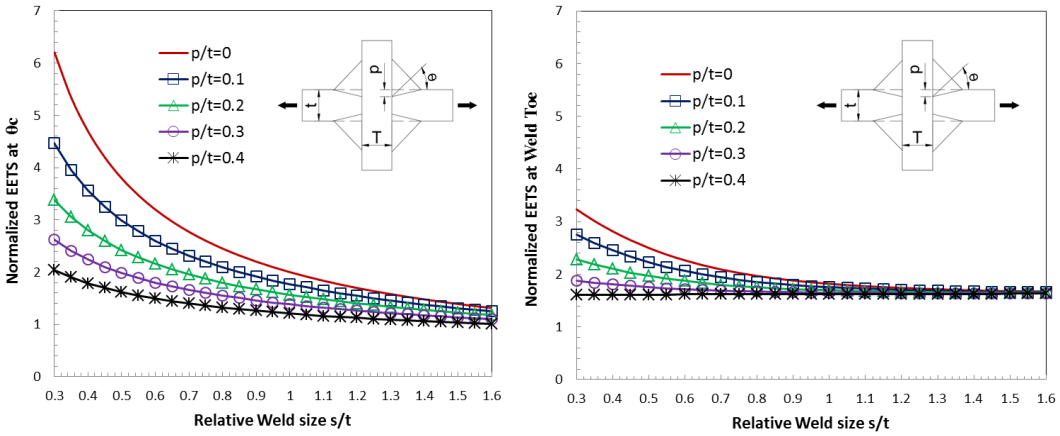

Figure 2.14: Relative weld penetration effect on EETS: (a) weld throat EETS at θ_c; (b) weld toe EETS

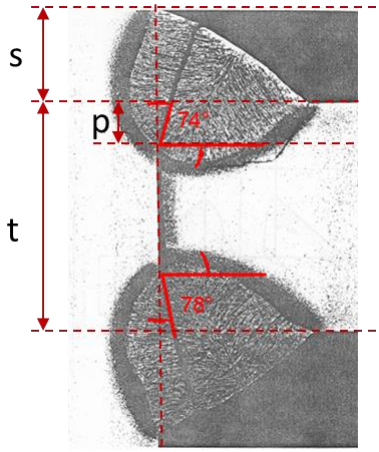

Figure 2.15: A typical weld root cracking through weld throat in load-carrying fillet welded cruciform specimen ($s/t \approx 0.65$ and $p/t \approx 0.2$)

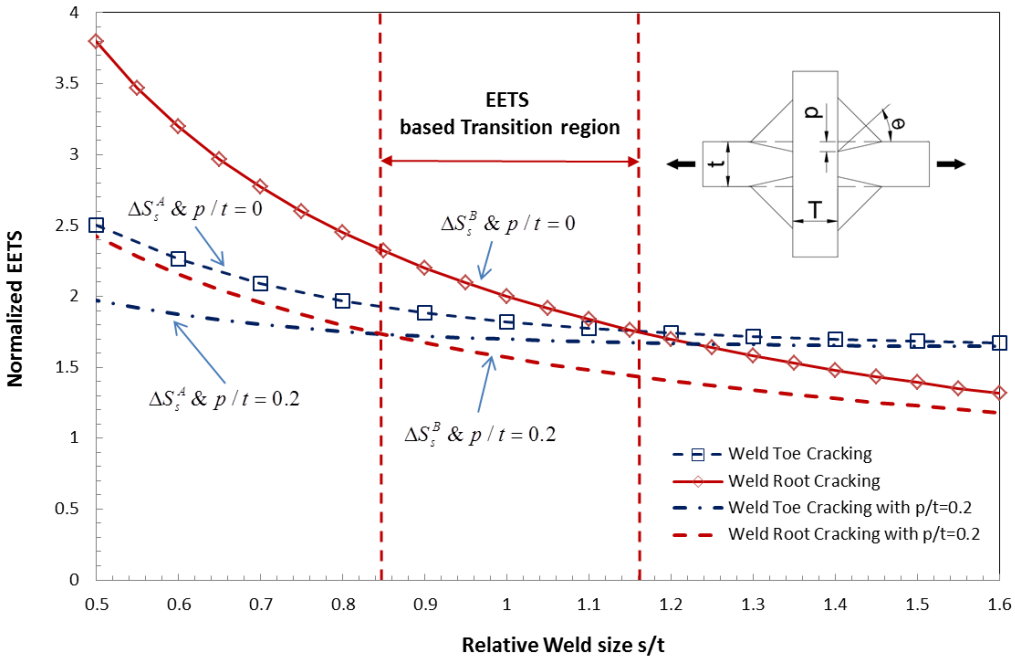

Figure 2.16: EETS based critical weld size determination

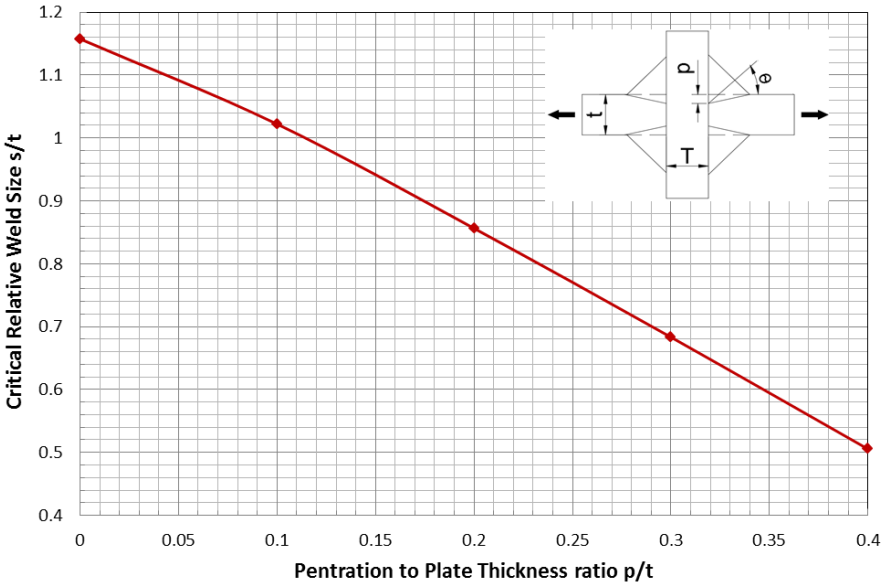

Figure 2.17: EETS based critical weld size θ_c versus relative weld penetration (p/t)

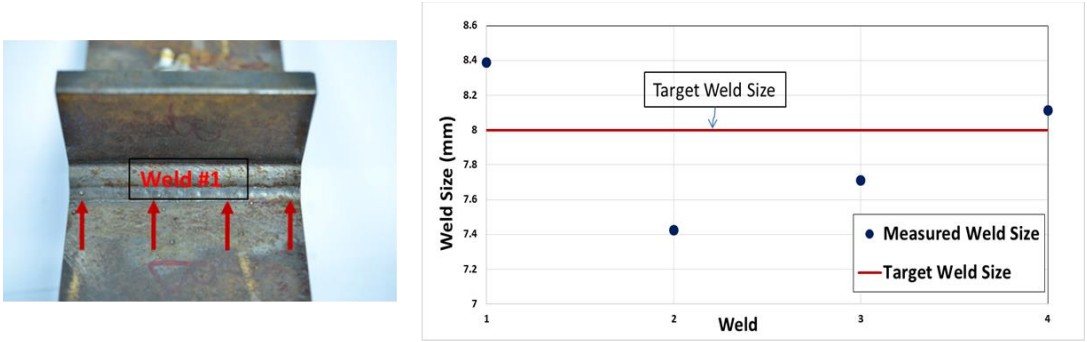

Figure 2.18: Illustration of fillet weld size measurement procedure: (a) Measurement positions along each weld; (b) Comparison of measured weld size with target weld size (8*mm*) on a specimen (four welds in each specimen)

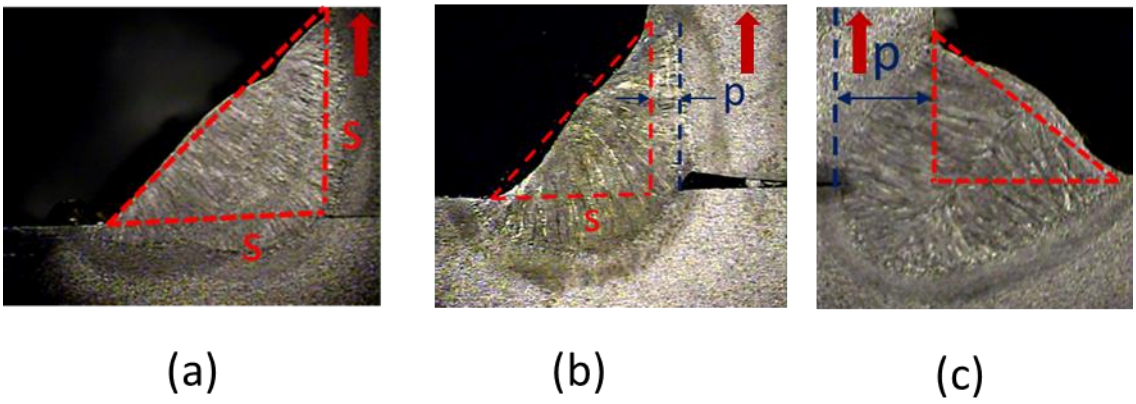

Figure 2.19: Typical weld macros: (a-c) Representative fillet weld cross-sections indicating a varying degree of penetration (*p*)

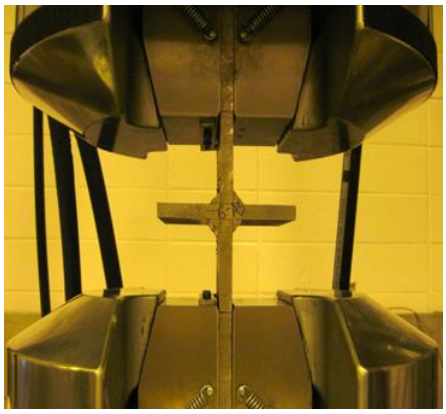

Figure 2.20: Fatigue test machine with a specimen mounted prior to testing

Figure 2.21: Representative failure modes observed from fatigue testing: (a) weld toe cracking (Mode A); (b) weld root cracking (Mode B)

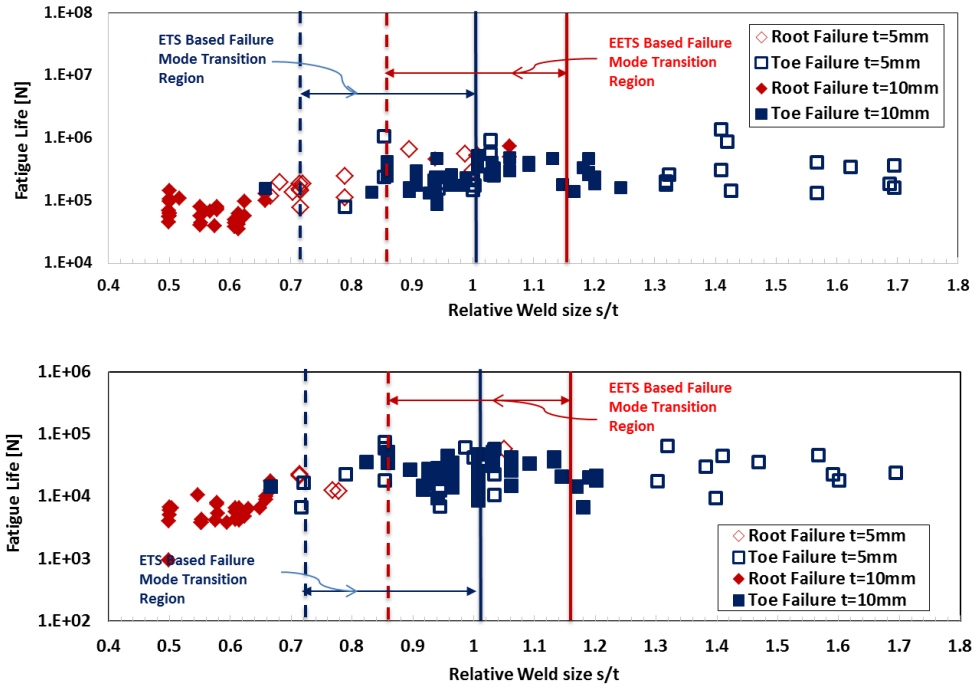

Figure 2.22: Experimental data versus relative Actual weld size: (a) fatigue data tested under ±15Ksi; (b) fatigue data tested under ±30Ksi;

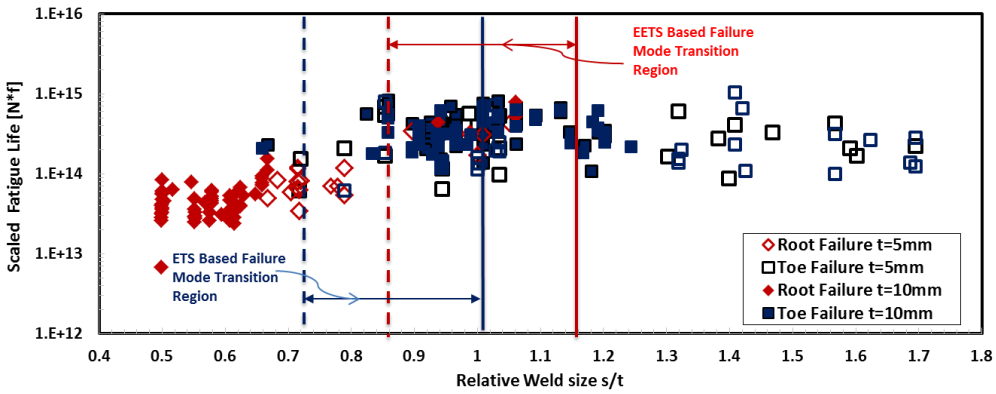

Figure 2.23: Scaled fatigue lives by Eq. (2.22) versus relative weld size

Acknowledgment

The authors acknowledge the support of this work through a grant from the National Research Foundation of Korea (NRF) Gant funded by the Korea government (MEST) through GCRC-SOP at University of Michigan under Project 2-1: Reliability and Strength Assessment of Core Parts and Material System.

References

[1] Maddox, Stephen John. Fatigue strength of welded structures. Woodhead publishing, 1991.
[2] Maddox, Stephen J. "Status review on fatigue performance of fillet welds." Journal of Offshore Mechanics and Arctic Engineering 130.3 (2008): 031006.
[3] Gurney, Timothy Russell. Fatigue of welded structures. CUP Archive, 1979.
[4] Noblett, J. E., and R. M. Andrews. "A stress intensity factor solution for root defects in fillet and partial penetration welds." Fatigue: Core Research from TWI (2000): 120.
[5] Kainuma, Shigenobu, and Takeshi Mori. "A fatigue strength evaluation method for load-carrying fillet welded cruciform joints." International journal of fatigue 28.8 (2006): 864-872.
[6] Kainuma, Shigenobu, and Takeshi Mori. "A study on fatigue crack initiation point of load-carrying fillet welded cruciform joints." International Journal of Fatigue 30.9 (2008): 1669-1677.
[7] Balasubramanian, V., and B. Guha. "Establishing criteria for root and toe cracking of load carrying cruciform joints of pressure vessel grade steel." Engineering Failure Analysis 11.6 (2004): 967-974.
[8] Hong, Jeong K. "Evaluation of weld root failure using battelle structural stress method." Journal of Offshore Mechanics and Arctic Engineering 135.2 (2013): 021404.
[9] Hobbacher, Adolf, ed. Fatigue design of welded joints and components: Recommendations of IIW Joint Working Group XIII-XV. Woodhead Publishing, 1996.
[10] Hobbacher, A. "IIW Recommendations for fatigue design of welded joints and components, Doc. IIW-1823." WRC Bulletin 520.
[11] BS7608, British Standard. "Code of practice for fatigue design and assessment of steel structures." British Standards Institution (1993).
[12] Fricke, Wolfgang. "Recommended hot-spot analysis procedure for structural details of ships and FPSOs based on round-robin FE analyses." International Journal of Offshore and Polar Engineering 12.01 (2002).
[13] Design of steel structures—Part 1-1. ENV 1993-1-1. Eurocode 3, European Committee for Standardization, Brussels, 1992.
[14] Dong, P., and J. K. Hong. "Analysis of hot spot stress and alternative structural

stress methods." ASME 2003 22nd International Conference on Offshore Mechanics and Arctic Engineering. American Society of Mechanical Engineers, 2003.
[15] Dong, P. "A structural stress definition and numerical implementation for fatigue analysis of welded joints." International Journal of Fatigue 23.10 (2001): 865-876.
[16] Nie, Chunge, and Pingsha Dong. "A traction stress based shear strength definition for fillet welds." The Journal of Strain Analysis for Engineering Design 47.8 (2012): 562-575.
[17] Huang, T. D., et al. "Reduction of Overwelding and Distortion for Naval Surface Combatants, Part 1: Optimized Weld Sizing for Lightweight Ship Structures." Journal of Ship Production and Design 30.4 (2014): 184-193.
[18] Dong, P., et al. "A Math-Based Design-for-Produceability Evaluation of Titanium Applications in Ship Hull Structures." Transactions-Society of Naval Architecture and Marine Engineers (SNAME). 2013. 299-305.
[19] Veritas, Det Norske. "Fatigue design of offshore steel structures." No. DNV-RP-C203 (2005)..
[20] Lahti, Kari E., Hannu Hänninen, and Erkki Niemi. "Nominal stress range fatigue of stainless steel fillet welds—the effect of weld size." Journal of Constructional Steel Research 54.1 (2000): 161-172.
[21] Lotsberg, Inge. "Fatigue design of welded pipe penetrations in plated structures." Marine structures 17.1 (2004): 29-51.
[22] Petinov, S. V., W. S. Kim, and Y. M. Paik. "Assessment of fatigue strength of weld root in ship structure: an approximate procedure." Ships and Offshore Structures 1.1 (2006): 55-60.
[23] Dong, P., et al. "The Master SN Curve Method an Implementation for Fatigue Evaluation of Welded Components in the ASME B&PV Code, Section VIII, Division 2 and API 579-1/ASME FFS-1." Welding Research Council Bulletin 523 (2010).
[24] Dong, P. "A robust structural stress method for fatigue analysis of offshore/marine structures." Journal of offshore mechanics and Arctic engineering 127.1 (2005): 68-74.
[25] Dong, Pingsha, Jeong K. Hong, and Ab Ílio MP De Jesus. "Analysis of recent fatigue data using the structural stress procedure in ASME Div 2 rewrite." Journal of Pressure Vessel Technology 129.3 (2007): 355-362.
[26] Dong, P., and J. K. Hong. "The master SN curve approach to fatigue evaluation of offshore and marine structures." ASME 2004 23rd International Conference on Offshore Mechanics and Arctic Engineering. American Society of Mechanical Engineers, 2004.
[27] Lu, Hanqing, Pingsha Dong, and Srimanth Boppudi. "Strength analysis of fillet welds under longitudinal and transverse shear conditions." Marine Structures 43 (2015): 87-106.
[28] ASME Boiler and Pressure Vessel Code, Section VIII, Division 2, 2007.
[29] API 579 RP-1/ASME FFS-1, Fitness-For-Service, 2007
[30] Dong, P., and J. Hong. "A robust structural stress parameter for evaluation of multiaxial fatigue of weldments." Fatigue and Fracture Mechanics: 35th Volume. ASTM International, 2007.
[31] Wei, Zhigang, and Pingsha Dong. "A generalized cycle counting criterion for arbitrary multi-axial fatigue loading conditions." The Journal of Strain Analysis for

Engineering Design (2014): 0309324713515465.
[32] Knight, J. W. Some basic fatigue data for various types of fillet welded joints in structural steel. Welding Institute, 1976.
[33] AWS B4.0: 2007. Standard methods for mechanical testing of welds.
[34] Fricke, Wolfgang. "IIW guideline for the assessment of weld root fatigue." Welding in the World 57.6 (2013): 753-791.
[35] Turlier, Didier, Patrice Klein, and Florent Bérard. "FEA shell element model for enhanced structural stress analysis of seam welds." Welding in the World 58.4 (2014): 511-528.

Chapter 3
An Analytical SCF Solution Method for Joint Misalignments and Application in Fatigue Test Data Interpretation

Abstract

In this study, we first present a general analytical method for calculating stress concentration factors in a cruciform connection containing either axial or angular misalignment between two intercostal members based on a potential energy formulation. As such, various end restraint conditions of interest in practice can be considered with ease. Such a solution method provides stress concentration factors at intersection location not only with respect to intercostal members, but also with respect to continuous members. A comprehensive set of SCF solutions, confirmed by finite element solutions, are then presented in tabular forms which can be used as supplements to the existing SCF solutions such as those given in BS 7910 and DNV-RP-C203 for performing fatigue and fracture assessment of welded connections. Some of the existing solutions are shown to be valid only under a narrower set of conditions than documented and some seem to be in significant error. As a further demonstration of the validity of the analytical approach presented in this paper, the same analytical formulation is applied for examining interaction effects between misalignments and fatigue testing conditions, resulting in significantly improved correlation of fatigue test data obtained as a part of this study.

Keywords: Load-carrying cruciform joint; axial misalignment; angular misalignment; fatigue testing; master S-N curve; stress concentration

3.1 Introduction

Load-carrying fillet-welded connections are commonly used in welded structures and prone to misalignments either due to poor fit-up conditions prior to or welding induced distortions during welding assembly [1]. Two types of misalignments (i.e., axial misalignment and angular misalignment, as illustrated in Figure 3.1, respectively) must be controlled to within an acceptable tolerance during manufacturing and structural assembly in order to avoid any significant impact on joint fatigue performance. For ship structures, the acceptable limits may be defined as one half of plate thickness of the discontinuous member (or intercostal member) for axial misalignments and one half of plate thickness at an intercostal plate position based on stiffener spacing, as recently discussed by Huang et al. [2]. Figure 3.1shows two representative fatigue test specimens among those investigated in this study: one exhibits dominantly axial misalignment (see Figure 3.1a) and the other angular misalignment (see Figure 3.1b). These misalignments were considered acceptable under typical shipyard environment, for which fatigue test results have been presented in [3] and analyzed using a new traction stress method [3].

There have been numerous analytical and experimental studies in the literature on effects of manufacturing-caused misalignments on fatigue performance of welded joints, such as on load-carrying cruciform joints [4-6] and butt-seam welded joints [7]. It has been shown that fatigue of welded connections can be significantly impacted by joint misalignments which introduce secondary bending at the presence of axial tension on loaded intercostal members both in laboratory testing and in service conditions. In what follows, we briefly highlight some of prior research efforts that are relevant to this study and discuss areas that require an improved analytical treatment of joint misalignments in terms of reliable stress concentration factor solutions under more general boundary

conditions than being considered in the literature.

To quantitatively estimate the stress concentration factors (SCF) resulted from both axial and angular misalignments in load-carrying cruciform joints, Berge and Myhye [4] proposed two expressions that were derived from simple beam theory under statically determinate conditions. They recognized that any presence of redundant supports, i.e., additional displacement-based boundary conditions, could complicate the solution process for analytically calculating misalignment-induced bending stresses. Therefore, they chose finite element method. Upon some detailed finite element investigations under various boundary constraints, a scaling parameter was introduced into their SCF expressions, which was determined based on finite element (beam) analysis results by assuming all members being identical in lengths and thicknesses in a cruciform joint. Wylde and Maddox [7] applied these SCF expressions (corresponding to free end conditions on the continuous member) developed by Berge and Myhye [4] in analyzing a set of fatigue test data from butt welded joints and demonstrated a good correlation among specimens with a varying degree of axial misalignments.

Subsequently, Andrews [5] performed an experimental investigation into axial misalignment effects on fatigue strength of load-carrying cruciform joints. These specimens were manufactured with pre-designed axial misalignments and tested under grip conditions that incorporated a spacer with its thickness being the same as actual axial misalignment amount to prevent any pre-stressing or deformation during specimen mounting prior to fatigue testing. Under cyclic tension loading conditions, Andrew [5] reported that an axial misalignment of 50% base plate thickness caused an average 65% fatigue strength reduction (weld toe cracking failure mode) at 10^5 cycles, comparing with

that for nominally aligned specimens. A further increase in axial misalignment to an amount of 100% of base plate thickness, the fatigue strength at 10^5 cycles was reduced to about 35%. Andrew [5] noted that the SCF expression given by Berge and Myhye [4] overestimated the stresses by about 20% comparing to strain gauge measurements for misalignment *e/t=1*. The reasons for these discrepancies remain elusive.

Recognizing some of the detrimental effects of joint misalignments on fatigue performance, major fitness-for-service (FFS) assessment procedures such as BS 7910 [8] and fatigue evaluation procedure such as BS 7608 [9] and DNV-RP-C203 [10] all provide SCF expressions for treating both axial and angular misalignments. However, there exist a number of issues in some of the existing SCF expressions given in these procedures [8-10]:

(a) Lack of generality: For instance, BS 7910 [8] adopted the SCF equations developed by Berge and Myhye [4] discussed above, which contain a scaling parameter determined from finite element results under a set of specific boundary conditions. These boundary conditions may not be consistent with a given application of concern. As a case in point, Berge and Myhye [4] assumed a cruciform joint configuration in which all member thicknesses and lengths were assumed being the same. Obviously, if the intercostal members have different thicknesses, which often occur in practice [2], the scaling parameters developed by Berge and Myhye [4] may no longer be applicable

(b) Insufficient documentation of assumptions used: For instance, DNV-RP-C203 [10] provides only one SCF expression for treating axial misalignment in cruciform joint configuration with pinned conditions at all four ends without

providing a clear any reference stress definition. This can cause confusions in practice, resulting in erroneous SCF calculations when considering joint misalignment effects.

(c) No consideration of SCF at weld toe on continuous members: To our best knowledge, all previous investigations [e.g., 4-6] and the existing SCF expressions provided in codes and standards [8-10] have not addressed stress concentration on continuous members. Both axial and angular misalignments can cause secondary bending stress concentration at weld toe on continuous member subjected various end conditions in an actual structure. In structural life evaluation, such stress concentration effects on fatigue must be taken into account in order to ensure the fitness of a structure of concern for intended service.

In this study, we first present an analytical SCF calculation method for treating misalignments in a general cruciform connection with its ends being subjected to maximum possible boundary constraints by means of a potential energy formulation. Such a solution method allows a direct calculation of SCFs at joint location with respect to both intercostal and continuous members. Note that for the latter, there are no solutions available in the literature to our best knowledge. Finite element analysis is then performed to confirm the validity of the assumptions and formulation method used in the proposed approach. Solutions for special cases considered in some widely used Codes and Standards such as BS 7910 [8] and DNV-RP-C203 [10] can be obtained simply by selectively removing relevant boundary constraints in the general formulation. As a result, some of the solutions given in these Codes and Standards are shown to be

valid only under some specific conditions and some seem to be in significant error for intended applications, in addition to shedding lights on how others can be correctly used. Finally, the same analytical method is also extended for capturing stress concentration effects on fatigue test data as a result of interactions between misalignments and specimen grip conditions involved in fatigue testing. As a result, the validity of the analytical method is further proven by its effectiveness in interpreting a large amount of fatigue test data on load-carrying cruciform joints containing various amount of axial and angular misalignments.

3.2 Analytical Model for Misalignment Effects

3.2.1 Formulation and Solution

Consider a cruciform connection with all its ends being fully restrained except the translational degree of freedom at the right end of the intercostal member, as illustrated in Figure 3.2a. In a statically equivalent sense, all redundant boundary conditions can be replaced by reaction forces and moments, leading to a statically determinate structure (see Figure 3.2b). As a result, a total of eight reaction forces and moments can be identified as V_I , M_I , P_{III} , V_{III} , M_{III} , P_{IV} , V_{IV} , M_{IV} .

Consider statically equilibrium conditions with respect to each of the four members (labeled as $\boxed{1}$ through $\boxed{4}$ in Figure 3.2a) of the cruciform connection, the moments and forces acting on each member section can be expressed as follows:

$$M_1 = V_I x + M_I \qquad 0 \le x \le L_1 \tag{3.1}$$

$$M_2 = \begin{pmatrix} M_I + V_I x + (-P_{III} - P_{IV})(x - L_1) \\ -P_I e - M_{III} + M_{IV} + V_{III} L_3 - V_{IV} L_4 \end{pmatrix} \qquad L_1 \le x \le L_1 + L_2 \tag{3.2}$$

$$M_3 = V_{III} y - M_{III} \qquad 0 \le y \le L_3 \tag{3.3}$$

$$M_4 = -V_{IV} z + M_{IV} \qquad 0 \le z \le L_4 \tag{3.4}$$

$$P_1 = P_I \qquad 0 \le x \le L_1 \tag{3.5}$$

$$P_2 = P_I - V_{III} - V_{IV} \qquad L_1 \le x \le L_1 + L_2 \tag{3.6}$$

$$P_3 = P_{III} \qquad 0 \le y \le L_3 \tag{3.7}$$

$$P_4 = P_{IV} \qquad 0 \le z \le L_4 \tag{3.8}$$

as a function of local coordinate along each member as indicated in Figure 3.2b. Then strain energy due to bending and axial force actions as well as total energy of the system can be expressed as,

$$U_{bending} = \int_0^{L_1} \frac{M_1^{\,2}}{2 \cdot E \cdot \mathrm{I}_1} \mathrm{d}x + \int_{L_1}^{L_1+L_2} \frac{M_2^{\,2}}{2 \cdot E \cdot \mathrm{I}_2} \mathrm{d}x + \int_0^{L_3} \frac{M_3^{\,2}}{2 \cdot E \cdot \mathrm{I}_3} \mathrm{d}y + \int_0^{L_4} \frac{M_4^{\,2}}{2 \cdot E \cdot \mathrm{I}_4} \mathrm{d}z \tag{3.9}$$

$$U_{tensile} = \int_0^{L_1} \frac{P_1^2}{2 \cdot \mathrm{E} \cdot A_1} \mathrm{d}x + \int_{L_1}^{L_1+L_2} \frac{P_2^{\,2}}{2 \cdot \mathrm{E} \cdot A_2} \mathrm{d}x + \int_0^{L_3} \frac{P_3^{\,2}}{2 \cdot \mathrm{E} \cdot A_3} \mathrm{d}y + \int_0^{L_4} \frac{P_4^{\,2}}{2 \cdot \mathrm{E} \cdot A_4} \mathrm{d}z \tag{3.10}$$

$$U = U_{tensile} + U_{bending} \tag{3.11}$$

respectively. In the above equations, E is Young's modulus, I and A represent moment of inertia and cross section area of each member. Applying Castiliano's second theorem, one obtains the relations between reaction forces and displacements through:

$$\left[\frac{\partial U}{\partial M_I} \quad \frac{\partial U}{\partial V_I} \quad \frac{\partial U}{\partial M_{III}} \quad \frac{\partial U}{\partial V_{III}} \quad \frac{\partial U}{\partial M_{IV}} \quad \frac{\partial U}{\partial V_{IV}} \quad \frac{\partial U}{\partial P_{III}} \quad \frac{\partial U}{\partial P_{IV}} \right]^T = \underline{0} \tag{3.12}$$

The eight unknown reaction forces and moments (given in Figure 3.2) can be obtained by solving the simultaneous equations (Eq. (3.12)). Then, the bending moment acting on each member section can be analytically expressed according to Eqs. (3.1) through (3.4) with the critical locations defined at $x = L_1$, $y = L_3$ and $z = L_4$ in Eqs. (3.1) through (3.4), respectively. It should be pointed out that the present derivation also provides bending

stress solutions for the continuous members at the junction, i.e., at $y = L_3$, $z = L_4$.

By ignoring higher order terms, normalized bending stresses at the four critical locations with respect to reference stress $\sigma_{p1} = p_I / A_1$ can be expressed in two parts with respect to ith $(i = 1,2,3,4)$ member

$$\left(\frac{\sigma_b}{\sigma_{p1}}\right)_i^{(e)} = \left(\frac{6L_1L_2L_3L_4t_1t_i}{\left(L_1L_2L_3t_4^{\,3} + L_1L_2L_4t_3^{\,3} + L_1L_3L_4t_2^{\,3} + L_2L_3L_4t_1^{\,3}\right)L_i}\right)e \qquad (3.13)$$

$i = 1, 2, 3, 4$

which is directly resulted from the presence of axial misalignment *e*, and structural interaction among members:

$$\left(\frac{\sigma_b}{\sigma_{p1}}\right)_i^{(s)} = \frac{3L_1L_2^{\,2}\left(L_3^{\,2}t_4^{\,3} - L_4^{\,2}t_3^{\,3}\right)t_1t_i}{L_3L_4t_2\left(L_1L_2L_3t_4^{\,3} + L_1L_2L_4t_3^{\,3} + L_1L_3L_4t_2^{\,3} + L_2L_3L_4t_1^{\,3}\right)L_i} \qquad (3.14)$$

$i = 1..2$

$$\left(\frac{\sigma_b}{\sigma_{p1}}\right)_i^{(s)} = (-1)^{i+1}\frac{3L_2\left(\begin{array}{l}\dfrac{L_1L_2t_3^{\,3}L_3t_4^{\,3}}{t_i^{\,3}} + \dfrac{L_1L_2L_4t_3^{\,3}t_4^{\,3}}{t_i^{\,3}} + \\ \dfrac{L_3^{\,2}t_2^{\,3}L_1L_4^{\,2}}{L_i^{\,2}} + \dfrac{L_3^{\,2}L_2t_1^{\,3}L_4^{\,2}}{L_i^{\,2}}\end{array}\right)t_i^{\,2}}{L_3L_4t_2\left(\begin{array}{l}L_1L_2L_3t_4^{\,3} + L_1L_2L_4t_3^{\,3} + \\ L_1L_3L_4t_2^{\,3} + L_2L_3L_4t_1^{\,3}\end{array}\right)} \qquad (3.15)$$

$i = 3..4$

which is related to structural interactions among the members in cruciform connections. In Eqs. (3.14) and (3.15), t_i and L_i stand for thickness and length of ith member. The total stress concentrations at the junction with respect to ith member can be expressed as:

$$\left(\frac{\sigma_b}{\sigma_{p1}}\right)_i = \left(\frac{\sigma_b}{\sigma_{p1}}\right)_i^{(e)} + \left(\frac{\sigma_b}{\sigma_{p1}}\right)_i^{(s)} \qquad (3.16)$$

Note that the contributions from interactions of structural members as given in Eqs. (3.14)

and (3.15) become negligible if all length dimensions of members are far greater than their thicknesses.

With the above developments, solutions to various axial misalignment cases that are of interest in practice can be developed simply by selectively removing boundary restraints and setting related reaction forces and moments to zero in Eqs. (3.9) and (3.10). These solutions are summarized in Table 3A- 1in Appendix 3-A. As an example, the SCF solution for Case No. 5 in Table 3A- 1can be obtained by simply setting $P_{III} = P_{IV} = 0$ in Eq. (3.10)(see also Figure 3.2b).

A general cruciform connection with angular misalignment conditions subjected to a set of general boundary conditions (shown in Figure 3.3) can be treated in the same manner. The only difference here is that angular misalignment α contributes to both the bending moment of 1st member section (Eq.(3.1)) in the form of $p_I \alpha x$ and moment of 2nd member section (Eq. (3.2)) in the form of $p_I \alpha L_1$ instead of $p_I e$. Then, the final solutions can be derived as follows, by following the same procedure described above:

$$\left(\frac{\sigma_b}{\sigma_{p1}}\right)_i^{(\alpha)} = \left(\frac{3L_3 L_4 t_i t_1 \left(\begin{array}{l} \dfrac{L_1 L_3 L_4 t_1^{\,3} t_2^{\,3}}{t_i^{\,3}} + \dfrac{L_2^{\,2} L_1^{\,2} L_3 t_4^{\,3}}{L_i^{\,2}} + \\ \dfrac{L_2^{\,2} L_1^{\,2} L_4 t_3^{\,3}}{L_i^{\,2}} + \dfrac{L_2 L_3 L_4 t_1^{\,3} t_2^{\,3}}{t_i^{\,3}} \end{array} \right)}{L_1 L_2 \left(L_3 t_4 + L_4 t_3\right) \left(\begin{array}{l} L_1 L_2 L_3 t_4^{\,3} + L_1 L_2 L_4 t_3^{\,3} + \\ L_1 L_3 L_4 t_2^{\,3} + L_2 L_3 L_4 t_1^{\,3} \end{array} \right)} \right) \alpha \qquad (3.17)$$

$i = 1, 2$

$$\left(\frac{\sigma_b}{\sigma_{p1}}\right)_{\mathrm{i}}^{(\alpha)} = \left(\frac{3L_3^{\,2}L_4^{\,2}t_i\left(L_1^{\,2}t_2^{\,3} - L_2^{\,2}t_1^{\,3}\right)t_1}{L_1L_2\left(L_3t_4 + L_4t_3\right)\begin{pmatrix} L_1L_2L_3t_4^{\,3} + L_1L_2L_4t_3^{\,3} + \\ L_1L_3L_4t_2^{\,3} + L_2L_3L_4t_1^{\,3} \end{pmatrix}L_i} \right)\alpha \qquad (3.18)$$

$i = 3, 4$

where, i, t_i, and L_i follow the same definition as for the solutions corresponding to the axial misalignment case, as shown in Figure 3.3.

The SCFs resulted from structural interactions are the same as Eqs. (3.14)-(3.15) since the structure in Figure 3.3 remains the same as that in Figure 3.2 when axial and angular misalignments are not considered. The total stress concentration can be evaluated by using Eq. (3.16) replacing $\left(\frac{\sigma_b}{\sigma_{p1}}\right)_i^{(e)}$ with $\left(\frac{\sigma_b}{\sigma_{p1}}\right)_i^{(\alpha)}$. Again, by releasing selected boundary restraints, a set of SCF solutions for some practical cases can be generated and are given in Table 3A- 2 in Appendix 3-A**.**

3.2.2 Comparison with FE Solutions

To ensure that the assumptions and analytical formulations used in the previous section are valid, finite element beam models shown in Figure 3.4 (one for axial misalignment condition, see Figure 3.4a, and the other for angular misalignment, see Figure 3.4b) are considered here, representing a rather general cruciform configuration in terms of member thicknesses (t_1 through t_4) and lengths (L_1 through L_4) with the same boundary conditions as shown in Figure 3.2a and Figure 3.3a. Note that the finite element solution for each case shown in Figure 3.4 yields the total stresses represented by Eq. (3.16) for both cases. Both finite element and analytical results for the axial alignment case shown in Figure 3.4 are compared in Figure 3.5a, along with existing

solutions given in BS 7910 [8] and DNV-RP-C203 [10], in terms of normalized SCFs by FEA results. It can be seen that the analytical results according to Eqs. (3.13) through (3.16) show a very good agreement with finite element results at all critical locations. However, BS 7910 under-estimates SCF value about 50% at the intersection position on 1st member, while over-estimating by about 125% at the intersection position on 2nd member. DNV-RP-C203 [10] gives a reasonable SCF estimation for 1st member, while noticeably under-estimating SCF for 2nd member on which further detailed discussions will be given in a later section. It should be pointed out here that stress concentrations at the interaction positions on continuous members (3rd and 4th) are significant for the cases investigated here, which are not addressed by BS 7910 [8] and DNV-RP-C203 [10]. For the case with angular misalignment depicted in Figure 3.4b, analytical results according to Eqs. (3.17)-(3.18) and Eq. (3.16) also show a good agreement with FEA results at the interaction positions on all four structural members, as shown in Figure 3.5b. BS 7910 [10] gives a reasonable SCF estimation at the intersection position on the 1st member, but a significant over-estimation on the 2nd member, at about 250% (see Figure 3.5b). It should be noted that DNV-RP-C203 [10] does not provide any SCF solutions for cruciform connections with angular misalignment.

3.3 Interactions with Fatigue Testing Conditions

It should be noted that the SCF solutions discussed in Sec. 3.2 are strictly valid for misalignments that are already presented in as-assembled structures in which a reference load is applied on one of the members such as 1st member in Figure 3.2 and Figure 3.3. In fatigue testing, a specimen with pre-existing misalignments must be mounted to a fatigue testing machine, typically through a hydraulic grip system (see

Figure 3.6) that are aligned with machine loading axis. The application of such a grip mechanism can cause pre-deformation (see Figure 3.6b) on a specimen containing an axial misalignment (*e*), which result in additional secondary stress concentration due to the presence of a deflection curve marked as *d(X)* in Figure 3.6b during cyclic loading during fatigue testing. Obviously, such a nonlinear geometry effect can be mitigated by adding a shim of thickness *e*, which can be difficult to accomplish in practice since *e* can vary from specimen to specimen, particularly when dealing with angular misalignment.

3.3.1 Axial Misalignment and Gripping

Consider a cruciform specimen containing an axial misalignment of *e* as shown in Figure 3.6a. In mounting the specimen to fatigue test grips can be modeled by considering one end of the specimen being fixed while both a transverse force and moment are applied on the other such that both ends of the specimen are aligned with the load application line, as shown in Figure 3.6b. With this deformed configuration (Figure 3.6b), the analytical method discussed in Sec. 3.2 can then be applied for computing stress concentration factor due to axial fatigue loading *P*. A two-step analytical solution process is described below.

3.3.1.1 Gripping-Induced Deformation

The analysis procedure is identical to those discussed in Sec. 3.2, except that this is a displacement-controlled process for which a dummy force *F* at a distance of *X* is introduced for computing gripping-induced deflection, as shown in Figure 3.6a. Then, moments on each beam section can be written as:

$$M_1 = -\mathrm{M} - \mathrm{V}\cdot x \qquad 0 \le x \le X \tag{3.19}$$

$$M_2 = -\mathrm{M} - \mathrm{V}\cdot \mathrm{x} + \mathrm{F}\cdot(\mathrm{x} - X) \qquad X \le x \le L \tag{3.20}$$

Then, the corresponding strain energy can be expressed as:

$$U_{bending} = \int_0^X \frac{M_1^{\,2}}{2E\mathrm{I}}\mathrm{d}x + \int_X^L \frac{M_2^{\,2}}{2E\mathrm{I}}\mathrm{d}x \tag{3.21}$$

By applying Castigliano's second theorem and setting the end displacement corresponding to shear force V as the axial misalignment amount, e, one obtains the following two equations:

$$\frac{\partial}{\partial \mathrm{M}} U_{bending} = 0 \tag{3.22}$$

$$\frac{\partial}{\partial \mathrm{V}} U_{bending} = e \tag{3.23}$$

Both reaction shear force V and moment M can then be obtained by solving Eqs.(3.22)-(3.23) . Then, the deflection can be evaluated by differentiating Eq.(3.21) with respect to dummy force F, as:

$$d(X) = \frac{\partial}{\partial \mathrm{F}} U_{bending} \tag{3.24}$$

which results in deflection curve as a function of distance X:

$$d(X) = -\frac{e(L+2X)(L-X)^2}{L^3} \tag{3.25}$$

A finite element calculation on the same configuration as in Figure 3.6b is also performed for comparing with the analytical solution given in Eq.(3.25) . The results are shown in Figure 3.7, clearly showing a good agreement between the analytical and finite element results.

3.3.1.2 Stress Concentration Calculation

The deflection curve $d(X)$, as given in Eq. (3.25), also shown in Figure 3.7, can then be used to determine eccentricity as a function of X as a result of gripping action

(see Figure 3.6b):

$$e'(X) = e + d(X) \qquad 0 \le X \le L_1 \tag{3.26}$$

$$e'(X) = d(X) \qquad L_1 \le X \le L \tag{3.27}$$

The resulting bending moment on each of the two horizontal members in Figure 3.6b can be written as:

$$m_1 = -vX - m + p\left(\mathrm{e}+\mathrm{d}(X)\right) \quad 0 \le \mathrm{X} \le \mathrm{L}_1 \tag{3.28}$$

$$m_2 = -vX - \mathrm{m} + p\mathrm{d}(X) \qquad L_1 \le X \le L \tag{3.29}$$

By comparing Figure 3.6b with Figure 3.2b, only the reaction forces and bending moments on 1st member section present, while forces and moments on 3rd and 4th members are zero. Inserting Eqs. (3.28) and (3.29) into Eq. (3.9) and applying Castiliano's second theorem, one obtains both the reaction force v and bending moment m through Eq. (3.12). Then, Eqs. (3.28) and (3.29) can be used to describe moment distributions at any position X along the two intercostal members (i.e., 1 and 2).

Consequently, normalized bending stress σ_b by the applied stress $\sigma_p = \frac{p}{A}$ (where A is the cross section area of base plate) can be expressed as a function of intersection position, $X = L_c$, as:

$$k_e = \left(\frac{\sigma_b}{\sigma_p}\right)_e = \left(\frac{3}{5} \frac{\left(\begin{array}{l} 11L^3 - 40L^2L_1 - 12L^2L_c + 30LL_1{}^2 \\ +60LL_1L_c + 30LL_c{}^2 - 60L_1{}^2L_c - 20L_c{}^3 \end{array} \right)}{L^3} \right) \frac{e}{t} \tag{3.30}$$

In fatigue testing, the length between edges of grips (see Figure 3.6) L is typically symmetrically positioned, i.e. $L_1 = L/2$. Then, Eq. (3.30) can be further simplified as:

$$k_e = \left(\frac{\sigma_b}{\sigma_p}\right)_e = \left(\frac{3}{10}\frac{\left(-3L^3 + 6L^2L_c + 60LL_c{}^2 - 40L_c{}^3\right)}{L^3}\right)\frac{e}{t} \tag{3.31}$$

3.3.2 Angular Misalignment and Gripping

The same two-step analytical solution process can be used to treat angular misalignment as illustrated in Figure 3.8. The only difference is that gripping action forces the right end to displace by an amount of αL_1. The resulting deformation after gripping is illustrated as Figure 3.8b, which is analytically expressed as:

$$d(X) = \left(\frac{\left(LL_1 - LX + 2L_1X\right)\left(L - X\right)^2}{L^3}\right)\alpha \tag{3.32}$$

Then, the second step is the same as the procedure used for treating axial misalignment in the previous section. The resulting stress concentration factor solution at position $X = L_c$ becomes:

$$k_\alpha = \left(\frac{\sigma_b}{\sigma_p}\right)_\alpha = \left(\frac{4}{5}\frac{\left(L^4 - 9L^3L_c + 39L^2L_c{}^2 - 60L_c{}^3L + 30L_c{}^4\right)}{L^3t}\right)\alpha \tag{3.33}$$

If both axial and angular misalignments are present, the combined SCF can be calculated as below:

$$k_{e+\alpha} = k_e + k_\alpha \tag{3.34}$$

which is superposition of Eqs. (3.31) and(3.33). It should be noted that angle α in Eqs. (3.33)and (3.34) has the unit of radian. For easy visualization purpose in later sections, angular misalignment α will be presented in degree hereafter.

3.3.3 Comparison with FE Solutions

Finite element models for three misalignment conditions (see detailed dimensions given in Table 3-1) were generated using 2D plain-strain elements for cruciform

connection configuration, as illustrated in Figure 3.6a and Figure 3.8a. Note that the dimensions for these two cruciform joint geometries given in Table 3-1 are taken from actual fatigue test specimens to be discussed in the next section. Nonlinear geometry effects were considered here in order to account for pre-deformation effects introduced by the gripping actions described as Step 1 of the analytical solution process discussed in Secs. 3.3.1 and 3.3.2. Bending stresses at intersection positions are calculated using a nodal forces method (see [11-14]) for suppressing sharp notch induced stress singularity so that the stress concentration results from these finite element models are consistent with the analytical solutions presented here, for which elementary structural mechanics theory is used without considering geometric discontinuities at the cruciform intersections. All finite element based calculations were carried out using ABAQUS [15]. As shown in Figure 3.9, both the finite element and analytical solutions show an excellent agreement, proving the accuracy of the analytical solution method discussed in Secs. 3.3.1.1-3.3.1.2.

3.3.4 Analysis of Fatigue Specimens and Test Data

As an integral part of this study, a systematic fatigue testing of load-carrying fillet-welded cruciform joints was conducted after detailed misalignment measurements were performed, as illustrated in Figure 3.1. Most of these specimens, manufactured to reflect production processes in typical shipyard environment, contain a varying degree of misalignments that were deemed acceptable, as discussed by Huang et al. [2]. A question to be addressed in this section is how the misalignments measured from these specimens have contributed to the data scatter of these fatigue test results.

3.3.4.1 Misalignment SCFs in Test Specimens

The overall dimensions of fatigue test specimens are given in Figure 3.10, along with a photograph (Figure 3.10b) of a representative specimen grip-mounted in fatigue machine for illustration purposes. Both continuous and intercostal members have the same thickness (t), for which two values of t are considered in this test program, i.e., *5mm* and *10mm*, respectively. Table 3B-1 in Appendix 3-B provides a summary of all relevant details of the specimen tested, including measured misalignments (axial and angular) and fatigue test results. Note that all these specimens failed at weld toe. To relate test specimen geometry including weld toe position to dimensional parameters used in the analytical model described in the previous sections (see Figure 3.6 or Figure 3.8), Figure 3.11F provides an illustration using two actual fatigue test specimens. Note the weld toe position (corresponding weld toe failure mode observed in test data) is defined as $L_c = L/2 - t/2 - s$, where s is fillet weld leg size. The resulting analytically calculated SCFs for the two specimens are compared with finite element results in Figure 3.12, showing negligible differences, even though the finite element models considered both weld root gaps and fillet welds. By applying the analytical solutions in Secs. 3.3.1. and 3.3.2 for all fatigue test specimens, the final misalignment-caused SCF results are listed in Table 3-B1 in Appendix 3-B, along with fatigue test for completeness.

3.3.4.2 Analysis of Fatigue Test Results

Detailed fatigue test procedures and data analysis based on nominal specimen geometry (i.e., without considerations of any misalignment effects which is the focus of this study) have been given in Huang et al. [2] and Xing and Dong [3]. By introducing the master S-N curve approach, originally developed by Dong et al. [11-12] and adopted

by ASME 2007 Div 2 Code [16] and API 579 [17], the test data can be presented in the form of an equivalent traction stress range, i.e.,

$$\Delta S_s = \frac{\Delta\sigma_s}{t_e^{\frac{2-m}{2m}} I(r)^{\frac{1}{m}}} \tag{3.35}$$

versus cycle to failure (N) in Figure 3.13, along with the master S-N curve scatter band given by ASME 2007 Div 2 Code [16] in Figure 3.13. In Eq.(3.35), $\Delta\sigma_s$ represents structural stress range calculated using nodal force based procedure; $t_e = t/2$ for symmetric cruciform joints; m=3.6, and r is expressed as $r = |\Delta\sigma_b| / |\Delta\sigma_s|$, where $\Delta\sigma_b = \Delta\sigma_s - \Delta\sigma_m$ and $\Delta\sigma_m$ is the membrane part of $\Delta\sigma_s$. For the detailed derivation of Eq. (3.35) and its application in formulating the master S-N curve method, interested readers may consult a series of prior publications such as [11-14], in which WRC Bulletin No. 523 [13] provides a comprehensive documentation on the method and its detailed validations.

Without considering misalignment effects for the specimens listed in Table 3-B1, the use of Eq. (3.35) results in some unexpected plate thickness effects (see Figure 3.13a) with some of the data corresponding to *t =5mm* being failing below the master S-N curve scatter band (i.e., $Mean - 2\sigma$) given in ASME Div 2 [16]. The standard deviation for the data in Table 3-B1 is calculated as 0.27. It should be pointed out here that the ASME master S-N curve scatter band with a standard deviation of 0.24 was established based on about 1000 large scale fatigue tests including cruciform fillet welded specimens like those investigated here. By examining the measured misalignments in terms of *e/t* in Table 3-B1, it can be clearly seen that the test specimens with *5mm* base plate thickness tend to show a higher value of misalignments than those with *10mm* base plate thickness.

With the analytically calculated SCF values (designated as $k_{e+\alpha}$ in Eq. (3.34) and given in Table 3-B1in Appendix 3-B), $\Delta\sigma_s$ in Eq. (3.35)is replaced by $\Delta\sigma_s + k_{e+\alpha}\Delta\sigma_p$, the same test data now shows a significantly improved correlation with the master S-N curve scatter band (see Figure 3.13b). In addition, the standard deviation for the new test data listed in Table 3-B1is now reduced from 0.27 to 0.199, once the SCFs due to misalignments in Table 3-B1 are considered.

3.4 Discussions

In this study, a comprehensive set of analytical SCF solutions to misalignments in cruciform connections have been developed under a set of more general boundary conditions and structural element dimensions (e.g. member thickness and length) than what are available in the literature. These SCF solutions have been shown to recover specific solutions directly relevant to cases stipulated in some well-known Codes and Standards such as BS 7910:2013 [8] and additional cases that are of practical interest, but not available in the literature. These solutions based on the present study are summarized in Appendix 3-A for both axial misalignments in Table 3-A1 and angular misalignments in Table 3-A2. All these analytical solutions are further confirmed by finite element solutions as demonstrated in Figure 3A. 1 in addition to the validation cases given in Figure 3.4a-Figure 3.4b. It is important to note that one major contribution of these analytical solutions is that SCFs on continuous members are now provided for the first time, which proves to be not insignificant, as shown in Figure 3A. 1c and Figure 3A. 1d, particularly in view of the fact that continuous members are usually highly loaded members in marine structures. It should be pointed out that Cases 1-3 and Cases 7-8 are also directly applicable for determining SCFs at plate butt-seam welds situated in

between stiffeners.

3.4.1 Misalignment SCFs in BS 7910

With the above developments, we are now in a position to comment on the applicability and limitations of the SCF equations given in BS 7910:2013 [8] which provides two expressions, with

$$\frac{\sigma_b}{\sigma_p} = \frac{\kappa L_1}{L_1 + L_2}\frac{e}{t} \tag{3.36}$$

for axial misalignment *e*, and

$$\frac{\sigma_b}{\sigma_p} = \frac{\kappa\alpha L_1 L_2}{t\left(L_1 + L_2\right)} \tag{3.37}$$

for angular misalignment α. In Eqs. (3.36) and (3.37), σ_p refers to applied stress acting on member *1* (with a length of L_1) and κ is a scaling parameter given in 7910:2013 [8] for $L_1 \le L_2$, which depends on specific boundary conditions (see Table 2). It should be emphasized here that the scaling parameter κ in Eqs. (3.36) and (3.37) were taken from the finite element solutions performed by Berge and Myhye [4] on a cruciform joint with all its members having the same length and thickness.

If those κ values given in BS 7910 (see the third column of Table 3-2) are valid for the conditions described, the analytical solutions developed here should confirm as such. By setting $L_1 = L_2/2 = L_3 = L_4 = l$ and $L_1 = L_2 = L_3 = L_4 = l$ in those SCF equations in Tables A1 and A2 with boundary conditions consistent with those cases given in BS 7910 (see the last column of Table 3-2), the results are listed in Table 2 under "This study". From the comparison shown in Table 3-2, some important observations can be made as follows: Firstly, the validity of κ values as given by BS 7910 [8] is confirmed for Cases

(a) – (f) and (i) under the conditions of $L_1 = L_2$, but not of $L_1 < L_2$. For conditions corresponding to $L_1 < L_2$, κ tends to be underestimated for most of the cases by BS 7910, as shown in Table 3-2 (see the fourth column for $L_1 = L_2 / 2$). Secondly, under angular misalignment conditions, neither the κ values given in BS 7910, nor the form of Eq. (3.37) can be proven valid for Cases (g) and (h). The valid form of the SCF equation corresponding to these two cases should be:

$$\left(\frac{\sigma_b}{\sigma_p}\right)_1 = c_A\left(\frac{t}{l}\right)\alpha \tag{3.38}$$

while, Eq. (3.37) from BS 7910 can be reduced to:

$$\frac{\sigma_b}{\sigma_p} = c_B\left(\frac{l}{t}\right)\alpha \tag{3.39}$$

where, c_A and c_B are constants associated with dimensions of structural members (i.e., L_1, L_2, t). As can be seen, Eqs. (3.38) and (3.39) show completely different forms in terms of independent variables involved, resulting in completely different SCFs. This observation suggests that both κ values and equation form (see Eq. (3.37)or 39) given in BS 7910 [8] are incorrect for the specified boundary conditions. In fact, the validity of Eq. (3.37)for Cases (g) and (h) according to BS 7910 can be readily challenged by considering the following: Under fully restrained conditions such as Case (g), as more clearly shown in Figure 3.3, any rotation at the intersection due to the moment caused by the eccentricity $l\alpha$ at the loaded end is obviously restricted for most part by the continuous (vertical) members (i.e., members 3 and 4). This suggests that the moment at intersection location contributing to σ_b could not possibly be linearly proportional to l, as suggested by Eq. (3.37) or Eq. (3.39).

3.4.2 Misalignment SCFs in DNV-RP-C203

There exists only one formula in DNV-RP-C203 [10] for calculating SCF due to axial misalignment for cruciform joint with pinned restraints at all four ends (shown as Case 6 in Appendix 3-A). This formula is written as:

$$SCF = \frac{6t_i^{\,2}e}{L_i\left(\frac{t_1^{\,3}}{L_1}+\frac{t_2^{\,3}}{L_2}+\frac{t_3^{\,3}}{L_3}+\frac{t_4^{\,3}}{L_4}\right)}$$
$$t_i = thickness\ of\ \ considered\ \ plate\ (i=1,2) \qquad (3.40)$$
$$L_i = length\ of\ \ considered\ \ plate (i=1,2)$$

However, reference stress for using Eq.(3.40) is not clearly defined in DNV-RP-C203 [10] since *i* varies from 1 to 2. Based on all the information provided in DNV-RP-C203 [10] regarding Eq. (3.40), the loaded member should correspond to $i=1$, leading to the interpretation that the reference stress in Eq. (3.40) is very likely defined only with respect to the 1st member of the cruciform joint. Then, for Eq. (3.40) to be valid for $i=1,2$, the term t_i^2 on its numerator must be replaced by $t_1 t_i$, as given by our analytical solution (see Case 4 in Table 3-A1). Otherwise, Eq. (3.40) underestimates SCF at the critical location on its 2nd member by about 20%, as shown in Figure 3.5. It should also be pointed out here that our analytical solutions for Case 4 and Case 6 are identical. This means that Eq. (3.40), after the correction described above, should be also valid for cruciform connections with embedded boundary conditions at all ends, which is not stated in DNV-RP-C203 [10]. Furthermore, as shown in Table 3-A1, Eq. (3.40) after correction also becomes valid for evaluating SCFs on continuous members by stating $i=1,2,3,4$, instead of $i=1,2$.

3.5 Summary

Starting with a general formulation of stress concentration problems for treatment of misalignments in cruciform connections, a comprehensive set of analytical SCF solutions under various boundary conditions have been presented and validated by finite element solutions. These analytical SCF solutions, in addition to shedding lights on detailed applicability of some of the existing SCF equations such as those in BS 7910 and DNV-RP-C203, cover a great deal of more geometric and boundary conditions of practical interest than what have been available to date. The analytical method is also applied for treatment of stress concentration development in fatigue specimens subjected to typical test conditions. As a result, the validity of the proposed analytical method has been further confirmed in its effectiveness in interpretation of fatigue test data generated as a part of this study. Finally, with the aid of these new analytical solutions, both applicability and limitations of some of the existing SCF equations for treating joint misalignments such as those given in BS 7910 and DNV-RP-C203 are discussed.

Appendix 3-A

Table 3A- 1: Bending stresses induced by axial misalignment

Case No.	Detailed Configurations and Boundary Conditions	Bending Stress Induced by Distortion
Case 1		$\left(\frac{\sigma_b}{\sigma_{p1}}\right)_i = \left(\frac{6L_i t_1}{(L_1+L_2)t_i^2}\right)e$ $i = 1, 2$
Case 2	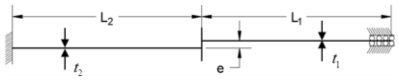	$\left(\frac{\sigma_b}{\sigma_{p1}}\right)_i = \left(\frac{6t_i L_1 L_2 t_1 \left(4\frac{L_i^3 t_1^3 t_2^3}{t_i^3} + 3\frac{L_i L_1 L_2 t_1^3 t_2^3}{t_i^3} + \frac{L_1^3 L_2^3 t_i^3}{L_i^3}\right)}{L_i\left(L_1^4 t_2^6 + 4L_1^3 L_2 t_1^3 t_2^3 + 6L_1^2 L_2^2 t_1^3 t_2^3 + 4L_1 L_2^3 t_1^3 t_2^3 + L_2^4 t_1^6\right)}\right)e$ $i = 1, 2$
Case 3	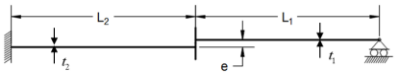	$\left(\frac{\sigma_b}{\sigma_{p1}}\right)_1 = \left(\frac{9t_1^3 L_2(2L_1+L_2)L_1}{L_1^3 t_2^4 + 3L_1^2 L_2 t_1^4 + 3L_1 L_2^2 t_1^4 + L_2^3 t_1^4}\right)e$ $\left(\frac{\sigma_b}{\sigma_{p1}}\right)_2 = \left(3\frac{t_1\left(2L_1^3 t_2^4 + 3L_1 L_2^2 t_1^4 + 2L_2^3 t_1^4\right)}{\left(L_1^3 t_2^4 + 3L_1^2 L_2 t_1^4 + 3L_1 L_2^2 t_1^4 + L_2^3 t_1^4\right)t_2^2}\right)e$
Case 4	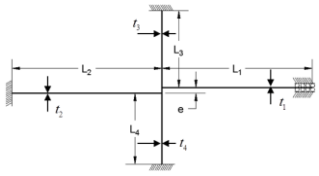	$\left(\frac{\sigma_b}{\sigma_{p1}}\right)_i = \left(\frac{6L_1 L_2 L_3 L_4 t_i t_1}{L_i\left(L_1 L_2 L_3 t_4^3 + L_1 L_2 L_4 t_3^3 + L_1 L_3 L_4 t_2^3 + L_2 L_3 L_4 t_1^3\right)}\right)e$ $i = 1, 2, 3, 4$
Case 5	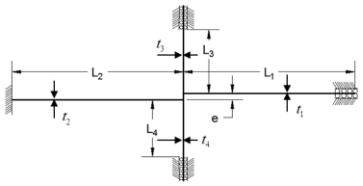	$\left(\frac{\sigma_b}{\sigma_{p1}}\right)_i = \left(\frac{6L_1 L_2 L_3 L_4 t_i t_1 \left(4\frac{L_i^3 t_2^3 t_1^3}{t_i^3} + 3\frac{L_i L_1 L_2 t_2^3 t_1^3}{t_i^3} + \frac{L_1^3 L_2^3 t_i^3}{L_i^3}\right)}{\left(\begin{array}{l} 4L_1^4 L_2 L_3 t_2^3 t_4^3 + 4L_1^4 L_2 L_4 t_2^3 t_3^3 + L_1^4 L_3 L_4 t_2^6 \\ +4L_1^3 L_2 L_3 L_4 t_1^3 t_2^3 + 6L_1^2 L_2^2 L_3 L_4 t_1^3 t_2^3 + 4L_1 L_2^4 L_3 t_1^3 t_4^3 \\ +4L_1 L_2^4 L_4 t_1^3 t_3^3 + 4L_1 L_2^3 L_3 L_4 t_1^3 t_2^3 + L_2^4 L_3 L_4 t_1^6 \end{array}\right) L_i}\right)e$ $i = 1, 2$ $\left(\frac{\sigma_b}{\sigma_{p1}}\right)_i = \left(\frac{24L_1 L_2 L_3 L_4 t_i (L_1 t_2 + L_2 t_1)\left(L_1^2 t_2^2 - L_1 L_2 t_1 t_2 + L_2^2 t_1^2\right)t_1}{\left(\begin{array}{l} 4L_1^4 L_2 L_3 t_2^3 t_4^3 + 4L_1^4 L_2 L_4 t_2^3 t_3^3 + L_1^4 L_3 L_4 t_2^6 \\ +4L_1^3 L_2 L_3 L_4 t_1^3 t_2^3 + 6L_1^2 L_2^2 L_3 L_4 t_1^3 t_2^3 + 4L_1 L_2^4 L_3 t_1^3 t_4^3 \\ +4L_1 L_2^4 L_4 t_1^3 t_3^3 + 4L_1 L_2^3 L_3 L_4 t_1^3 t_2^3 + L_2^4 L_3 L_4 t_1^6 \end{array}\right) L_i}\right)e$ $i = 3, 4$
Case 6	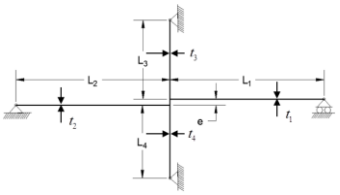	$\left(\frac{\sigma_b}{\sigma_{p1}}\right)_i = \left(\frac{6L_1 L_2 L_3 L_4 t_i t_1}{L_i\left(L_1 L_2 L_3 t_4^3 + L_1 L_2 L_4 t_3^3 + L_1 L_3 L_4 t_2^3 + L_2 L_3 L_4 t_1^3\right)}\right)e$ $i = 1, 2, 3, 4$

Note: Index i refers ith member in cruciform joint, where $i = 1, 2, 3, 4$

σ_{p1}: membrane stress of ith member section

Table 3A- 2: Bending stresses induced by angular distortion

Case No.	Detailed Configurations and Boundary Conditions	Bending Stress Induced by Distortion
Case 7		$\left(\frac{\sigma_b}{\sigma_{p1}}\right)_i = \left(\frac{6L_1L_2t_1}{(L_1+L_2)t_i^2}\right)\alpha$ $i = 1, 2$
Case 8		$\left(\frac{\sigma_b}{\sigma_{p1}}\right)_i = \left(\frac{12L_1^2t_1^4t_2^3L_2^2(L_1+L_2)}{\left(L_1^4t_2^6+4L_1^3L_2t_1^3t_2^3+6L_1^2L_2^2t_1^3t_2^3+4L_1L_2^3t_1^3t_2^3+L_2^4t_1^6\right)t_i^2}\right)\alpha$ $i = 1, 2$
Case 9	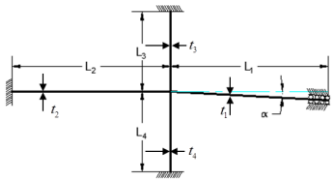	$\left(\frac{\sigma_b}{\sigma_{p1}}\right)_i = \left(\frac{3L_3L_4t_it_1\left(\frac{L_1L_3L_4t_1^3t_2^3}{t_i^3}+\frac{L_2^2L_1^2L_3t_4^3}{L_i^2}+\frac{L_2^2L_1^2L_4t_3^3}{L_i^2}+\frac{L_2L_3L_4t_1^3t_2^3}{t_i^3}\right)}{L_1L_2(L_3t_4+L_4t_3)\left(L_1L_2L_3t_4^3+L_1L_2L_4t_3^3+L_1L_3L_4t_2^3+L_2L_3L_4t_1^3\right)}\right)\alpha$ $i = 1, 2$ $\left(\frac{\sigma_b}{\sigma_{p1}}\right)_i = \left(\frac{3L_3^2L_4^2t_i(L_1^2t_2^3-L_2^2t_1^3)t_1}{L_1L_2(L_3t_4+L_4t_3)\left(L_1L_2L_3t_4^3+L_1L_2L_4t_3^3+L_1L_3L_4t_2^3+L_2L_3L_4t_1^3\right)L_i}\right)\alpha$ $i = 3, 4$
Case 10	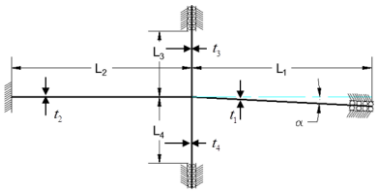	$\left(\frac{\sigma_b}{\sigma_{p1}}\right)_i = \left(\frac{12L_1^2L_2^2t_it_1\left(\frac{L_1L_3L_4t_1^3t_2^3}{t_i^3}+\frac{L_1^2L_2^2L_3t_4^3}{L_i^2}+\frac{L_1^2L_2^2L_4t_3^3}{L_i^2}+\frac{L_1L_2L_3L_4t_1^3t_2^3}{L_it_i^3}\right)}{\left(\begin{array}{l}4L_1^4L_2L_3t_4^3+4L_1^4L_2L_4t_3^3+L_1^4L_3L_4t_2^6\\+4L_1^3L_2L_3L_4t_1^3t_2^3+6L_1^2L_2^2L_3L_4t_1^3t_2^3+4L_1L_2^4L_3t_1^3t_4^3\\+4L_1L_2^4L_4t_1^3t_3^3+4L_1L_2^3L_3L_4t_1^3t_2^3+L_2^4L_3L_4t_1^6\end{array}\right)}\right)\alpha$ $i = 1, 2$ $\left(\frac{\sigma_b}{\sigma_{p1}}\right)_i = \left(\frac{12L_1^2L_2^2L_3L_4t_i(L_1^2t_2^3-L_2^2t_1^3)t_1}{L_i\left(\begin{array}{l}4L_1^4L_2L_3t_2^3t_4^3+4L_1^4L_2L_4t_2^3t_3^3+L_1^4L_3L_4t_2^6\\+4L_1^3L_2L_3L_4t_1^3t_2^3+6L_1^2L_2^2L_3L_4t_1^3t_2^3+4L_1L_2^4L_3t_1^3t_4^3\\+4L_1L_2^4L_4t_1^3t_3^3+4L_1L_2^3L_3L_4t_1^3t_2^3+L_2^4L_3L_4t_1^6\end{array}\right)}\right)\alpha$ $i = 3, 4$
Case 11	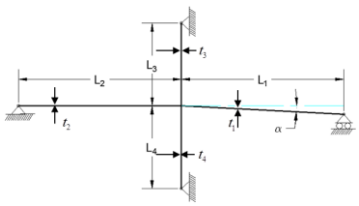	$\left(\frac{\sigma_b}{\sigma_{p1}}\right)_i = \left(\frac{\frac{3}{2}L_3L_4t_it_1(L_3t_3+L_4t_4)\left(\begin{array}{l}\frac{L_1L_3L_4t_1^3t_2^3}{t_i^3}+\frac{L_1^2L_2^2L_3t_4^3}{L_i^2}\\+\frac{L_1^2L_2^2L_4t_3^3}{L_i^2}+\frac{L_2L_3L_4t_1^3t_2^3}{t_i^3}\end{array}\right)}{L_1L_2t_3t_4(L_3+L_4)^2\left(\begin{array}{l}L_1L_2L_3t_4^3+L_1L_2L_4t_3^3\\+L_1L_3L_4t_2^3+L_2L_3L_4t_1^3\end{array}\right)}\right)\alpha$ $i = 1, 2$ $\left(\frac{\sigma_b}{\sigma_{p1}}\right)_i = \left(\frac{\frac{3}{2}L_3^2L_4^2t_i(L_1^2t_2^3-L_2^2t_1^3)(L_3t_3+L_4t_4)t_1}{t_3L_1L_2t_4(L_3+L_4)^2\left(\begin{array}{l}L_1L_2L_3t_4^3+L_1L_2L_4t_3^3\\+L_1L_3L_4t_2^3+L_2L_3L_4t_1^3\end{array}\right)L_i}\right)\alpha$ $i = 3, 4$

Note: Index i refers i[th] member in cruciform joint, where $i = 1, 2, 3, 4$

σ_{p1}: membrane stress of i[th] member section

Appendix 3-B

Table 3B- 1: Fatigue Specimen Details and Misalignment/Test Results

Specimen	t[mm]	Weld Size s[mm]	$\Delta\sigma_p$ [MPa]	Fatigue Life [N]	e/t	α [DEG]	$k_{e+\alpha}$
UM-A1	5	3	414	16600	0.20	1.41	0.82
UM-A2	5	4	414	18100	0.00	0.65	0.15
UM-A3	5	4	414	59100	0.19	0.05	0.47
UM-A4	5	4	414	22600	0.13	0.72	0.48
UM-A5	5	4	414	12700	0.29	0.78	0.87
UM-A6	5	4	414	7000	0.13	2.27	0.81
UM-A7	5	5	414	61600	0.08	0.29	0.25
UM-A8	5	5	207	177100	0.19	1.71	0.84
UM-A9	5	5	207	936200	0.20	0.21	0.52
UM-A10	5	5	414	37119	0.01	0.92	0.22
UM-A11	5	5	414	10500	0.21	0.99	0.71
UM-A12	5	5	414	22512	0.19	0.74	0.62
UM-A13	5	7	414	17600	0.12	1.72	0.64
UM-A14	5	7	414	65300	0.04	0.74	0.26
UM-A15	5	7	207	261000	0.07	1.24	0.43
UM-A16	5	7	414	29892	0.15	0.57	0.45
UM-A17	5	7	414	9500	0.28	1.13	0.86
UM-A18	5	7	207	867700	0.03	1.36	0.35
UM-A19	5	7	207	143800	0.31	1.56	1.02
UM-A20	5	7	414	35800	0.06	1.79	0.51
UM-A21	5	8	414	22500	0.31	0.69	0.81
UM-A22	5	8	414	18300	0.05	1.21	0.37
UM-A23	5	8	207	345900	0.31	0.91	0.84
UM-A24	5	9	207	183300	0.23	0.64	0.61
UM-A25	5	9	414	24000	0.02	0.19	0.08
UM-B1	10	6	414	14600	0.06	0.46	0.18
UM-B2	10	8	414	35600	0.00	0.13	0.02
UM-B3	10	8	207	134700	0.02	0.15	0.06
UM-B4	10	8	414	51600	0.04	0.12	0.08
UM-B5	10	9	207	161000	0.05	0.02	0.10
UM-B6	10	9	207	303700	0.01	0.26	0.04
UM-B7	10	9	414	14800	0.18	0.13	0.34
UM-B8	10	9	414	16300	0.06	1.74	0.29
UM-B9	10	9	414	19400	0.08	0.82	0.22
UM-B10	10	9	207	131000	0.03	1.92	0.25
UM-B11	10	9	414	24000	0.02	0.14	0.05
UM-B12	10	9	414	21000	0.04	1.78	0.26
UM-B13	10	9	207	106600	0.15	0.54	0.34
UM-B14	10	9	414	44200	0.05	0.18	0.12
UM-B15	10	9	414	26900	0.07	0.48	0.18
UM-B16	10	9	414	34400	0.02	0.50	0.09
UM-B17	10	9	414	19500	0.01	0.71	0.10
UM-B18	10	9	207	174000	0.09	0.60	0.23
UM-B19	10	9	207	233700	0.11	0.32	0.22
UM-B20	10	10	414	47800	0.04	0.26	0.11
UM-B21	10	10	414	14477	0.03	1.98	0.25
UM-B22	10	10	207	408200	0.00	0.88	0.09
UM-B23	10	10	414	34400	0.11	0.36	0.23
UM-B24	10	10	414	30200	0.08	0.18	0.16
UM-B25	10	10	207	296100	0.01	0.36	0.05
UM-B26	10	11	414	33500	0.01	0.49	0.06
UM-B27	10	12	207	467100	0.01	0.78	0.09
UM-B28	10	12	414	41900	0.07	0.82	0.19
UM-B29	10	12	414	20900	0.11	0.78	0.26
UM-B30	10	12	207	181300	0.16	0.41	0.30
UM-B31	10	12	207	335000	0.04	2.22	0.27
UM-B32	10	13	207	162800	0.05	3.26	0.39

Table 3-1: dimensions of FEA models

Dimension	Unit	Type of Misalignment		
		Axial Only	Angular Only	Combined
L	mm	127	127	127
L_c	mm	58.5	58.5	58.5
t	mm	10	10	10
e	mm	5	0	5
α	DEG	0	3	3

Table 3-2: Comparison of κ given in BS 7910 with those analytically derived from this study

Type of Misalignment	Case No.	Scaling Parameter κ			Cases in BS 7910
		BS 7910 $L_1 \le L_2$	This Study $L_1 = \frac{L_2}{2} = L_3 = L_4 = l$	This Study $L_1 = L_2 = L_3 = L_4 = l$	
Axial Misalignment	(a)	6	6	6	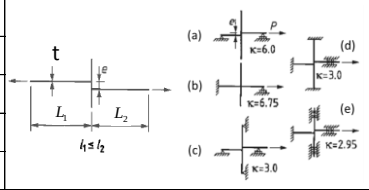
	(b)	6.75	8	6.75	
	(c)	3	5.14	3	
	(d)	3	4.50	3	
	(e)	2.95	2.88	3	
Angular Misalignment	(f)	6	6	6	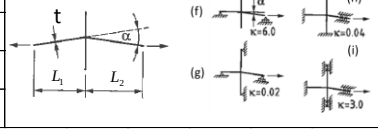
	(g)	0.02	See Eq. (38)	See Eq. (38)	
	(h)	0.04	See Eq. (38)	See Eq. (38)	
	(i)	3	3.52	3	

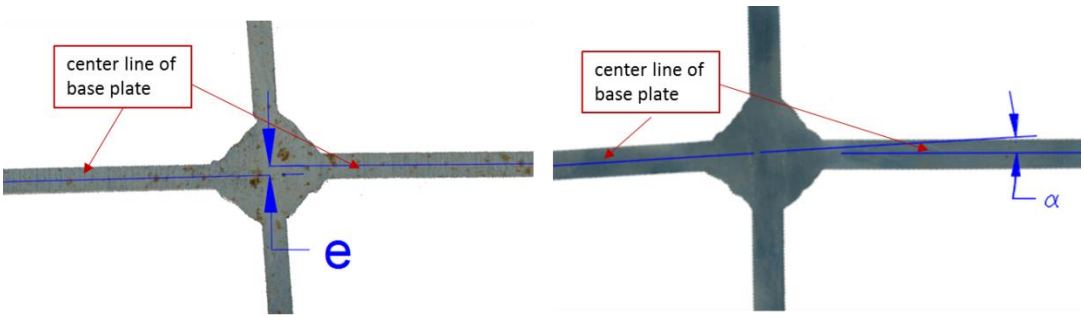

Figure 3.1: Illustration of two types of joint misalignments in fillet welded connections: (a) axial misalignment; (b) angular misalignment

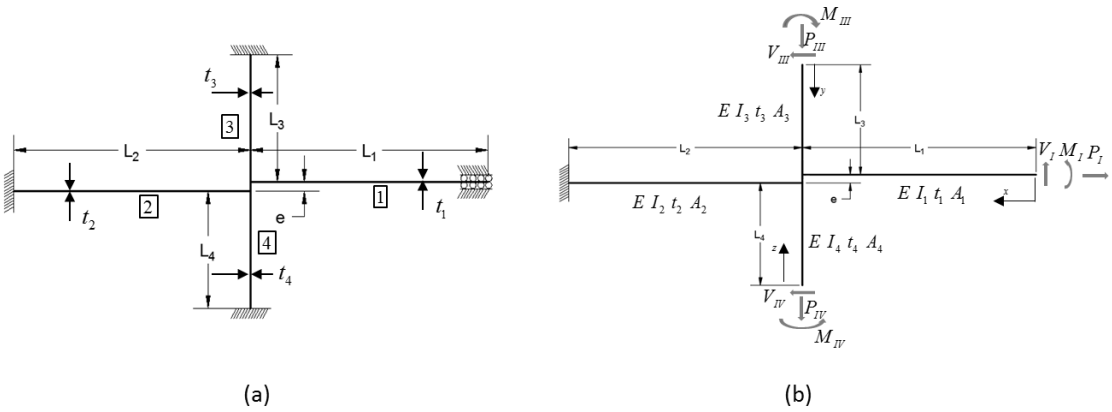

Figure 3.2: A general cruciform connection with axial misalignment and its analytical treatment: (a) end restraint conditions considered; (b) replacements of redundant boundary conditions by statically equivalent reaction forces and moments

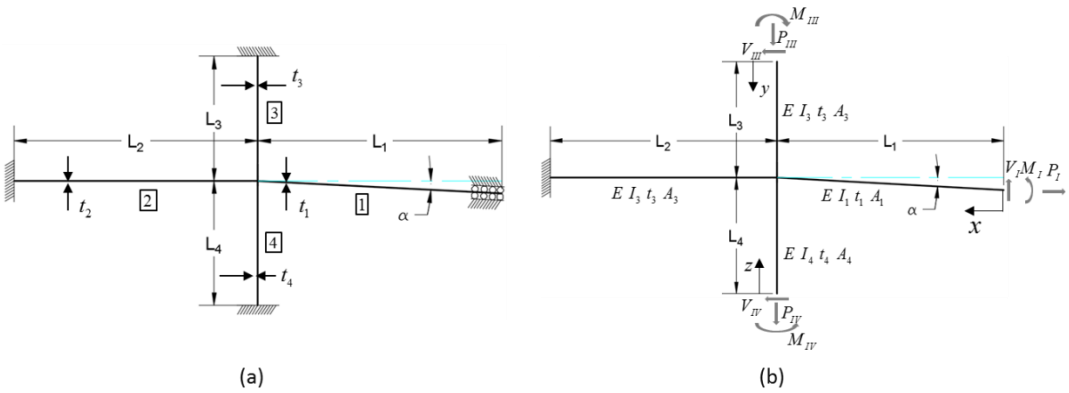

Figure 3.3: A general cruciform connection with angular misalignment and its analytical treatment: (a) end restraint conditions considered; (b) replacements of redundant boundary conditions by statically equivalent reaction forces and moments

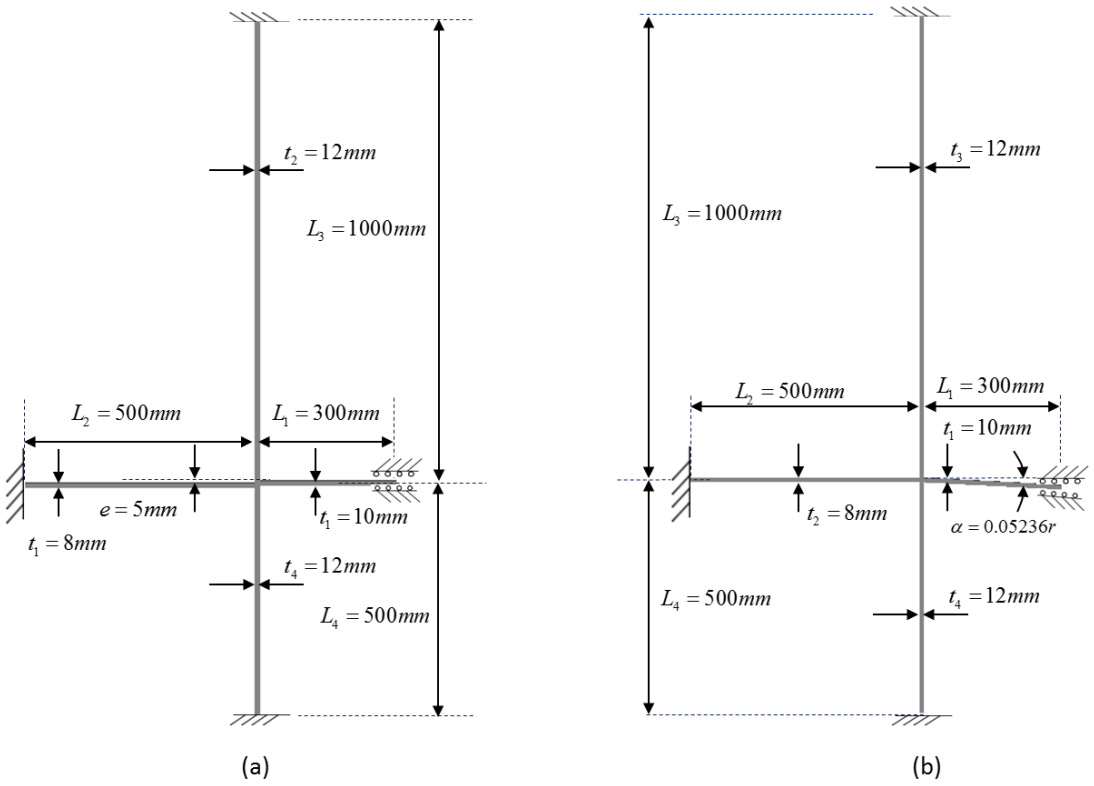

Figure 3.4: Finite element beam models used for verifying analytical formulation developed: (a) axial misalignment; (b) angular misalignment

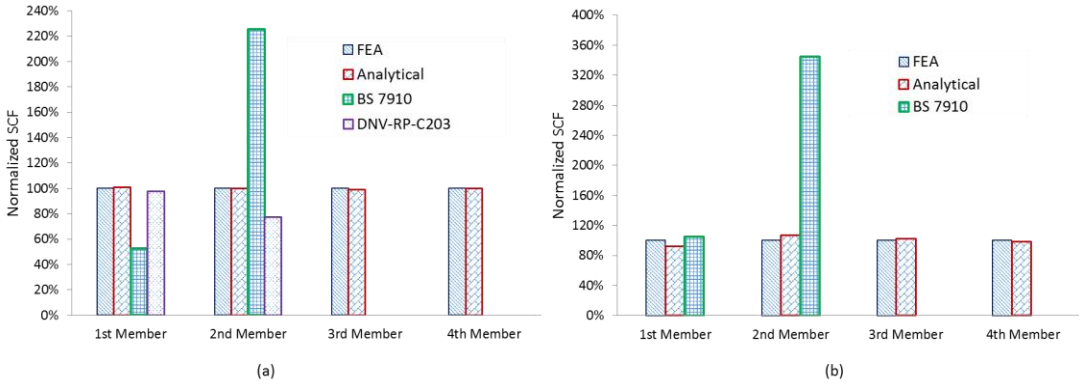

Figure 3.5: Comparison of normalized SCFs among FEA, analytical, BS 7910, DNV-RP-C203: (a) axial misalignment; (b) angular misalignment

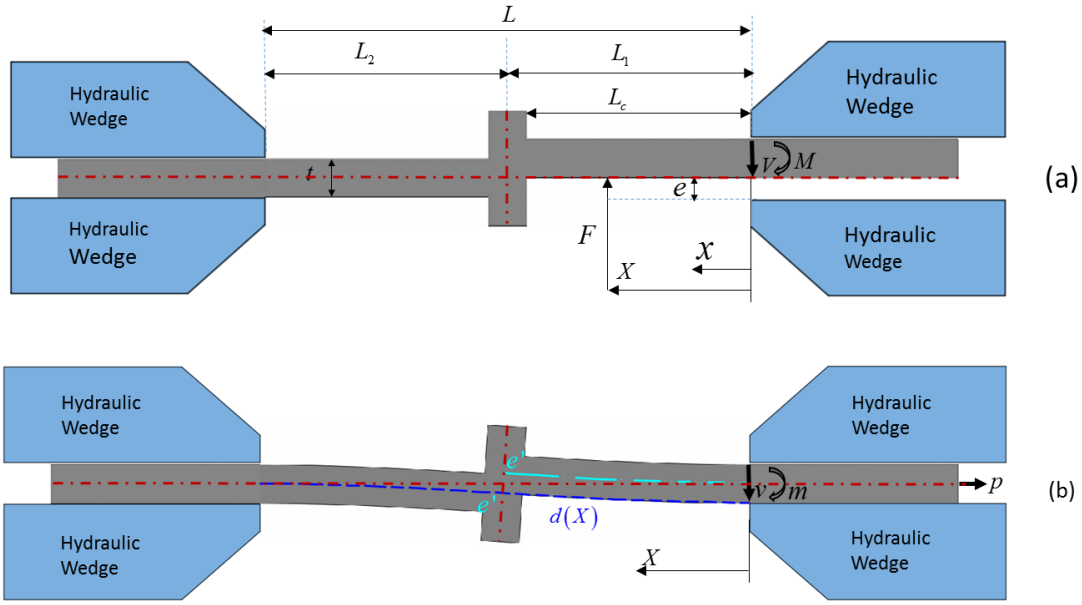

Figure 3.6: Cruciform joint with axial misalignment: (a) dimensions and shape before clamping; (b) deformed shape after clamping

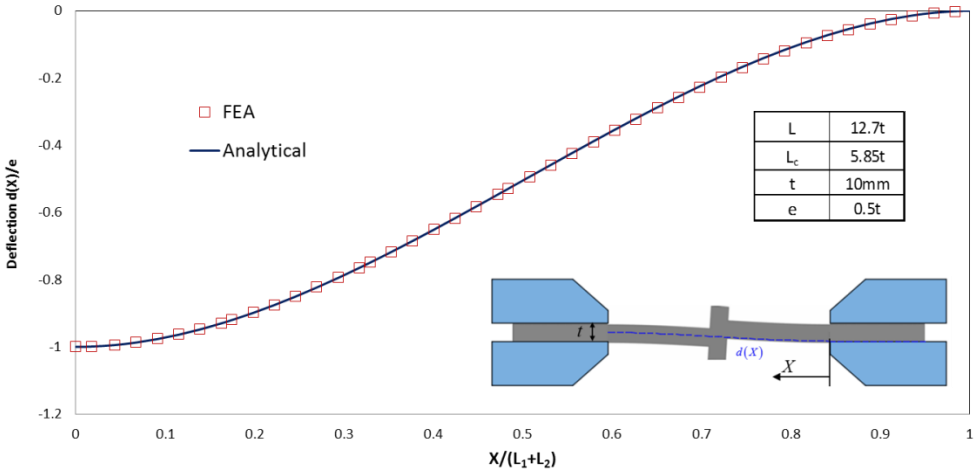

Figure 3.7: Comparison of analytical and FE solutions for a cruciform fillet welded fatigue specimen with axial misalignment *e*

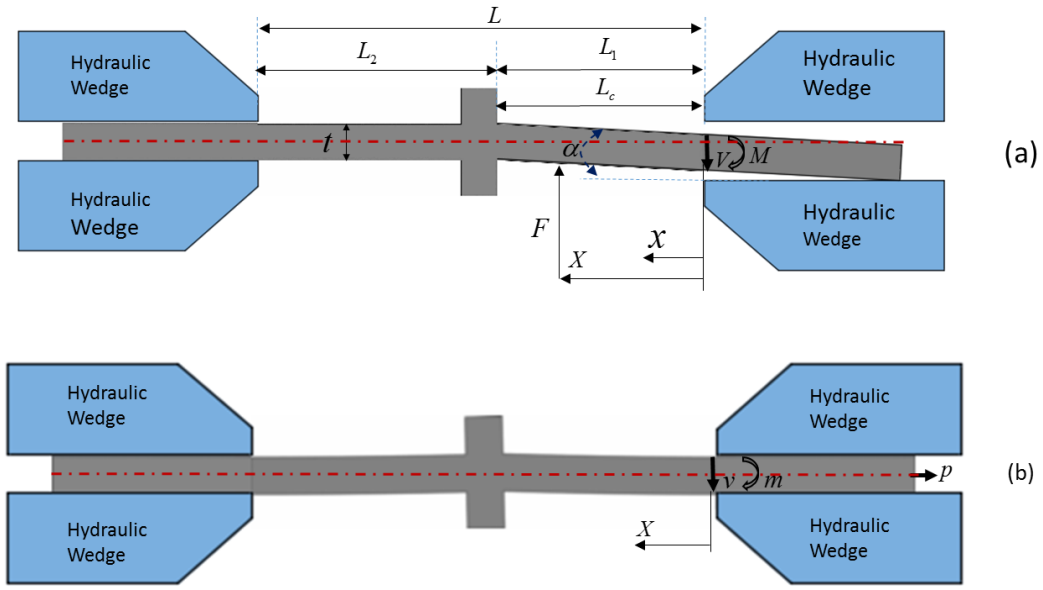

Figure 3.8: Cruciform joint with angular misalignment: (a) dimensions and shape before clamping; (b) deformed shape after clamping

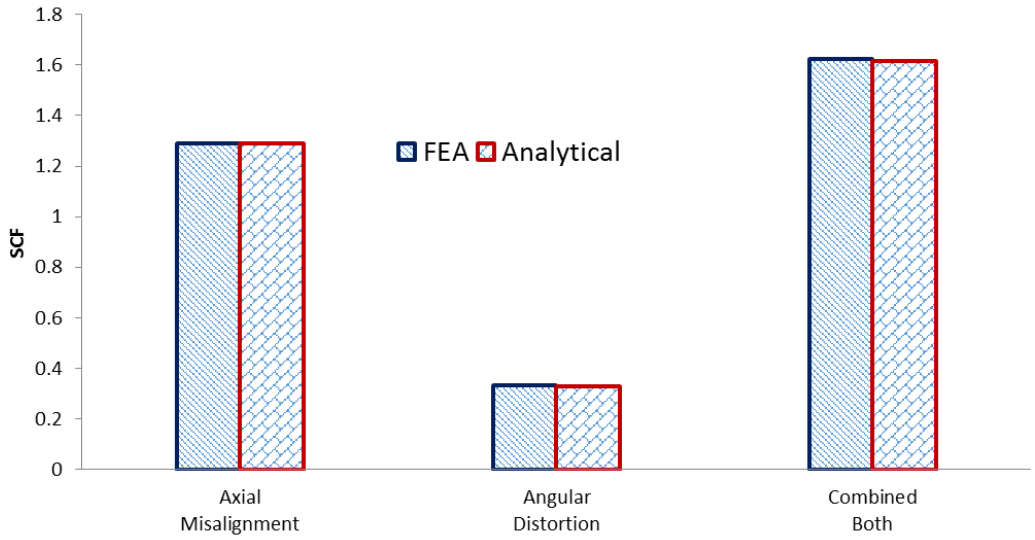

Figure 3.9: Comparison of SCFs computed by FE method and analytical solutions applications in fatigue test data interpretation

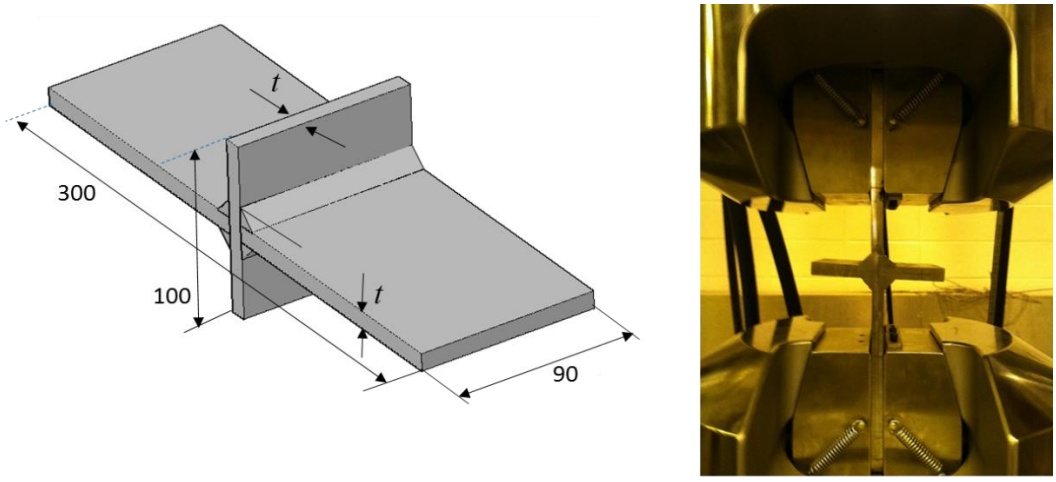

Figure 3.10: fatigue test specimen: (a) fatigue specimen geometry; (b) an actual test specimen mounted in fatigue test machine

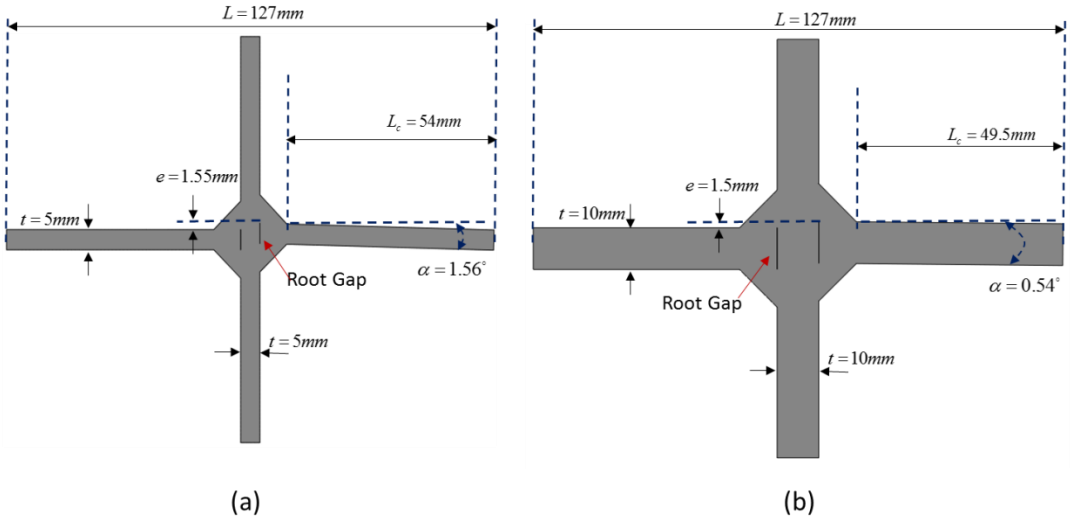

Figure 3.11: Illustration of dimensional relationships between actual test specimens and analytical model (see Figure 3.6 or Figure 3.8): (a) Specimen UM-A19; (b) Specimen UM-B13

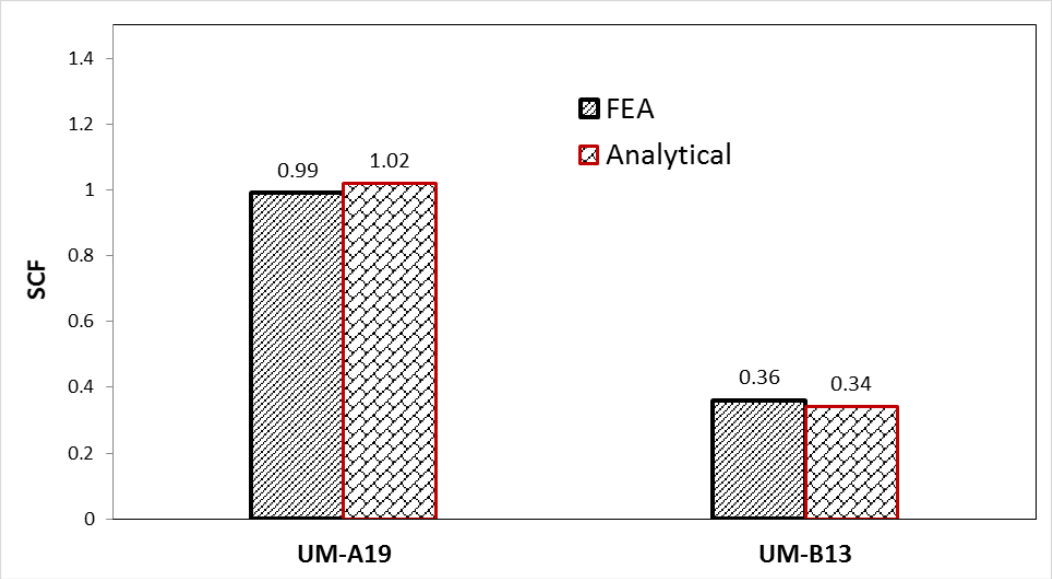

Figure 3.12: Comparison of SCF results calculated by FEA and analytical method for two specimens shown in Figure 3.11

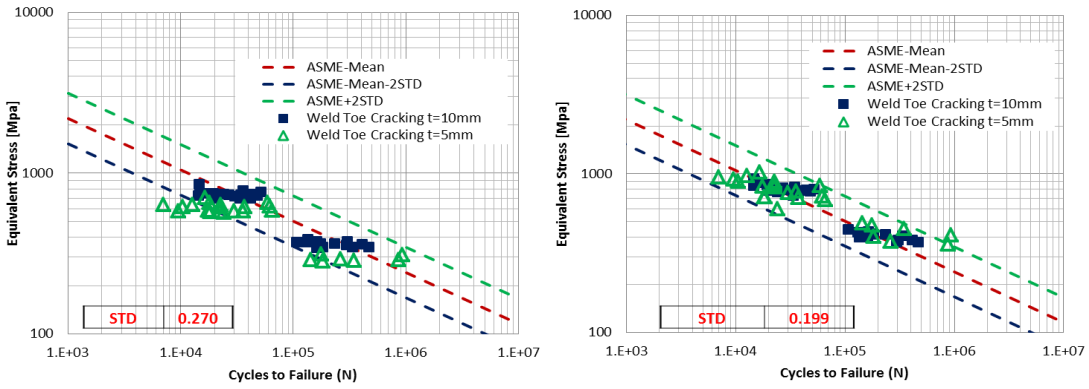

Figure 3.13: Analysis of fatigue test data: (a) without considering misalignments; (b) with considering misalignments using analytically derived SCFs given in Table B1

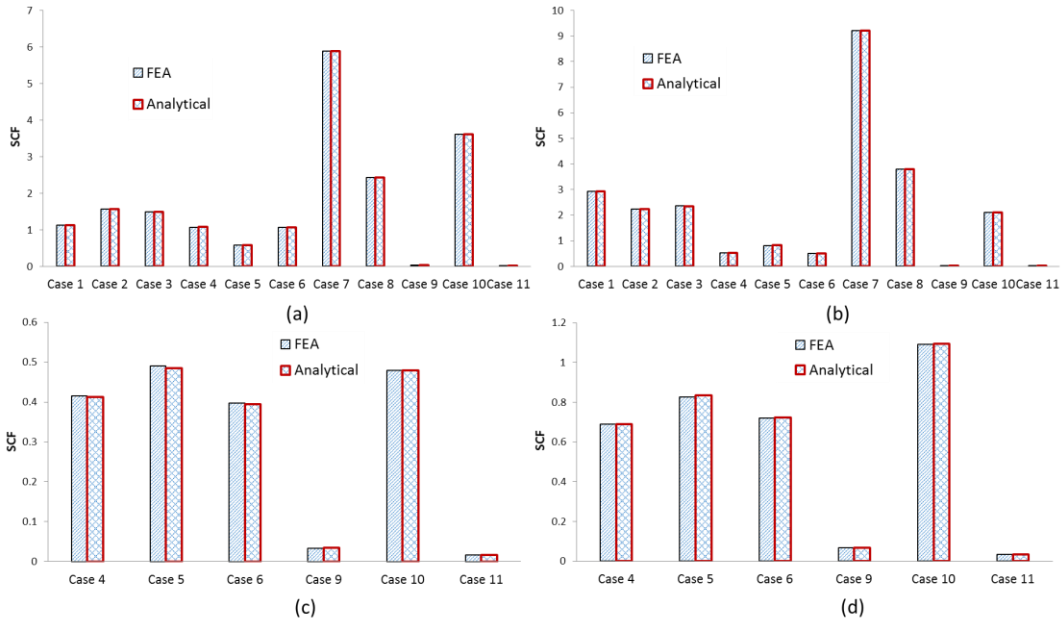

Figure 3A. 1: FEA validation of Analytical SCF solutions: (a) SCFs on 1st member section; (b) SCFs on 2nd member section; (c) SCFs on 3rd member section; (d) SCFs on 4th member section

Acknowledgment

The authors acknowledge the support of this work through a grant from the National Research Foundation of Korea (NRF) Gant funded by the Korea government (MEST) through GCRC-SOP at University of Michigan under Project 2-1: Reliability and Strength Assessment of Core Parts and Material System.

References

[1] Dong, P., and F. W. Brust. "Welding residual stresses and effects on fracture in pressure vessel and piping components: a millennium review and beyond." Journal of Pressure Vessel Technology 122.3 (2000): 329-338.

[2] Huang, T. D., et al. "Reduction of Overwelding and Distortion for Naval Surface Combatants, Part 1: Optimized Weld Sizing for Lightweight Ship Structures." Journal of Ship Production and Design 30.4 (2014): 184-193.

[3] Xing, S., et al. “Analysis of Fatigue Failure Mode Transition in Load-Carrying Fillet-Welded Connections”, submitted to Marine Structures

[4] Berge, S., and H. Myhre. "Fatigue strength of misaligned cruciform and butt joints." Norwegian Maritime Research 5.1 (1977).

[5] Andrews, R. M. "The effect of misalignment on the fatigue strength of welded cruciform joints." Fatigue & Fracture of Engineering Materials & Structures 19.6 (1996): 755-768.

[6] Jakubczak, H., and G. Glinka. "Fatigue analysis of manufacturing defects in weldments." International journal of fatigue 8.2 (1986): 51-57.

[7] Wylde, J. G., and S. J. Maddox. "Effect of misalignment on fatigue strength of transverse butt welded joints." Significance of deviations from design shapes (1979).

[8] BSI, BS. "7910: Guide on methods for assessing the acceptability of flaws in metallic structures." British Standards Institute (2013).

[9] BS7608, British Standard. "Code of practice for fatigue design and assessment of steel structures." British Standards Institution (1993).

[10] Veritas, Det Norske. "Fatigue design of offshore steel structures." No. DNV-RP-C203 (2011)

[11] Dong, P. "A structural stress definition and numerical implementation for fatigue analysis of welded joints." International Journal of Fatigue 23.10 (2001): 865-876

[12] Dong, P. "A robust structural stress method for fatigue analysis of offshore/marine structures." Journal of Offshore Mechanics and Arctic Engineering 127.1 (2005): 68-74.

[13] Dong, P., et al. "THE MASTER SN CURVE METHOD AN IMPLEMENTATION FOR FATIGUE EVALUATION OF WELDED COMPONENTS IN THE ASME B&PV CODE, SECTION VIII, DIVISION 2 AND API 579-1/ASME FFS-1." Welding Research Council Bulletin 523 (2010).

[14] Dong, P., et al. "A structural strain method for low-cycle fatigue evaluation of

welded components." International Journal of Pressure Vessels and Piping119 (2014): 39-51.
[15] ABAQUS, 2012, User's Manual, Version 6.12
[16] ASME Boiler and Pressure Vessel Code, Section VIII, Division 2, 2007.
[17] API 579 RP-1/ASME FFS-1, Fitness-For-Service, 200

Chapter 4
Fatigue Analysis of TIG and MIG Fillet-Welded Titanium Components Using a Traction Stress Method

Abstract

Fatigue testing of both TIG and MIG welded titanium components was first carried out using fillet welded cruciform specimens. A mesh-insensitive traction based structural stress definition and thickness correction factor are then introduced for achieving data transferability from one joint geometry to another and one base plate thickness to another. In addition to fatigue test data obtained in this study, test data from literature are then analyzed using the traction stress parameter developed. Major findings are:

(a) Fatigue behaviors of Ti-CP and Ti-6-4 weldments can be described by the same S-N curve for a given joint type and base plate thickness

(b) The proposed traction stress parameter with a thickness correction term can be used to effectively correlate lab specimen test data in the form of a single S-N curve with a narrow scatter band regardless of joint type and base late plate thickness, which has been demonstrated for both MIG and TIG weldment test data obtained in this study and data reported in the literature

(c) The validity of the thickness-corrected traction stress parameter is further confirmed by its ability in correlating full-scale structural component tests with lab specimen test data.

Keywords: Titanium weldments; fatigue testing; fatigue life prediction; traction structural

stress method; finite element; cruciform joints

4.1 Introduction

Titanium and its alloys have been mostly used in aerospace industry due to their high strength to weight ratios and excellent resistance to corrosion environment [1]. For offshore structures, titanium and its alloys have been used for applications where lightweight, resistances to fatigue and corrosion are important, such as risers, as discussed by Baxter et al. [2]. To facilitate titanium riser design, Baxter et al. [2] proposed a fatigue design S-N curve which was referred to as RMI-Stolt design curve in 1997, with limited support data obtained using a set of fatigue tests of dog-bone shaped specimens with weld cap being ground flush. Subsequently, Salama et al. [3] proposed a design S-N curve by down-shifting smooth bar based S-N curve used by aerospace industry by one standard deviation to accommodate effects of "infrequently occurring defects" in Ti-6-4 (Grade 5) welded joints. He demonstrated the proposed design S-N curve was sufficiently conservative by carrying out fatigue tests using dog-bone shaped specimens in both air and seawater environment [3].

More recently, Berge et al. [4] showed that both RMI-Stolt design S-N curve and the one proposed by Salama were not sufficiently conservative by comparing with their fatigue test results [5]. Thus, Berge et al. [4] suggested a more conservative design S-N curve, referred to as MARINTEK design curve. They [4] also carried out a series of fatigue tests for investigating the effects of titanium alloy grades (i.e., Grade 28 and Grade 29). They used hourglass-shape test specimens, extracted through water jet cutting process from a riser pipe section. The test results showed that the difference between the two grades of titanium alloys was rather small. They demonstrated that MARINETEK

design curve was conservative for use in fatigue design of risers. This was further supported by dog-bone specimen test results on Grade 23 with specimens extracted from a welded pipe section [6]. In order to establish a basis for accessing significance of weld defects, Salama [7] reviewed available crack growth data on Ti-6-4 available at that time from about 20 laboratories including data from base metal and welded joints. As a result, two crack growth curves for offshore applications: one has an exponent of 3.75 using data processing procedure given in BSI PD 6493 (now referred to as BS 7910 [8]) and the other with an exponent of 3.2 based on linear regression analysis of test data.

In recent years, titanium has been shown to be increasingly attractive for ship hull applications for achieving lightweight and reducing total ownership cost, as discussed by Dong et al. [9]. However, unlike other hull materials such as structural steel and aluminum alloys, lack of comprehensive test data for supporting structural design is one major challenge for adopting titanium and its alloys for marine structure applications. It should be pointed out here that all test data described above for supporting riser design [2-6] were obtained using small dog-bone specimens in which weld cap and root are ground-smooth and therefore not directly applicable for ship hull structure applications. To address such a need, Iwata and Matsuoka [10] carried out a series of fatigue tests for weldments made of commercial pure titanium i.e. Grade 2 (denoted as Ti-CP hereafter), including transverse butt-welded plate, cruciform fillet-welded, and longitudinal gusset specimens. TIG welding process was used in manufacture of these specimens. The resulting test data were represented in the form of nominal stress range versus cycle to failure and were shown to follow three separate trend lines, each with significant scatter band. Their investigation suggests that a weld classification approach [11] could still be

used for fatigue design of titanium structures, however, requiring a great deal of more test data from different joint geometries and loading conditions. To meet industry's needs, AWS recommended a series of design fatigue curves for titanium weldments referred to as "FAT Classes" in its D1.9 [12] with a S-N curve slope of 3.5 in log-log plot. In addition to the empirical nature of these FAT Classes in D1.9, joint types and loading conditions are rather limited for applications in complex structures.

In this study, we first start with an experimental investigation into fatigue behavior of titanium weldments made of Ti-CP (Grade 2) and Ti-6-4 (Grade 5) using cruciform specimens. Two types of welding processes are considered: Gas Tungsten Arc (TIG) and Metal Inert Gas (MIG) welding. To establish data transferability among different joint types and plate thicknesses, a mesh-insensitive traction stress parameter is then introduced. With this traction stress based parameter, both tests performed in this investigation and those available from literature are shown to follow a consistent trend line, demonstrating data transferability. Therefore, exhaustive testing can be avoided for developing design S-N curve for practical applications. Further validation of the present approach is then demonstrated by providing satisfactory fatigue life prediction of a number of full scale tests on MIG welded structural components.

4.2 Fatigue Testing

4.2.1 Materials, Specimen Design and Preparation

Both commercially pure titanium (Ti-CP) and titanium alloy (Ti-6-4) are considered here for fatigue testing as a follow up study to one reported by Dong et al. [9] on titanium ship hull structures. The mechanical properties as tested in this study are summarized in Table 4-1. The overall specimen dimensions are given in Figure 4.1, in

which each individual specimen (of non-load-carrying fillet weld type) was extracted from a cruciform block containing a total seven specimens under the same welding conditions. Both TIG and MIG weld size definitions are illustrated in Figure 4.1b and Figure 4.1c, respectively. Note that the TIG weld size definition used here follows the definition given in AWS B4 [15] for treating concaved fillet weld profile. All specimen details are given in Table 4-2, with a total of 63 test specimens. The narrow strips on both sides of the welded blocks shown in Figure 4.1a were used as weld macro specimens for examining fusion zone profile and fillet weld size. Representative macrographs showing fillet weld details are given in Figure 4.2. Based on observations on weld macros (Figure 4.2b), all TIG fillet weld profiles are defined as a quarter circle (i.e. a 90 degree arc) for consistently modeling and evaluating stress at weld toe. As such, the radius R can be related to weld size s as $R = s/\left(2-\sqrt{2}\right)$.

4.2.2 Test Procedure

All fatigue tests were performed using a MTS test machine with a load capacity 200 *KIPs* equipped with MTS 647 hydraulic wedge grips, as shown in Figure 4.3, in which a test specimen was in a loaded configuration. An applied stress ratio of 0.1 was used for all specimens under load-controlled conditions with a cyclic frequency of 5-8 *Hz*, depending upon specimen thickness being tested. During testing, both peak load range and displacement range were monitored and recorded. In all test specimens, final failure is defined as when specimen stiffness is reduced by 50% or complete separation, whichever occurred first.

4.2.3 Test Results

Among the total number of specimens listed in Table 4-2, five failed at base metal

away from welds and seven of which did not fail after running over *2* million cycles were considered as run-outs. The rest of the specimens failed at weld toe, which a focus of this study. The actual test results are summarized in Table 4A- 1 in Appendix 4-A. The nominal stress based S-N plot of all test results are given in Figure 4.4 for TIG welded joints and Figure 4.5 for MIG welded joint, respectively. Note that TIG weld test data by Iwata and Matsuoka [10] are also included in Figure 4.4 for comparison purposes, which also include TIG-welded longitudinal gusset specimens [10], as depicted in Figure 4.6a, in addition to cruciform specimens shown in Figure 4.6b. Each of the two joint types was tested with *2mm* and *10mm* base plate thicknesses. Not surprisingly, the scatter bands seen in Figure 4.4and Figure 4.5 are significant in terms of nominal stress range versus cycle to failure, due to the fact that nominal stresses are not capable of capturing plate thickness and joint geometry effects on fatigue, as discussed in numerous publications [16-17, 19-21]. As a result, an effective stress parameter must be introduced for effectively extracting fatigue properties for design and analysis of welded titanium structures without relying on exhaustive testing on thickness and joint geometry effect, as discussed in the next section. This is particularly important for titanium and its alloys, due to its significantly higher material cost than conventional structural steels and aluminum alloys.

4.3 Analysis

4.3.1 Stress Concentration Analysis

To effectively correlate the test data shown in Figure 4.4for TIG-welded joints and Figure 4.5for MIG-welded joints, a reliable stress concentration factor calculation procedure must be introduced, which should demonstrate mesh-insensitivity when finite

element method is used. For MIG-welded components in which a sharp notch is typically assumed at weld toe, the mesh-insensitive structural stress method (also referred to as traction structural stress method) has been proven effective (see [16-22]. For TIG-welded components, in which fillet weld profile can be represented by a well-defined radius tangential to base plate (see Figure 4.2b), the effectiveness of the traction structural stress method remains to be demonstrated. In what follows, we will briefly outline the traction structural stress method with a specific emphasis on how it is applied for the joint types of interest in this study and demonstrate its robustness in correlating fatigue test data presented in the previous section.

4.3.1.1 Traction Structural Stress Method

As discussed in [17-19], a through-thickness normal traction structural stress component (σ_s) can be decomposed into its statically-equivalent membrane (σ_m) and bending (σ_b) parts. For general 3D stress state, there exist two other traction stress components, in-plane shear (τ_L) and transverse shear (τ_T), in which transverse shear traction stress only contains membrane part in the context of structural mechanics. The use of all three traction components has been demonstrated in [23-24] for treating multiaxial fatigue under proportional [23] and non-proportional loading [24]. In view of the joint types and loading conditions involved in the present study (see Figure 4.2 and Figure 4.6) normal traction stress σ_s (Figure 4.7) is the dominant component and other two components are negligible (e.g., see [16]).

The corresponding finite element calculation procedure for extracting normal structural stress component is illustrated in Figure 4.8. Along a though-thickness hypothetical cut plane at a weld toe (corresponding to weld toe cracking, see [21]), nodal

forces normal to the cut plane exposed are extracted, as shown in Figure 4.8b. These nodal forces are then translated in *z'* direction to the mid-thickness positions, which are accompanied by statically equivalent moments shown in Figure 4.8c. Note that *x'-y'-z'* represents a local coordinate system defined with respect to the cut surface along weld toe line. The resulting nodal forces and resulting moments acting along the plate mid-thickness can be shown being related to work-equivalent line forces and line moments (see [17 and 19]) in a matrix equation. For instance, normal nodal forces can be related to line forces in *y'* direction as:

$$\begin{Bmatrix} F_1 \\ F_2 \\ F_3 \\ \vdots \\ \vdots \\ F_n \end{Bmatrix} = \begin{bmatrix} \frac{l_1}{3} & \frac{l_1}{6} & 0 & 0 & \cdots & 0 \\ \frac{l_1}{6} & \frac{l_1+l_2}{3} & \frac{l_2}{6} & 0 & \cdots & 0 \\ 0 & \frac{l_2}{6} & \frac{l_2+l_3}{3} & \frac{l_3}{6} & 0 & 0 \\ 0 & 0 & \ddots & \ddots & \ddots & 0 \\ \vdots & \ddots & \ddots & \ddots & \frac{l_{n-2}+l_{n-1}}{3} & \frac{l_{n-1}}{6} \\ 0 & \cdots & \cdots & 0 & \frac{l_{n-1}}{6} & \frac{l_{n-1}}{3} \end{bmatrix} \begin{Bmatrix} f_1 \\ f_2 \\ f_3 \\ \vdots \\ \vdots \\ f_n \end{Bmatrix} \tag{4.1}$$

where F_1 , F_2 , …, F_n are nodal forces as depicted in Figure 4.8c in y' direction in the local coordinate system. Line forces f_1 , f_2 , …, f_n can be solved by inverting the matrix equation Eq. (4.1). In the same manner, nodal moments can be treated in the same way by simply replacing F_1 , F_2 , …, F_n with nodal moments M_1 , M_2 , …, M_n about x'. It should be noted that Eq. (4.1) was derived for linear FE model [17]. For parabolic elements, a similar matrix equation is also given in [17]. Then, the normal traction stress can be calculated in terms of its membrane and bending parts at each node position (depicted in Figure 4.8c) as:

$$\sigma_s = \sigma_m + \sigma_b = \frac{f_{y'}}{t} - \frac{6m_{x'}}{t^2} \tag{4.2}$$

4.3.1.2 Stress Concentration Calculation Results

4.3.1.2.1 Longitudinal Gusset Joint (TIG)

The longitudinal gusset joints tested by Iwata and Matsuoka[10] were modeled here as 3D solid element models shown in Figure 4.9 for base plate thicknesses of *2mm* and *10mm*, respectively. Only was one-eighth of the joint geometry modeled for each by taking advantage of symmetries. Note that TIG fillet weld sizes were not explicitly given in [10] and is estimated as having a radius of *8.5mm* (or $R \approx 8.5mm$) which gives an equivalent fillet size of *s=5mm* for 10*mm* base plate thickness (as defined in AWS B4 [15] and discussed in Sec. 4.2.1), *s=3mm* for 2*mm* base plate thickness. These weld size estimates were also consistent with the minimum fillet weld size requirements given in AWS D 1.1[25]. ABAQUS [26] was used for performing all finite element analyses (FEA) in this study. Upon completion of each FEA, nodal forces collected along the cut surface at weld toe line were transformed into local coordinate system *x'-y'-z'* (see Figure 4.8b and Figure 4.8c). Then, Eq. (4.1) in combination with Eq. (4.2) yields normal membrane, bending, and total stresses (membrane plus bending) along weld toe plane, as shown in Figure 4.10, in which traction based stress concentration factor (SCF) is defined as traction structural stress calculated at each position along the hypothetical cut at weld toe line divided by uniform remote nominal stress applied at the specimen ends. The traction stresses so calculated has been proven insensitive to element size and element types, as proven for a variety of joint types, loading mode, and complex components documented in [17], which will not be further discussed here due to space limitation.

As expected, the highest stress concentration in each case is located at the weld

toe position (labeled as “critical location”) at the end of the gusset plate, as shown in Figure 4.10. It is important to note that the membrane stress SCF for the gusset joint with *2mm* thickness base plate is significantly higher than the joint with *10mm* base plate thickness, while bending stress SCF is very close to each other. This suggests that thin plate joint is more sensitive to stiffness change due to the presence of longitudinal gusset than thick plate, as expected. The ability of partitioning membrane and bending stress concentration factors is unique to the traction structural stress procedure. Other stress concentration calculation procedures such as notch stress methods with an assumed notch radius [27], surface extrapolation based hot spot stress methods [28] are not capable of providing such partitioning, in addition to their sensitivity to notch radius in the former and element size in the latter.

4.3.1.2.2 Cruciform Fillet Joints

Traction stress based SCFs for cruciform joints shown in Figure 4.1 and Figure 4.6 can be solved in the same manner using 3D solid element models by means of Eqs. (4.1) and (4.2). Since such joints are essentially two dimensional (2D) stress analysis problems, the nodal force based traction stress method described in Figure 4.8 can be implemented in a more straight-forward manner with respect to 2D FE models, as illustrated in Figure 4.11 for TIG welded cruciform joints (Figure 4.11a) and MIG-welded joints (Figure 4.11b), respectively. In doing so, major differences between the traction structural stress and conventional surface stress methods can be more effectively illustrated and contrasted.

Consider the case for TIG-welded joint in Figure 4.11a, once nodal forces acting on the cut line (or plane) with respect to the element group shown in Figure 4.11a, both

statically-equivalent membrane stress σ_m and bending stress σ_b defined in Eq. (4.2) can be simply obtained, in a statically equivalent manner, as follows:

$$\sigma_m = \frac{\sum_{i=1}^{n} F_{xi}}{t} \tag{4.3}$$

$$\sigma_b = \frac{6\sum_{i=1}^{n} F_{xi}\left(y_i - \frac{t}{2}\right)}{t^2} \tag{4.4}$$

where, F_{xi} are nodal forces at node i in element group (Figure 4.11) with respect to the coordinate system (*x*- *y* -*z*) depicted in Figure 4.11.

The results are summarized in Figure 4.12 to Figure 4.13 using FE models with different element sizes, varying from $0.025t \times 0.025t$ up to $0.5t \times 1t$. For comparison purpose, surface stresses in the loading direction (*x*) directly extracted from FE results (all with parabolic element type "CPE8R" in ABAQUS [26]) at weld toe position (i.e., at tangent point for TIG welded joints) are also shown in the same figure. As can be seen, the traction structural stress method offers a remarkable mesh-size insensitivity in SCF calculations in both TIG (Figure 4.12) and MIG (Figure 4.13) welded joints, while surface stress based SCF shows a clear sensitivity, which is well known (see [17, 19] for MIG welded joints. For TIG welded joints, although the same weld cap radius was adequately represented by the parabolic elements in all models shown in Figure 4.13, the sensitivity of the SCF results at weld toe (tangent point) to element size is still rather obvious for element size of about $0.05t \times 0.05t$ or larger. This suggests that even for well-defined weld toe radius such as TIG welded joints, an element size in the order to $0.05t \times 0.05t$ or less would be required for consistently calculating surface stress based SCF using conventional methods. The traction stress method, in addition to its proven

mesh-insensitivity for computing SCF in MIG welded joints, still offers a significant advantage over the traditional methods for modeling TIG welded joints, as shown in Figure 4.12.

To facilitate fatigue test data analysis in this study, traction stress based SCF as a function of relative fillet size (*s/t*) from 0.5 to 1.2 are shown in Figure 4.14 for both TIG- and MIG-welded cruciform joints. As can be seen in Figure 4.14, traction stress based SCF shows a slight increase as fillet size increases from 0.5 to about 0.8 or 0.9 and then becomes stabilized for MIG-welded cruciform joints and a slight decrease for TIG-welded cruciform joints considered in this study.

4.3.2 Treatment of Thickness Effects

As discussed by numerous researchers over the last few decades [e.g. 29-30], fatigue life of welded joints can be treated as crack propagation life. As such, Dong and his co-workers [31-32] have showed that Mode I stress intensity factor (K) for weld toe cracking can be expressed in terms of the membrane and bending traction stresses as:

$$\Delta K = \Delta\sigma_s \sqrt{t}\left[f_m(a') - r(f_m(a') - f_b(a')\right] \tag{4.5}$$

where, $\Delta\sigma_s = \Delta\sigma_m + \Delta\sigma_b$, $r = \Delta\sigma_b / \Delta\sigma_s$, $f_m(a')$ and $f_b(a')$ are dimensionless compliance functions (given in closed-form solutions in [33])) and only dependent on relative crack size $a' = a/t$, where a is crack depth into plate thickness t at a weld toe location of interest. Invoking classical Paris law and integrating over from an initial crack size a_i' to a final crack size a_f', one obtains:

$$N = \frac{t}{t^{m/2}(\Delta\sigma_s)^m} \int_{a_i'}^{a_f'} \frac{da'}{C\left[f_m(a') - r(f_m(a') - f_b(a')\right]^m} \tag{4.6}$$

where exponent *m* is the slope of $da/dN - \Delta K$ curve in log-log plot, which has a value of

about 3.6 based on analysis of a large amount of crack growth rate data (see[16). For Ti-CP and Ti-6-4, as discussed in Sec. 4.1, *m* may vary between 3.2 and 3.75, depending upon data processing methods used, as discussed by Salama [7]. As a result, *m* =3.6 is chosen as an approximate average value in this study for data correlation purpose. Eq. (4.6) can be then rewritten as:

$$N = t^{\frac{2-m}{2}} (\Delta\sigma_s)^{-m} A(a_i', a_f', r, C) \tag{4.7}$$

where, $A(a_i', a_f', r, C)$ can be treated as a constant for the present purpose. Eq. (4.7) can be written as a traditional S-N curve form,

$$\frac{\Delta\sigma_s}{t^{\frac{2-m}{2m}}} \times N^{\frac{1}{m}} = \left[A(a_i', a_f', r, C) \right]^{\frac{1}{m}} \tag{4.8}$$

Therefore, a plate thickness corrected effective traction stress can be inferred from Eq. (4.8) as:

$$\Delta\sigma_e = \frac{\Delta\sigma_s}{t_c} \tag{4.9}$$

where, $t_c = t^{\frac{2-m}{2m}}$. Due to symmetry with respect to base plate mid-thickness in all joint types and loading conditions considered here, an effective thickness $t_e = t/2$ should be used (see [17]), resulting in $t_c = t_e^{\frac{2-m}{2m}}$, which will be used from this point on.

4.3.3 Analysis of S-N Test Data

The mesh-insensitivity nature of the traction structural stress method, as demonstrated in Sec. 4.3.1, suggests that stress concentration factors so calculated should uniquely describe the stress state at a location of interest (e.g., at weld toe), which can be related to joint type (e.g., cruciform fillet versus longitudinal gusset joints) and loading

modes (e.g., remote tension versus remote bending). Furthermore, effects of plate thickness (or size effects) on fatigue can be described by Eq.(4.9), as long as crack propagation dominates fatigue lives. Then, it follows that one should expect a reduced scatter band once the traction stress parameter and the thickness correction term (see Eq. (4.9)) are introduced.

4.3.3.1 TIG Weldment Data

All TIG weld data shown in Figure 4.4 are re-processed and plotted in Figure 4.15 in terms of traction stress range ($\Delta\sigma_s$) (see Figure 4.15a) which is calculated by multiplying SCF from Figure 4.14 for a given *s/t* and thickness-corrected effective traction stress range ($\Delta\sigma_s / t_c$) (see Figure 4.15b). As can be seen, when $\Delta\sigma_s$ is used (see Figure 4.15a), the resulting scatter band becomes significantly narrower than that in Figure 4.4, with a standard deviation being reduced to 0.291(see Figure 4.15a) from 0.411 in Figure 4.4, demonstrating the effectiveness of the traction stress parameter. Once the thickness correction term t_c is introduced, a further reduction in standard deviation, from 0.291 to 0.258 (see Figure 4.15b), proving the effectiveness of the thickness term derived in Sec. 4.3.2. it is worth emphasizing that the large scatter band in Figure 4.4 clearly shows the inability of the nominal stress in correlating fatigue test data. As a result, without an appropriate stress definition, simply introducing a thickness correction term t_c given in Eq. (4.9) with respect to nominal stress range proves to be ineffective in data correlation, as illustrated in Figure 2.16.

It is important to note that base metal (Ti-CP versus Ti-6-4) effects are negligible (see Figure 4.15b). This seems consistent with the fact that steel weldments follow essentially the same master S-N curve scatter band regardless of base metal strength

levels (from about 400MPa to 1000MPa in tensile strength) (see [21 and 27]).

4.3.3.2 MIG Weldment Data

MIG weld S-N data shown in Figure 4.5 can be analyzed in the same manner. The results in terms of the thickness-corrected traction stress range (see Eq. (4.9)) are shown in Figure 4.17, resulting in a reduction of a standard deviation from 0.238 in Figure 4.5 to 0.157 in Figure 4.17. This further confirms validity of the proposed effective traction stress parameter (Eq. (4.9)) when dealing titanium weldment fatigue data. Again, Figure 4.17 shows that the two base metal types (i.e., Ti-CP versus Ti-6-4) considered in this study fall into the same narrow scatter band, indicating that same S-N curve can be used fatigue evaluation purpose for dealing welded connections.

4.3.3.3 Applications for Structural Components

In addition to demonstrating data transferability of the lab fatigue tests from one joint type to another and one thickness to another, the ultimate goal of achieving effective data correlation is to demonstrate if fatigue lives of actual structural components can be reasonably estimated using the data from lab specimens. For this purpose, we will use a series of full scale welded beam tests performed by Patnaik et al. [13-14].

4.3.3.3.1 Descriptions of Full Scale Tests

Figure 4.18 shows full-scale titanium structural components made by MIG (Figure 4.18a) and testing conditions [13-14]. The overall dimensions are 686mm in total beam length, 76.2mm in flange width, and 98.4mm in web height. Other dimensions such as thicknesses as well as welding procedure details can be found in [13-14]. The tests were performed under four-point bending conditions with a setup shown in Figure 4.18b. A total of four components were tested, as summarized in Table 4-3. Out of the four, two

were made of Ti-CP labeled as “B5”, “B6”, the other two made of Ti-6-4 labeled as “B2”, “B3”. For components labeled as “B5” and “B6”, multiple load blocks were used with an increasing in amplitude, among which only “B6” was tested to failure. Therefore, there are a total of three full scale built-up test results that can be used for our validation study, i.e., “B2”, “B3”, and “B6”.

4.3.3.3.2 Traction Stress Determination

To make use of the three full scale tests, finite plate element models with a linear element size of about 0.5t were used in this study. The overall geometry of the full scale component is shown in Figure 4.19a, in which detailed FE mesh is not shown in order to highlight the critical weld location and weld line definition for using Eq. (4.1) with clarity. Two weld lines encompassing failure locations reported are evaluated as shown in Figure 4.19a. The traction structural stresses at nodal positions along each weld line were solved simultaneously through the system of linear equations given Eq. (4.1). It was found that the end position of Weld Line *1* possesses the highest traction structural stress among the two weld lines evaluated under given loading conditions. The corresponding traction stress distribution is shown in Figure 4.19b. Note that the resulting traction stresses shown in Figure 4.19b are computed under a reference load (1 KN), which can then be scaled to actual loads used in testing.

4.3.3.3.3 Structural versus Lab Specimen Test Results

The peak traction structural stress range calculated at the end of Weld Line *1* is then converted to effective stress range according to Eq. (4.9) for comparing with lab specimen test results discussed in early sections if under constant amplitude loading conditions in a log-log based $\Delta\sigma_e - N$ plot. This applies to Components B2 and B3 in

Table 3. Component B6 involved multiple loading blocks, a Miner's rule based effective traction stress with respect to the total loading cycles is used for data analysis purpose, i.e.,

$$\Delta\sigma_e = \left(\frac{1}{\sum n_i} \sum_{i=1}^{i=2} n_i \Delta\sigma_{e-i}^{\frac{1}{h}} \right)^h \tag{4.10}$$

where h represents the slope of S-N curve given in Figure 4.17, n_i and $\Delta\sigma_{e-i}$ are the number of cycles accumulated with i_{th} loading block and corresponding effective stress range according to Eq. (4.9), respectively.

Then, the structural component test results are inserted into Figure 4.17 and replotted in Figure 4.20 for clarity. It can be seen that all three tests are situated well within a scatter band defined by the mean plus/minus two standard deviations of lab specimen test data shown in Figure 4.17. The excellent agreement between full scale component tests and lab specimen tests seen in Figure 4.17 suggests that the lab specimen tests analyzed in this study provides not only transferability from one joint geometry to another and one plate thickness to another, but also offer a reasonable predictability for estimating fatigue lives for full-scale structural components. In doing so, the mesh-insensitive traction stress method serves as an enabler.

4.4 Discussions

4.4.1 TIG versus MIG

Comparing between Figure 4.15b (TIG welded joints) and Figure 4.17 (MIG welded joints), the scatter band for TIG welds is noticeably greater than MIG welds. The main reasons can be attributed to the following considerations:

(a) TIG weldment data considered in Figure 4.15b encompass different joint types (cruciform and longitudinal gusset joints) with base plate thickness varying from 2mm to 10mm. The data are two sources: test results from this study and those by Iwata and Matsuoka[10] given in [10]. In the latter, detailed weld size information and testing conditions such as failure criteria are not available. All these could have contributed to a greater variability seen in Figure 4.15b than that in Figure 4.17 for MIG welds which were all manufactured and tested as a part of this study under same controlled conditions.

(b) Although TIG weld profile can be approximated as a smooth arc being tangential to plate surface, actual fatigue crack development leading to final failure does not necessarily initiates at the tangential position, particularly in view of the fact visually insignificant surface (e.g., lack of smooth transition from weld cap to base metal surface) and sub-surface defects are unavoidable. Variation in cracking position near the tangent position from specimen to specimen could introduce additional variation in S-N data due to a change in SCF.

4.4.2 Ti-CP versus Ti-6-4

As discussed in Sec. 4.3.3, any effects of base material (i.e., Ti-CP versus Ti-6-4) on fatigue behavior are seen to be negligible, as shown in Figure 4.15 and Figure 4.17, even though the two base materials have significantly different yield and tensile strengths (see Table 4-1). Such a trend can be consistently observed in both TIG (see Figure 4.15) and MIG weld test results (see Figure 4.17). To further substantiate this observation, all cruciform joints shown in in Figure 4.15b and Figure 4.17 are replotted in Figure 4.21 by separating these data into two groups: Ti-CP versus Ti-6-4. Figure 4.21a shows all TIG

weldment data while Figure 4.21b shows all MIG weldment data. As it can be seen that both Ti-CP and Ti-6-4 data fall into essentially same scatter band in both cases. This is consistent with historical observations on large amount of steel weldment test data that have been used as a basis by well-known Codes and Standards for decades [8, 11, and 18].

4.5 Conclusions

Based on a systematic fatigue testing on TIG and MIG welded cruciform joints and data analysis using a new traction stress parameter, the following major conclusions can be drawn:

(a) Fatigue behaviors of Ti-CP and Ti-6-4 weldments can be described by the same S-N curve for a given joint type and base plate thickness

(b) The proposed thickness-corrected traction stress parameter can be used to effectively correlate lab specimen test data in the form of a single S-N curve with a narrow scatter band regardless joint type and base late plate thickness, which has been demonstrated for both MIG and TIG weldment test data performed in this study and reported in the literature

(c) The validity of the thickness-corrected traction stress parameter is further confirmed by its ability in correlating full-scale structural component test data with lab specimen test data

Appendix 4-A

Table 4A- 1: Fatigue test results

Specimen ID	Nominal Stress Range	Number of Cycles to Failure	Failure Location
A1	205	20900	Weld Toe
A2	88	468700	Weld Toe
A3	104	237800	Weld Toe
A4	205	16500	Weld Toe
A5	104	224200	Weld Toe
A6	140	52200	Weld Toe
A7	141	51200	Weld Toe
I1			Run Out
I2			Run Out
I3	206	100500	Weld Toe
I4	162	221600	Weld Toe
I5	299	12700	Weld Toe
I6	321	7700	Weld Toe
I7	350	6400	Weld Toe
K1			Run Out
K2	194	61000	Weld Toe
K3	193	59300	Weld Toe
K4	141	121000	Weld Toe
K5	141	123900	Weld Toe
K6	280	12200	Weld Toe
k7	340	5400	Weld Toe
L1	120	179100	Weld Toe
L2	144	138400	Weld Toe
L3	144	123800	Weld Toe
L4	190	58600	Weld Toe
L5	190	64900	Weld Toe
L6	235	27200	Weld Toe
L7	99	574700	Weld Toe
M1	201	83900	Weld Toe
M2	201	85600	Weld Toe
M3	126	389500	Weld Toe
M4	126	289500	Weld Toe
M5	244	31200	Weld Toe
M6	245	26900	Weld Toe
M7	105	1391200	Weld Toe

Specimen ID	Nominal Stress Range	Number of Cycles to Failure	Failure Location
C1			Base Metal
C2			Base Metal
C3	280	21000	Weld Toe
C4	280	34500	Weld Toe
C5	190	302900	Weld Toe
C6	155	855300	Weld Toe
C7	209	98700	Weld Toe
E1	182	959300	Weld Toe
E2			Run Out
E3			Run Out
E4	198	150700	Weld Toe
E5	284	59100	Weld Toe
E6	228	270000	Weld Toe
E7			Base Metal
F1	295	22400	Weld Toe
F2	295	23600	Weld Toe
F3	236	97900	Weld Toe
F4	207	220200	Weld Toe
F5	177	675400	Weld Toe
F6	148	341100	Weld Toe
F7			Run Out
G1	253	62200	Weld Toe
G2	253	59800	Weld Toe
G3			Base Metal
G4	197	184500	Weld Toe
G5			Run Out
G6			Base Metal
G7	169	268600	Weld Toe

Table 4-1: Tensile properties of base materials

Room Temperature Tensile Properties

Materials	Orientation	Yield Strength		Ultimate Strength		Elongation
		Ksi	MPa	Ksi	MPa	
Ti-CP	Rolling	50	342	73	505	9.7%
Ti-64	Rolling	126	869	149	1029	18.9%

Table 4-2: Test matrix

Group	Specimen ID							Process	Materials type	MATERIAL THICKNESS "t" (mm)	TARGET WELD SIZE "s" (mm)
A	A1	A2	A3	A4	A5	A6	A7	GMAW	TI CP2	13	7
C	C1	C2	C3	C4	C5	C6	C7	GTAW	TI CP2	5	3
E	E1	E2	E3	E4	E5	E6	E7	GTAW	TI CP2	6.5	3
F	F1	F2	F3	F4	F5	F6	F7	GTAW	TI 6-4	5	3
G	G1	G2	G3	G4	G5	G6	G7	GTAW	TI 6-4	5	3
I	I1	I2	I3	I4	I5	I6	I7	GMAW	TI CP2	5	3
K	K1	K2	K3	K4	K5	K6	K7	GMAW	TI CP2	7	5
L	L1	L2	L3	L4	L5	L6	L7	GMAW	TI 6-4	7	7
M	M1	M2	M3	M4	M5	M6	M7	GMAW	TI 6-4	5	4

Table 4-3: Summary of tested components

Speicmen (ID)	Material	Load Block	Load [KN]		Load Cycles [N]
			Max	Min	
B2	Ti-6-4	1st	111.00	11.10	25248 (failed)
B3	Ti-6-5	1st	111.00	11.10	30286 (failed)
B5	Ti-CP	1st	89.00	8.90	35,364
		2nd	36.00	3.60	1,000,000
		3rd	76.00	7.60	1000000 (not failed)
B6	Ti-CP	1st	76.00	7.60	1,000,000
		2nd	111.00	11.10	30000 (failed)

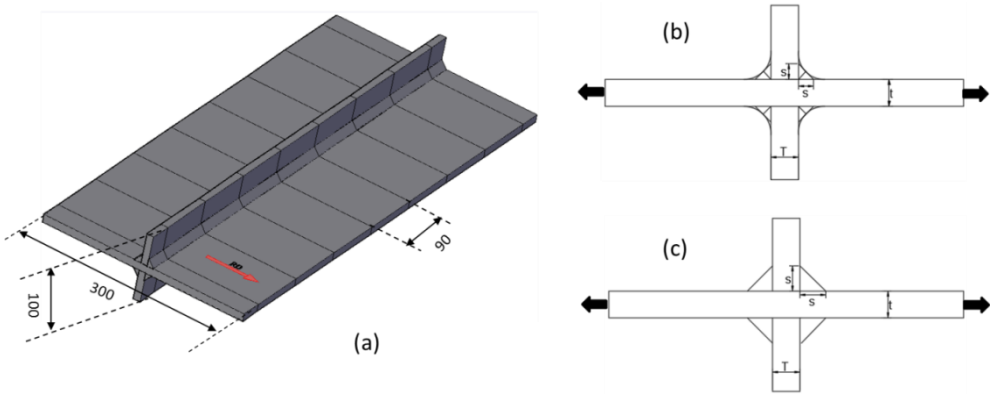

Figure 4.1: Cruciform test specimen geometry extracted from a block: (a) 3D view; (b) 2D cross section and weld size definitions of TIG welds; (c) 2D cross section and weld size definition of MIG welds

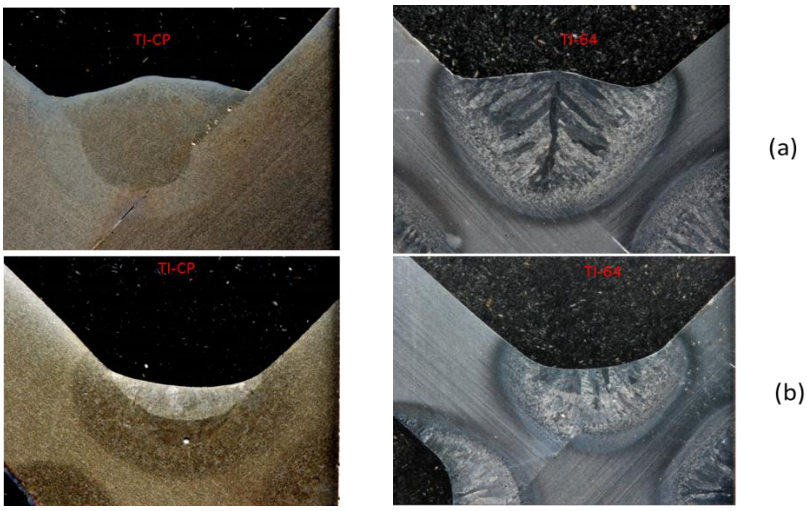

Figure 4.2: Representative weld macros for Ti-CP and Ti-6-4 weldments: (a) MIG welded specimens; (b) TIG welded Specimens

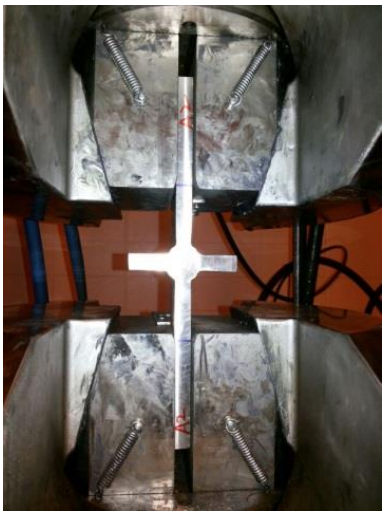

Figure 4.3: A titanium specimen in mounted configuration in hydraulic wedge grips in MTS test machine prior to fatigue testing

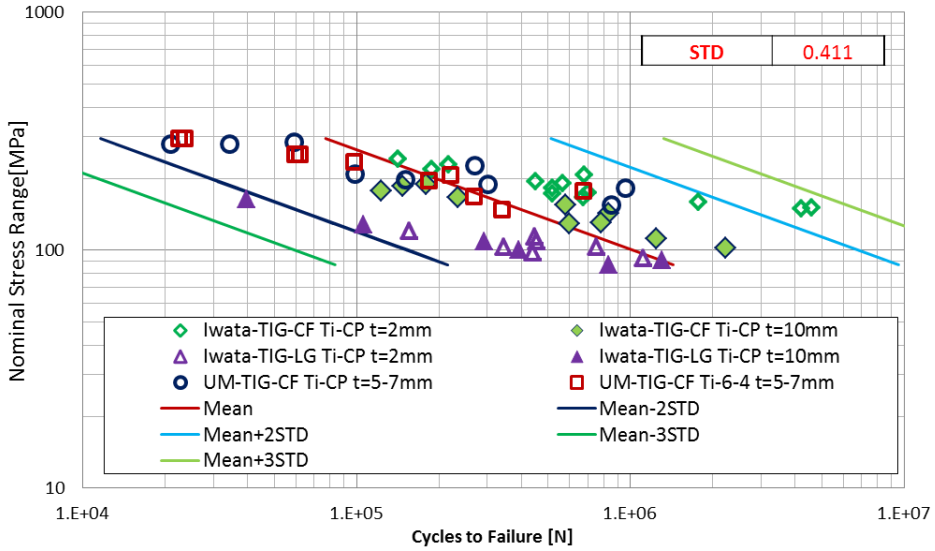

Figure 4.4: TIG weldment data: nominal stress range versus cycle to failure

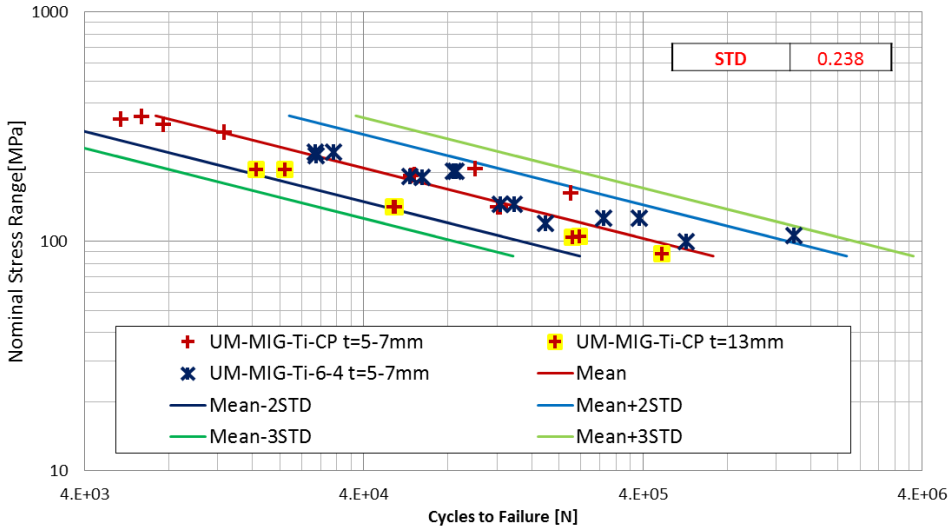

Figure 4.5: MIG weldment data: nominal stress versus cycle to failure

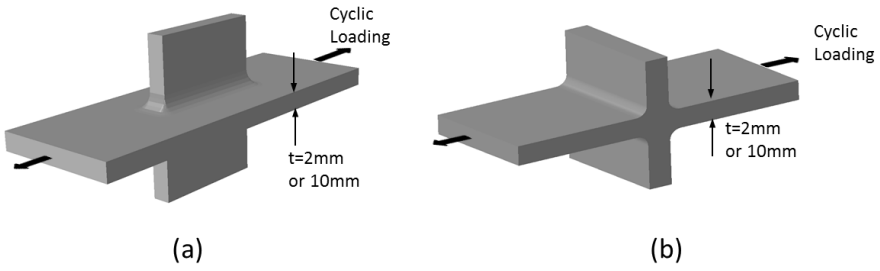

Figure 4.6: Joint geometry and cyclic loading conditions [10]: (a) TIG welded longitudinal gusset joint; (b) TIG welded cruciform joint;

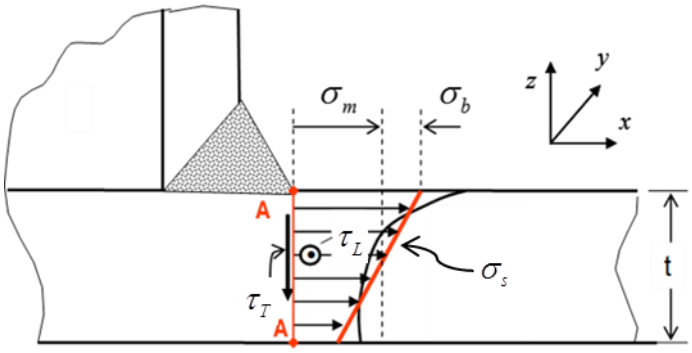

Figure 4.7: Traction structural stress definition

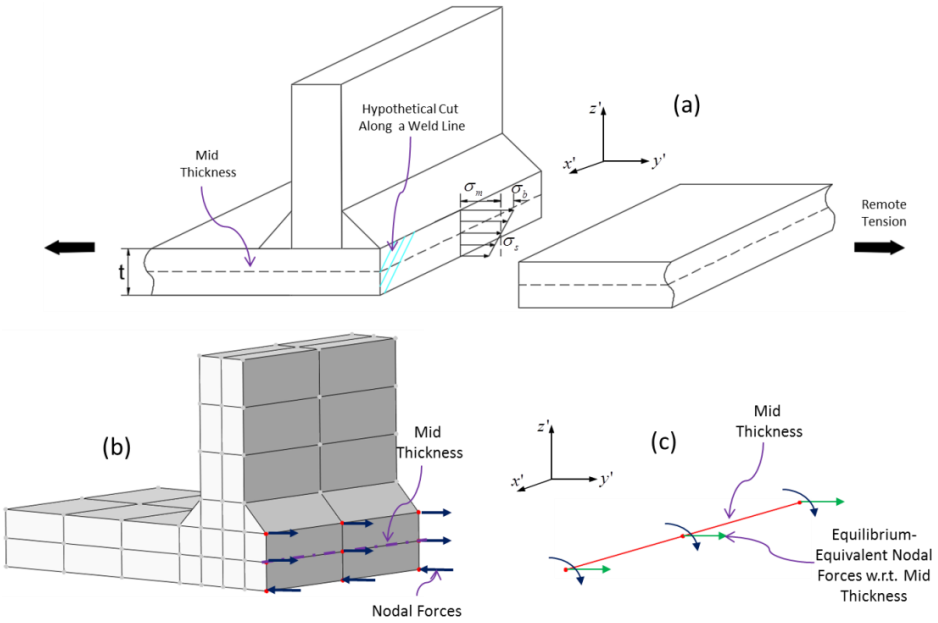

Figure 4.8: Through thickness traction stress definition and calculation procedure using 3D solid element model: (a) Linear traction stresses acting on a hypothetical cut at toe position; (b) nodal forces exposed; (c) statically equivalent nodal forces and moments acting on plate mid-thickness surface

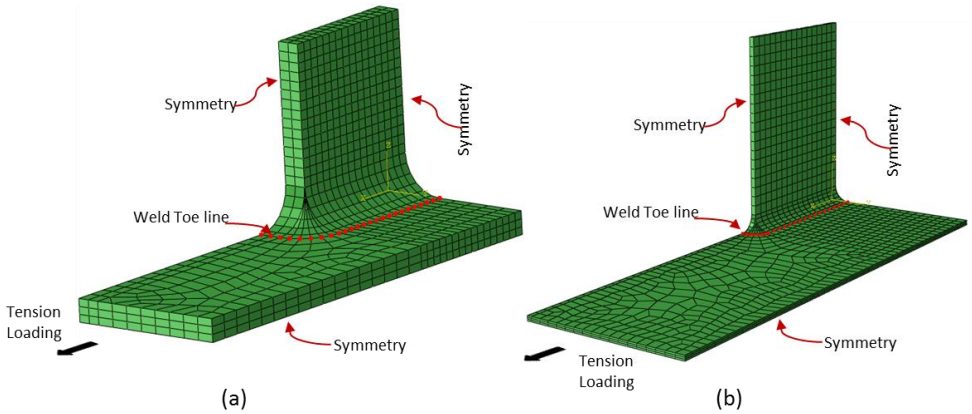

Figure 4.9: 3D solid FE models used for modeling longitudinal gusset joints: (a) 5mm base plate thickness; (b) 2mm base plate thickness

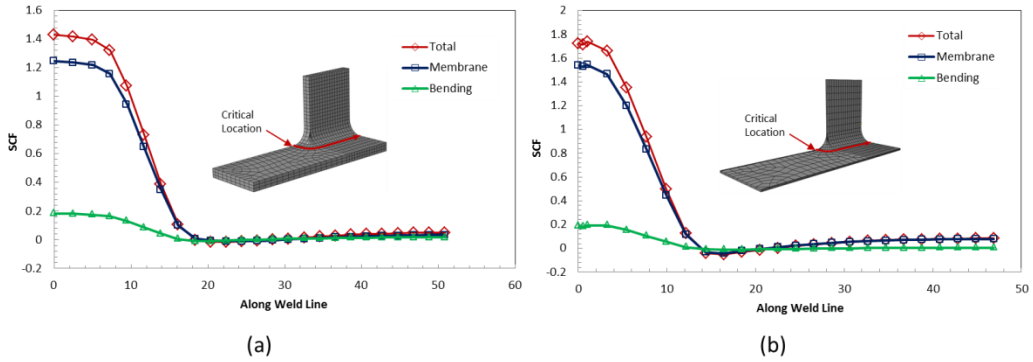

Figure 4.10: Stress concentration factor results along weld toe line in longitudinal gusset joints: (a) 10 mm base plate thickness; (b) 2mm base plate thickness

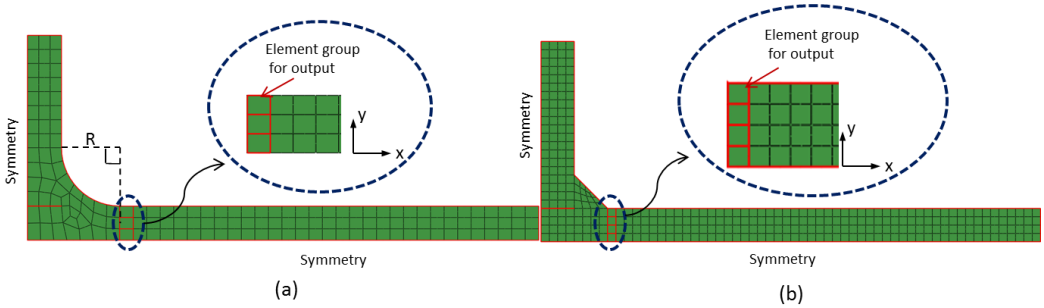

Figure 4.11: Cruciform fillet joints modeled as 2D plane strain models: (a) TIG welded cruciform joint; (b) MIG welded cruciform joint

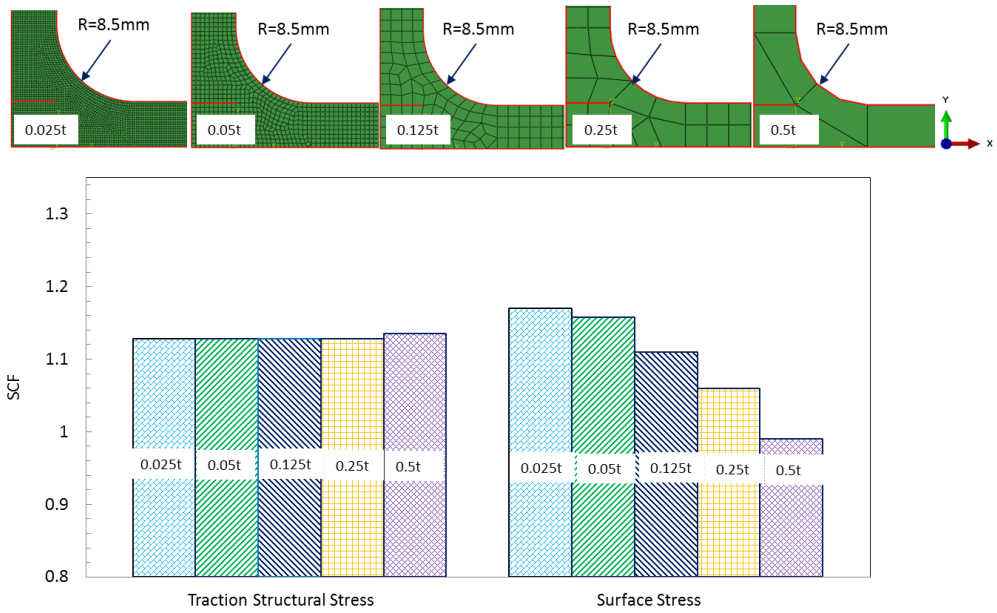

Figure 4.12: TIG weld SCF results obtained using FE models with different element size – traction structural stress results versus conventional FE-based surface stress results

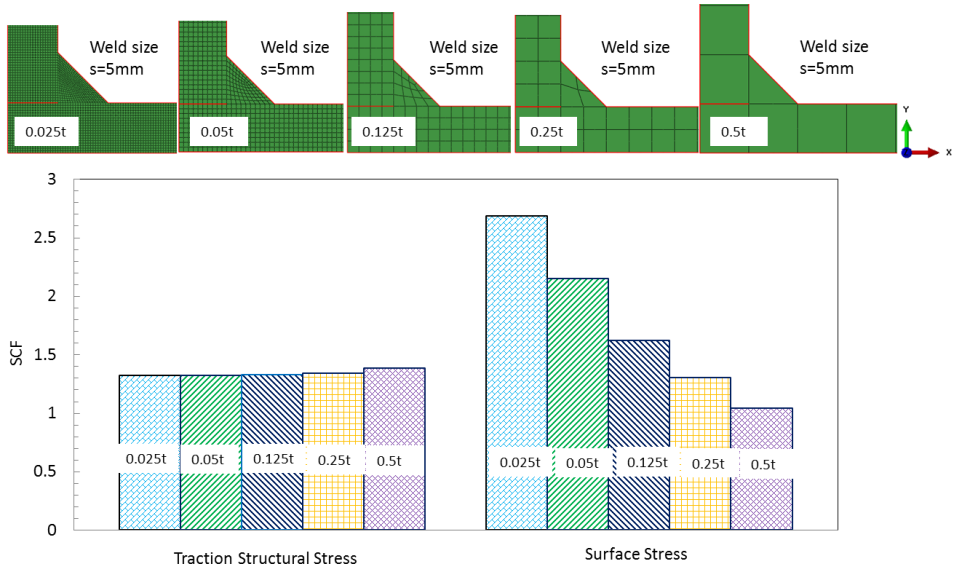

Figure 4.13: MIG weld SCF results obtained with FE models with different element size – traction structural stress results versus conventional FE-based surface stress results

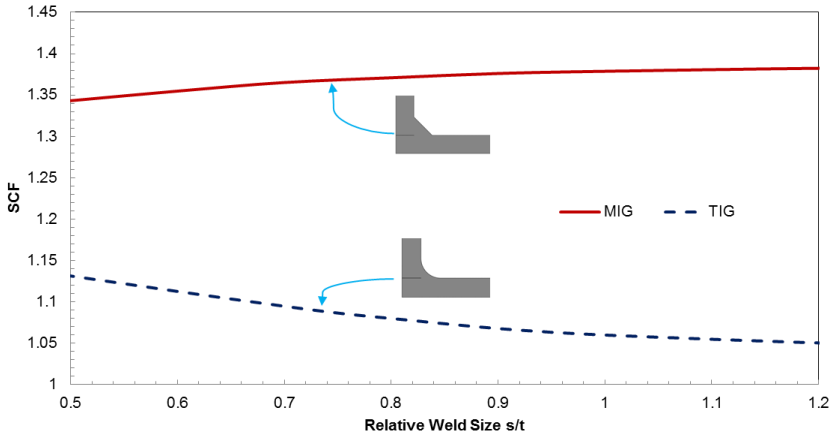

Figure 4.14: SCF as a function relative fillet weld size (s/t)

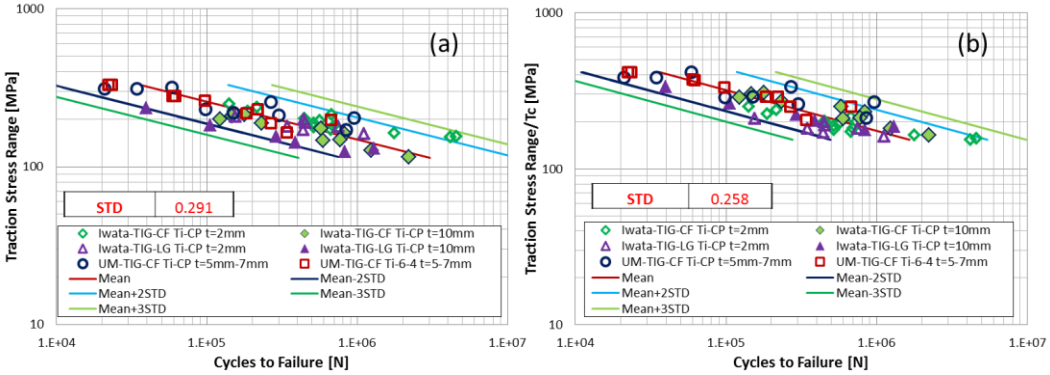

Figure 4.15: TIG weldment fatigue test data presented using different stress range definitions: (a) traction stress range; (b) thickness-corrected traction stress range

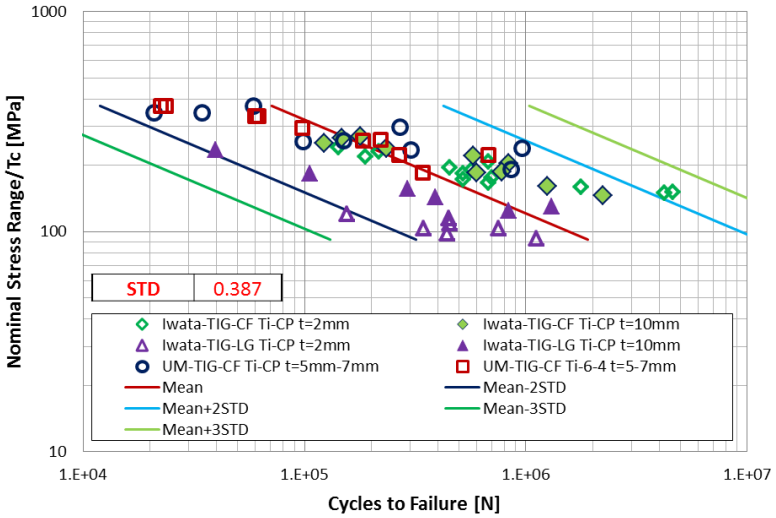

Figure 4.16: TIG weldment fatigue test data presented using thickness-corrected nominal stress range

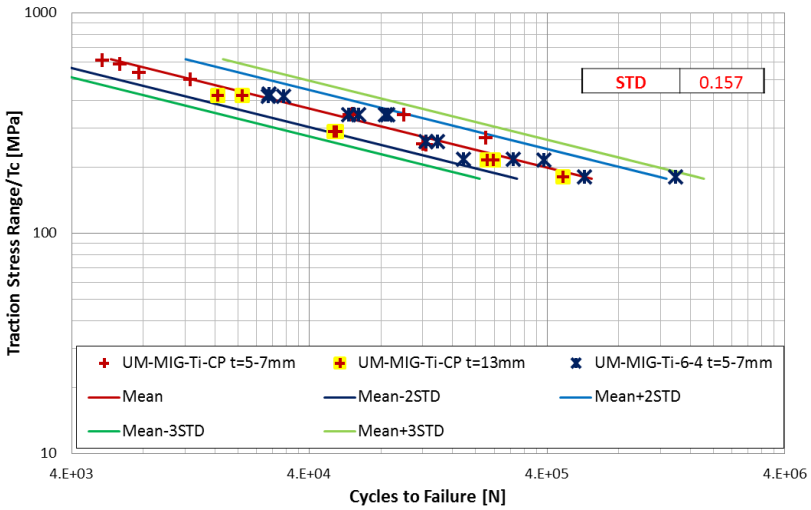

Figure 4.17: MIG weldment data correlation using the thickness-corrected traction stress range according to in Eq. (4.9)

Figure 4.18: Component configuration and fatigue testing conditions for welded titanium beams [13-14]: (a) as-welded I beam; (b) I-beam specimen mounted on fatigue test machine; (c) after final failure

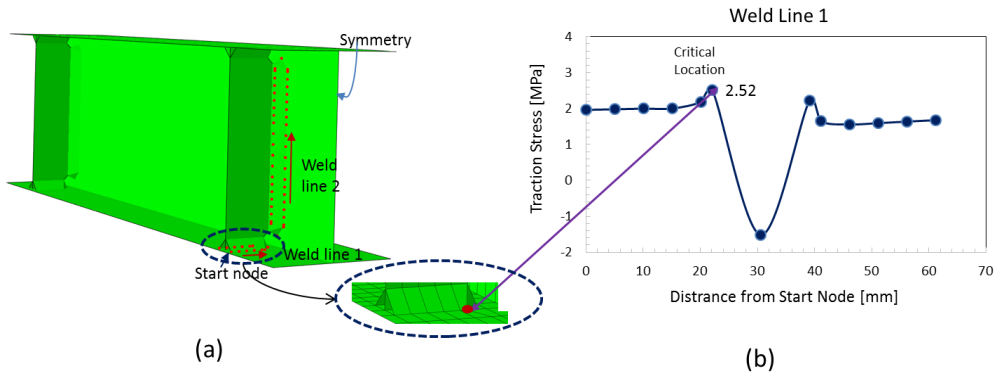

Figure 4.19: Finite element model (mesh not shown for clarity) and traction structural stress analysis results: (a) 3D linear shell model for B2 and B3; (b) normal traction stress distribution along Weld Line 1.

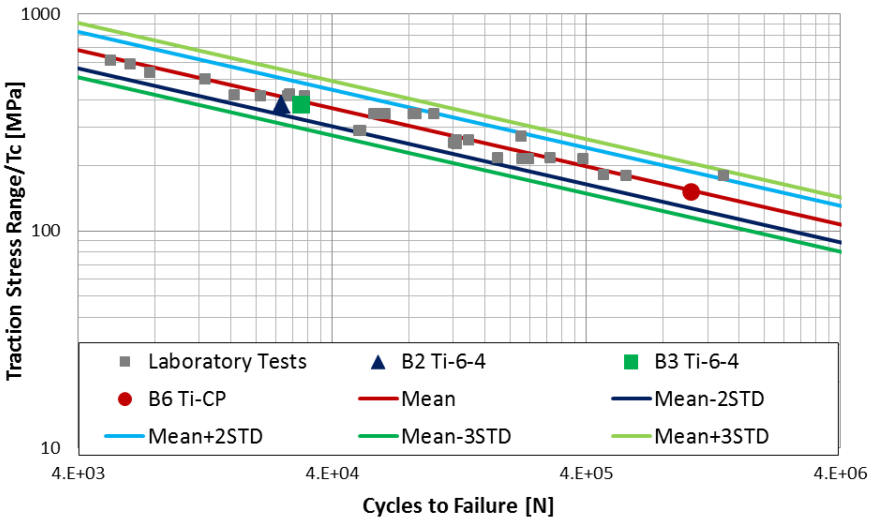

Figure 4.20: Correlation of structural component test data with proposed master S-N curve scatter band

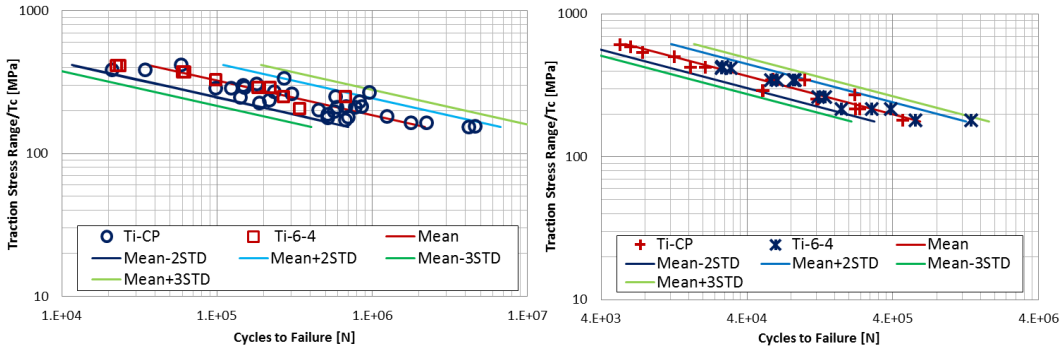

(a) (b)

Figure 4.21: Verification of base material effects on fatigue using all cruciform joint test data: (a) TIG weldment fatigue test data; (b) MIG weldment fatigue test data

ACKNOWELDGEMENTS

The authors gratefully acknowledge the support of this investigation in part by ONR Grant No. N00014-10-1-0479 and the National Research Foundation of Korea (NRF) Gant funded by the Korea government (MEST) through GCRC-SOP at University of Michigan under Project 2-1: Reliability and Strength Assessment of Core Parts and Material System.

References

[1] Boyer, R. R. "An overview on the use of titanium in the aerospace industry." Materials Science and Engineering: A 213.1 (1996): 103-114.
[2] Baxter, Carl, Sitham Pillai, and Graham Hutt. "Advances in Titanium Risers for FPSO's." Offshore Technology Conference. Offshore Technology Conference, 1997.
[3] Salama, Mamdouh M., Jagannathan Murali, and Mike W. Joosten. "Titanium drilling risers—application and qualification." Journal of Offshore Mechanics and Arctic Engineering 122.1 (2000): 47-51.
[4] Berge, Stig, Oddvar I. Eide, and Philippe Main ̧on. "Fatigue Strength of Titanium Riser Welds." Effect of Materials Grade and Weld Method, 21 “International Conference on Offshore Mechanics and Arctic Engineering, OMAE2002-28576. 2002.
[5] Berge, S. "Fatigue strength of Titanium risers: effect of defects." OMAE 1998: 17th International Conference on Offshore Mechanics and Arctic Engineering. 1998.
[6] Berge, Stig, Philippe Main ̧on, and Mons Hauge. "Fatigue of 28-inch Titanium Riser: SN Data and Defect Assessment." ASME 2002 21st International Conference on Offshore Mechanics and Arctic Engineering. American Society of Mechanical Engineers, 2002.
[7] Salama, Mamdouh M. "Fatigue crack growth behavior of titanium alloy Ti-6Al-4V and weldment." Journal of Offshore Mechanics and Arctic Engineering123.3 (2001): 141-146.
[8] British Standard, B. S. "7910." Guide on methods for assessing the acceptability of flaws in metallic structures (2005).
[9] Dong, P., et al. "A Math-Based Design-for-Produceability Evaluation of Titanium Applications in Ship Hull Structures." (2012).
[10] Iwata, T., and K. Matsuoka. "Fatigue strength of CP Grade 2 Titanium fillet welded joint for ship structure." Welding in the World 48.7-8 (2004): 40-47.
[11] BSL, KS. "7608--1993 Code of Practice for Fatigue Design and Assessment of Steel Structures." (1995).
[12] AWS, D1. "9/D1. 9 M." Structural Welding Code—Titanium (2007).
[13] Patnaik, Anil, et al. "Investigating and Understanding the Fatigue Response and Failure of Built-Up Welded Beams of a Titanium Alloy." Fatigue of Materials: Advances and Emergences in Understanding (2010): 195-215.

[14] Patnaik, Anil, et al. "The Fatigue Behavior of Built-Up Welded Beams of Commercially Pure Titanium." Journal of materials engineering and performance 20.7 (2011): 1247-1255.
[15] WS, B. (2007). 0: 2007. Standard methods for mechanical testing of welds, 67-71.
[16] Dong, P. "A robust structural stress method for fatigue analysis of offshore/marine structures." Journal of Offshore Mechanics and Arctic Engineering 127.1 (2005): 68-74.
[17] Dong, P., et al. "THE MASTER SN CURVE METHOD AN IMPLEMENTATION FOR FATIGUE EVALUATION OF WELDED COMPONENTS IN THE ASME B&PV CODE, SECTION VIII, DIVISION 2 AND API 579-1/ASME FFS-1." Welding Research Council Bulletin 523 (2010).
[18] ASME Boiler and Pressure Vessel Code, Section VIII, Division 2, 2007.
[19] Dong, P. "A structural stress definition and numerical implementation for fatigue analysis of welded joints." International Journal of Fatigue 23.10 (2001): 865-876.
[20] Dong, P., et al. "A structural strain method for low-cycle fatigue evaluation of welded components." International Journal of Pressure Vessels and Piping119 (2014): 39-51.
[21] Dong, P., and J. K. Hong. "The master SN curve approach to fatigue of piping and vessel welds." Welding in the World 48.1-2 (2004): 28-36.
[22] Xing, Shizhu, Pingsha Dong, and Alina Threstha. "Analysis of fatigue failure mode transition in load-carrying fillet-welded connections." Marine Structures46 (2016): 102-126.
[23] Dong, P., and J. Hong. "A robust structural stress parameter for evaluation of multiaxial fatigue of weldments." Fatigue and Fracture Mechanics: 35th Volume. ASTM International, 2007.
[24] Wei, Zhigang, and Pingsha Dong. "Multiaxial fatigue life assessment of welded structures." Engineering Fracture Mechanics 77.15 (2010): 3011-3021.
[25] AQualifications, A. S. S. W. Qualify procedures and personnel according to AWS D1. 1/D1. 1M,". Structural Welding Code-Steel, 6122, 051200-3.
[26] ABAQUS, 2012, User's Manual, Version 6.12
[27] Lazzarin, P., and P. Livieri. "Notch stress intensity factors and fatigue strength of aluminium and steel welded joints." International Journal of Fatigue 23.3 (2001): 225-232.
[28] Fricke, Wolfgang. "Recommended hot-spot analysis procedure for structural details of ships and FPSOs based on round-robin FE analyses." International Journal of Offshore and Polar Engineering 12.01 (2002).
[29] Gurney, Timothy Russell. Fatigue of welded structures. CUP Archive, 1979.
[30] Maddox, Stephen John. Fatigue strength of welded structures. Woodhead publishing, 1991.
[31] Dong, P., J. K. Hong, and Z. Cao. "Stresses and stress intensities at notches:'anomalous crack growth'revisited." International journal of fatigue25.9 (2003): 811-825.
[32] Dong, P., J. K. Hong, and Z. Cao. "A Robust K Estimation Scheme Using Mesh-Insensitive Structural Stresses." Welding in the World 48.5-6 (2004): 28-38.
[33] Tada, H., Paris, P.C., Irwin, G.R. "The Stress Analysis of Cracks Handbook", 2nd ed., Paris Productions Incorporated, St. Louis, Missouri, 1985

Chapter 5
Discussion

In Chap 2, we start with the examination of two plausible fatigue failure mode transition criteria: one in terms of an effective traction stress (ETS) combining both weld throat normal and shear stress components (see Eq.(2.14)) and the other in terms of a corrected ETS parameter by introducing both size- (i.e., plate thickness) and stress-state related parameters through fracture mechanics considerations (see Eq. (2.17)). Under ideal fillet weld geometric conditions, i.e., without counting weld penetration and joint misalignments, both criteria seem to provide a reasonable estimate of fatigue failure mode transition region with the former being simpler to use and the latter being more conservative with test data. In order to better understand the test data, particularly data scatter observed, it is found that both weld penetration and joint misalignment must be adequately taken into account. Although both effects on failure mode transition have been discussed in the literature to some extent, such as the investigations by Jakubczak and Glinka [1] and Andrew [2], a lack of a consistent analytical treatment on both weld throat and weld toe stress states have been a major hurdle for establishing an effective failure mode transition criterion. As reported in Chap 2, weld penetration can be directly incorporated into the analytical weld throat stress model developed. A new set of comprehensive analytical solutions for various joint misalignments and boundary conditions are given in Chap 3. Both new developments should enable a more reliable determination of failure mode transition from weld root cracking to weld toe cracking,

which will be discussed next.

5.1 Effects of Weld Penetration and Joint Misalignments

Based on the measurements on load carrying steel specimens presented in Chap. 2 and 3, all the fatigue test data shown in Figure 2.23 should contain a certain amount of coupled weld penetration and joint misalignments. Then, the individual effect of weld penetration and joint misalignments can't be identified. To experimentally validate the individual effect of weld penetration or joint misalignments, a unique experimental study is carried out [3] recently. All test specimens are fabricated as load-carrying cruciform joints using aluminum alloys (AL7N01). Base plate thicknesses vary from 8*mm* to 22*mm*. The fundamental testing procedures are the same as steel fatigue testing presented in Sec. 2.4 except load ratio $R=0.1$ instead of $R=-1$. The uniqueness of this testing is that the weld penetration is precisely controlled by using EDM drilling and WEDM cutting. The cruciform specimens are initially fabricated with full penetration. Then, the interface of the intercostal plate and the continuous plate is cut open with the desired size through EDM drilling and WEDM cutting. It should be noted that both axial and angular misalignments of each specimen are measured and recorded before cutting. Those specimens with greater joint misalignments will be cut with a size equal to intercostal plate thickness t i.e. without penetration remaining. Furthermore, the specimens containing minimum joint misalignments are cut with various cutting sizes to investigate penetration effect. By doing so, the weld penetration and joint misalignments can be successfully decoupled.

5.1.1 Weld Penetration

Figure 5.1a shows a specimen (B7-3) with weld size $s/t \approx 0.9$ and a cut size

$t = 10mm$ i.e. without weld penetration $p/t = 0$. A weld root cracking mode was developed as illustrated in Figure 5.1b. While Figure 5.1c shows a specimen (B7-5 $s/t \approx 0.9$) with greater penetration $p/t = 0.2$, it failed at weld toe (see Figure 5.1d). This experimental evidence confirms that weld penetration indeed influences failure mode transition.

5.1.2 Joint Misalignments

In Chap. 3, it has been shown that both axial and angular misalignments significantly influence the stresses associated to weld toe cracking (see Figure 3.12). However, the misalignment effect on weld root cracking mode has not been investigated. Using the same two specimens shown in Figure 3.11, the weld throat stresses at the angular section $\theta = 90^\circ$ are computed based on finite element method. The results are illustrated in Figure 5.2 along with weld toe stresses for comparison purpose. As seen, the misalignments have a negligible contribution to stress state relevant to weld root cracking for both 5*mm* and 10*mm* thick specimens (Figure 3.11). This suggests that joint misalignments will influence the fatigue failure mode transition behavior.

Figure 5.3a shows a specimen (B4-4 $s/t \approx 1.0$) with minimum measured axial misalignment $e/t \approx 0$ and angular misalignment $\alpha \approx 0^\circ$, and a weld root cracking was developed (see Figure 5.3b). Figure 5.3c shows a specimen (B4-6 $s/t \approx 1.0$) containing greater misalignments $e/t \approx 0.1$ and $\alpha \approx 1^\circ$, which developed a weld toe crack (see Figure 5.3d). This experimental evidence confirms that joint misalignments indeed influence the fatigue failure mode transition.

5.1.3 Ideal Failure Mode Transition Behavior

Excluding those specimens influenced by designed weld penetration and greater joint misalignments, the rest of specimens can be treated as an ideal condition. Then, all

the "ideal" data are plotted as scaled fatigue lives versus relative weld size *s/t* (see Figure 5.4) along with the EETS based critical weld size at $s/t \approx 1.16$ without counting weld penetration and joint misalignments or referred to as idealized critical weld size. Comparing Figure 5.4 to Figure 2.23, failure mode transition region as exhibited in Figure 2.23 does no longer exist. The idealized critical weld size $s/t \approx 1.16$ seems like an absolute cutting point of weld root cracking mode and weld toe cracking mode. From this point of view, the fatigue failure mode transition behavior shown in Figure 2.23 should be contributed to both weld penetration and joint misalignments.

5.1.4 Theoretical Critical Weld Size Incorporating Penetration and Misalignments

According to misalignment measurements listed in Table 3B- 1, the averaged axial misalignment (e/t) is obtained as $e/t = 0.11$, and averaged angular misalignment is 0.8°. Then, the average misalignment-induced stresses can be evaluated using Eqs. (3.31) and (3.33). With misalignment-induced stresses involved, the EETS relevant to weld toe cracking (see Figure 2.14b) will be elevated. Furthermore, according to the weld penetration measurements presented in Sec. 2.4.1, it is reasonable to estimate an averaged weld penetration as $p/t = 0.1$ for all tested specimens as an average of the upper bound $p/t = 0.2$ and lower bound $p/t = 0$. Then, a theoretical critical weld size incorporating weld penetration and joint misalignments is determined at $s/t \approx 0.78$ as illustrated in Figure 5.5 along with the idealized critical weld size $s/t \approx 1.16$. As seen, the critical weld size is reduced to $s/t \approx 0.78$ as a result of considering actual weld penetration and misalignments, comparing to idealized critical weld size $s/t \approx 1.16$. A validation will be performed, in what follows, by statistical analysis of the test data presented in Figure 2.23.

5.2 Statistical Analysis of Fatigue Test Data

5.2.1 Fatigue Life Based Critical Weld Size Determination

With all EETS based SCFs available in Figure 2.14, the S-N curves for both weld root cracking and weld toe cracking can be readily constructed. Figure 5.6 Show all weld toe cracking data in terms of EETS calculated by multiplying the SCFs ($p/t=0$ see Figure 2.14b) with applied nominal stress range. Figure 5.7 shows all weld root cracking data using maximum EETS calculated by multiplying the SCFs ($p/t=0$ see Figure 2.14b) with applied nominal stress range. It is worth noting that using SCF curves with respect to $p/t=0$ is to present the test data in as-tested condition to facilitate critical weld size calculation.

With both weld toe and root cracking S-N curves constructed, the fatigue failure mode transition point i.e. critical weld size can be determined by equating the two S-N mean curves shown in Figure 5.6 and Figure 5.7. Instead of solving a complex exponential equation (S-N curves), an alternative way is to explicitly seek the intersection point of the two fatigue life ratio curves below:

$$\frac{N^B}{N^A} \le 1 \tag{5.1}$$

$$\frac{N^A}{N^B} \le 1 \tag{5.2}$$

where N^A and N^B represent fatigue lives of weld toe cracking (Mode A) and weld root cracking (Mode B) respectively.

As seen in Figure 5.8, the critical weld size i.e. the intersection point of the two fatigue life ratio curves Eqs. (5.1) and (5.2) is determined at $s/t \approx 0.76$, which is very

close to the theoretical critical weld size $s/t \approx 0.78$ by incorporating weld penetration and joint misalignments (see Figure 5.8). This further confirmes the weld penetration and joint misalignment effect and the effectiveness of the analytical method on failure mode transition analysis proposed in Chap. 2.

For visualizing the determined critical weld sizes along with test data, all fatigue data scaled by a factor *f* defined in Eq. (2.22) are plotted in terms of relative weld size *s/t* (see Figure 5.9). As seen, the EETS based ideal critical weld size $s/t \approx 1.16$ is definitely conservative, beyond which no any test failed at weld root, since every data point in Figure 5.9 contains a certain amount of weld penetration and misalignments. The actual critical weld size $s/t \approx 0.76$ seems to reasonably divide the whole data set into weld root cracking dominant region (on the left) and weld toe cracking dominant region (on the right). However, from a design point of view, assuming ideal critical size $s/t \approx 1.16$ as design reference will result in the over-sized weld, which may cause more severe welding induced distortion [4], however using actual transition point $s/t \approx 0.76$ can only give a 50% chance to prevent weld root cracking. Such a dilemma will be dealt with in next section.

5.2.2 Logistic Regression

Each load-carrying fillet welded connection is statistically possible to develop a fatigue crack either at weld toe or at weld root due to various inherent variabilities such as penetration status, misalignments, and weld quality etc. The possibility of each cracking mode is highly related to relative weld size *s/t* as observed in Figure 5.9. Since two failure modes, either weld throat or weld toe cracking, a logistic regression analysis method for analyzing problems with binary outcome [5] should offer another perspective

on the interpretation of the failure mode transition behavior as seen in Figure 5.9.

For the present application, all data in Figure 5.9 are considered as independent observations of variable pairs (x_i, y_i), $i=1, 2, \ldots, n$, where y_i denotes a binary outcome variable, and x_i is the independent variable representing relative weld size *s/t*, corresponding to i^{th} observation in a given data population. The binary outcome variable y_i takes a value of either 0 or 1, representing weld root cracking or weld toe cracking mode, respectively. Then, a logistic regression model can be constructed in the following form [6]:

$$\ln\left(\frac{p\left(\frac{s}{t}\right)}{1-p\left(\frac{s}{t}\right)}\right)=\beta_0+\beta\cdot\frac{s}{t} \tag{5.3}$$

where, $p\left(\frac{s}{t}\right)$ and $1-p\left(\frac{s}{t}\right)$ represent the probabilities of weld toe cracking and weld root cracking, respectively, as a function of independent variable i.e. relative weld size *s/t*. Parameters β_0 and β are to be determined through a curve-fitting process to be discussed next. From Eq. (5.3), the probability of weld toe failure can be expressed as follows:

$$p\left(\frac{s}{t}\right)=\frac{1}{1+e^{-(\beta_0+\beta\cdot\frac{s}{t})}} \tag{5.4}$$

the corresponding conditional likelihood function [6] of the whole dataset shown in Figure 5.9 can be constructed as the product of the probability of each test outcome corresponding to either weld toe cracking, i.e., $p\left(\frac{s}{t}\right)$ or weld root cracking, i.e.,

$1-p\left(\frac{s}{t}\right)$:

$$L(\beta_0, \beta) = \prod_{i=1}^{n} p\left(\frac{s}{t}\right)^{y_i} \left(1-p\left(\frac{s}{t}\right)\right)^{1-y_i} \tag{5.5}$$

By introducing the maximum likelihood method [6], i.e., finding coefficients β_0 and β that maximizes the conditional likelihood function in Eq.(5.5), the two coefficients β_0 and β were determined as $\beta_0 = -14.436$ and $\beta = 18.573$. Then, the probability of weld toe failure can be estimated using Eq. (5.4) for any relative weld size (*s/t*), as graphically presented in Figure 5.10. The corresponding weld throat failure probability $1-p\left(\frac{s}{t}\right)$ is also presented in Figure 5.10 for illustration purpose.

The two vertical dash lines (in Figure 5.10) show both 50% and 95% chance for developing weld toe failure when relative weld size exceeds $s/t \approx 0.78$ and $s/t \approx 0.93$ Note that $s/t \approx 0.78$ at 50% confidence level agrees well with the actual critical weld sizes $s/t \approx 0.76$ and theoretical critical weld size $s/t \approx 0.78$ with considering actual specimen conditions. A critical weld size of $s/t \approx 0.93$ at 95% confidence level from logistic analysis results (Figure 5.10) seems conservative enough for design consideration.

5.3 Aluminum Alloys versus Steels

In this study, all theoretical developments, such as weld throat stress solution, fatigue failure mode transition criterion, and misalignment-induced SCF solutions are solely dependent on joint geometry, and independent of materials. It is worth validating it

by test data in different materials.

A large amount of load-carrying cruciform specimens made of aluminum alloys (AL6082) has been tested for investigation of fatigue failure mode transition behavior. The specimen dimensions and testing procedures are all the same as steel specimens as presented in Chap. 2. The base plate and attachment plate are of the same thicknesses (5*mm* and 10*mm*). A representative weld toe (Mode A) failure is illustrated in Figure 5.11a, and weld root (Mode B) failure is shown in Figure 5.11b.

All aluminum test results are then plotted as scaled fatigue lives versus relative weld size *s/t* (see Figure 5.12). As seen, the fatigue failure mode transition behavior is rather similar to steels, comparing to Figure 5.9. The EETS based ideal critical weld size $s/t \approx 1.16$ is still definitely conservative for aluminum alloys. The design reference $s/t \approx 0.93$ proposed based on steel data is also valid for aluminum fillet joints as well.

5.4 Titanium Alloys

In Chap. 4, the fatigue behavior of welded titanium components has been investigated. As a result, the base materials have a negligible effect, and traction based stress parameter is very effective for correlating titanium test data. This suggests the fatigue failure mode transition criteria developed in this study would be also valid for titanium alloys. However, it should be noted that the extension application has to be restricted on MIG welded titanium fillet joints since all the developments on failure mode transition are based on MIG shape weld. It has been noticed that the smooth TIG weld shape significantly reduces the stress concentration at weld toe position (see Figure 4.14). Furthermore, the sharp notch still exists at weld root considering a load-carrying fillet welded joint. Then, the fatigue failure mode transition behavior of TIG welded fillet

joints would be dramatically different from MIG welded fillet joints. This will be investigated in the future study.

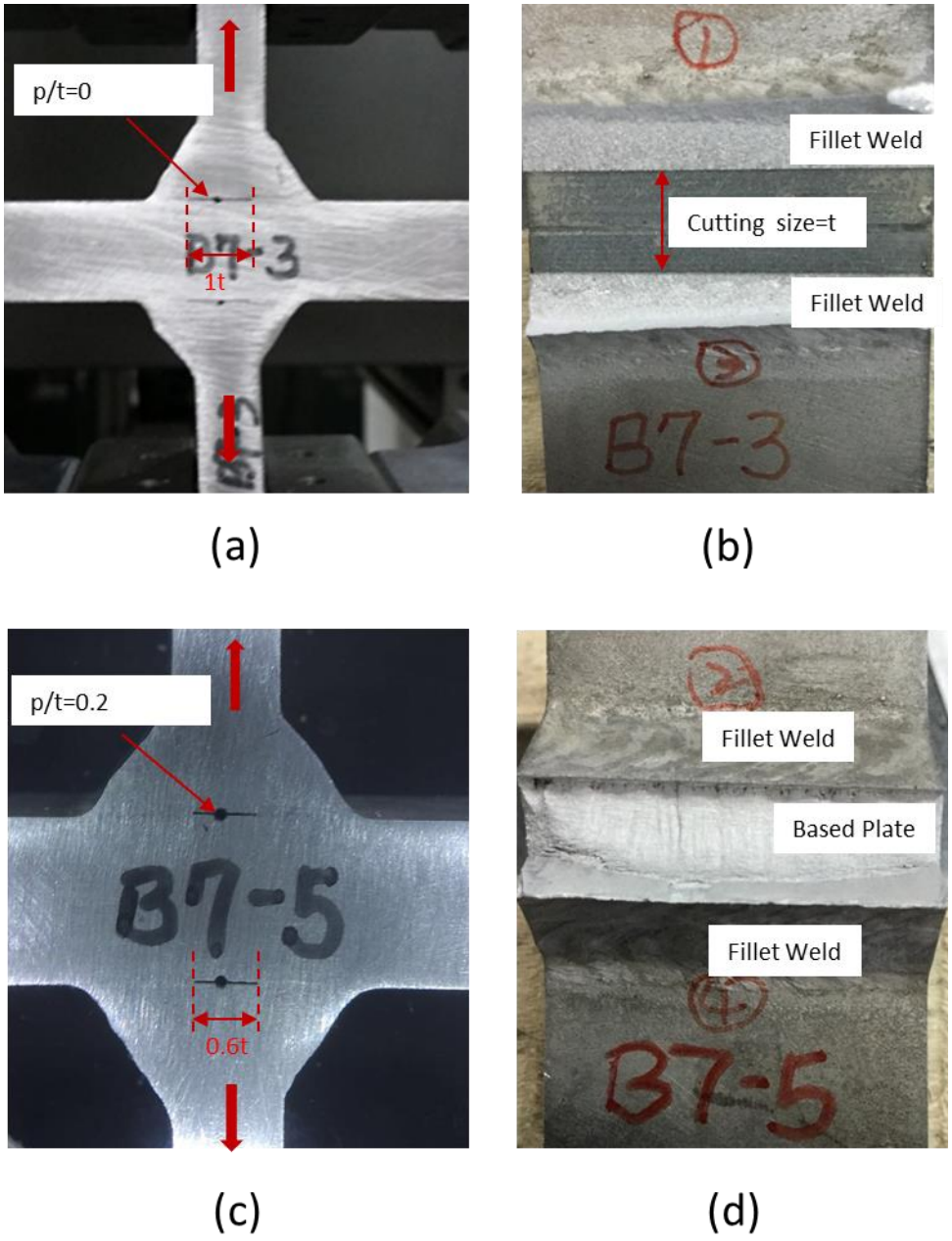

Figure 5.1: weld penetration effect: (a) specimen without weld penetration; (b) the specimen shown in Figure 5.1a failed at weld root; (c) specimen with greater penetration $p/t = 0.2$; (d) the specimen shown in Figure 5.1c failed at weld toe

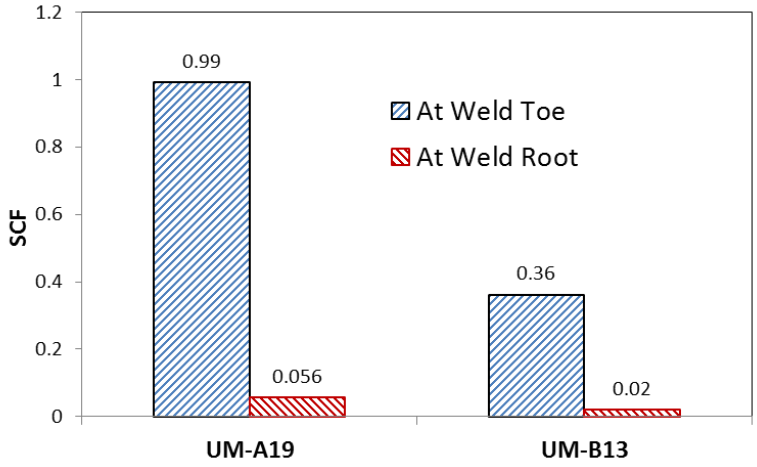

Figure 5.2: Comparison of misalignment-induced SCF associated to weld toe and root cracking modes respectively

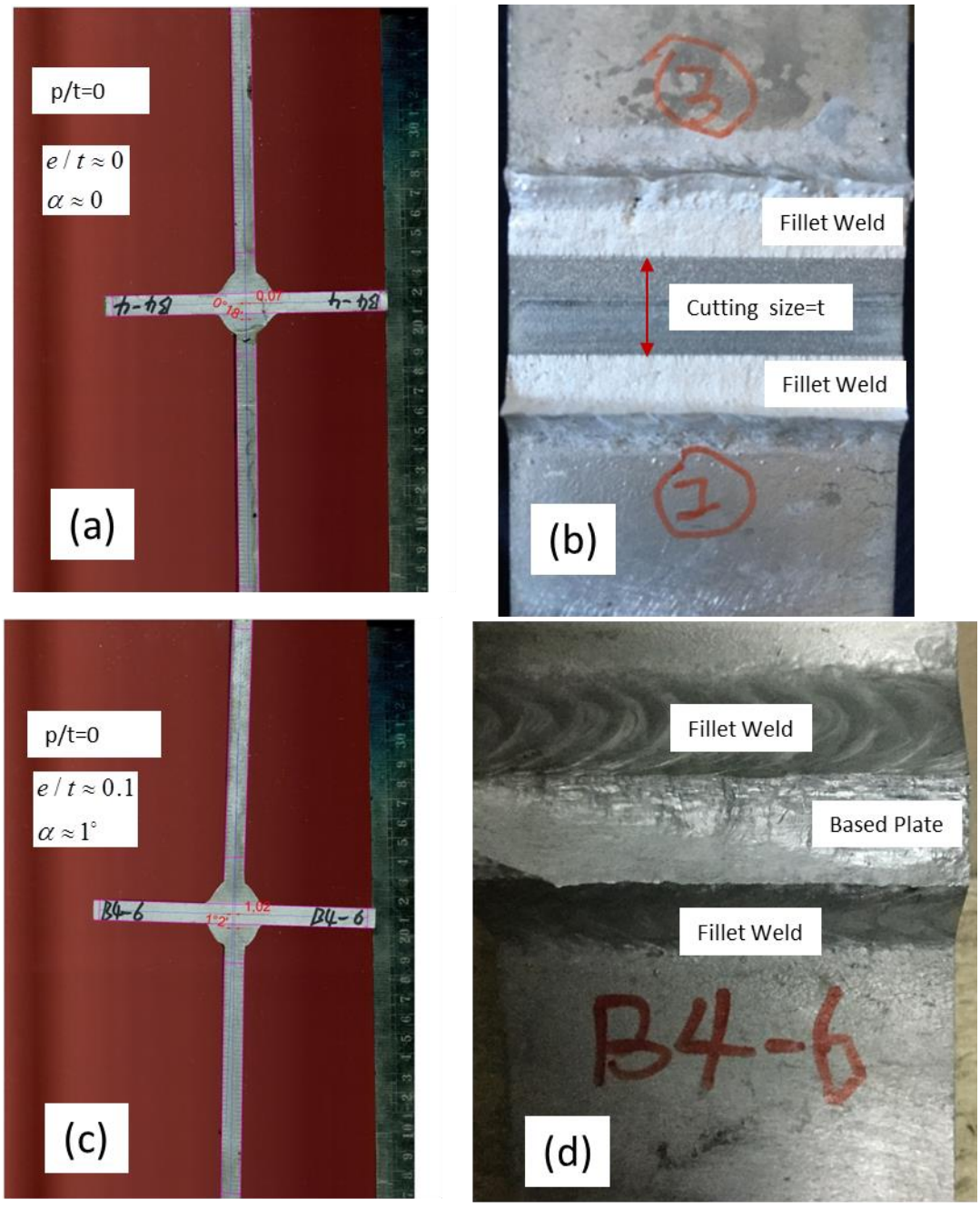

Figure 5.3: joint misalignment effect: (a) specimen with minimum joint misalignments; (b) the specimen shown in Figure 5.3a failed at weld root; (c) specimen with greater joint misalignments; (d) the specimen shown in Figure 5.3c failed at weld toe

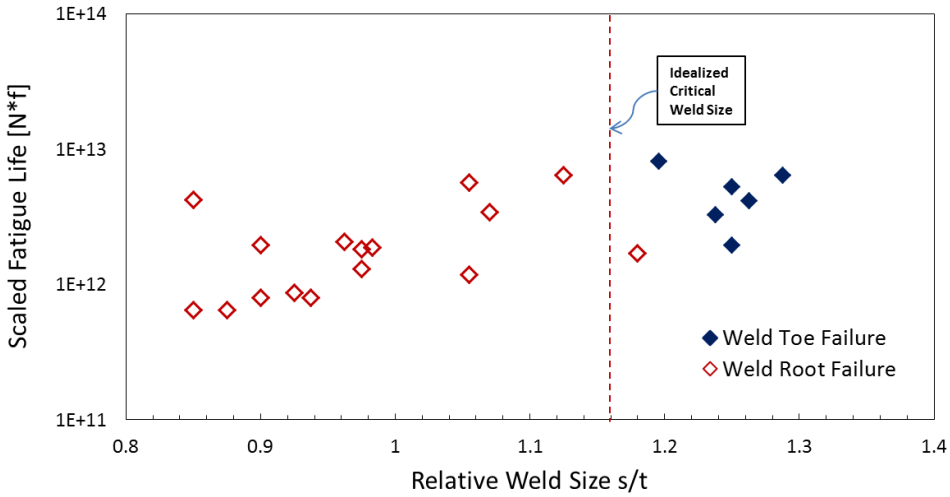

Figure 5.4: Critical weld size of test data treated as ideal condition

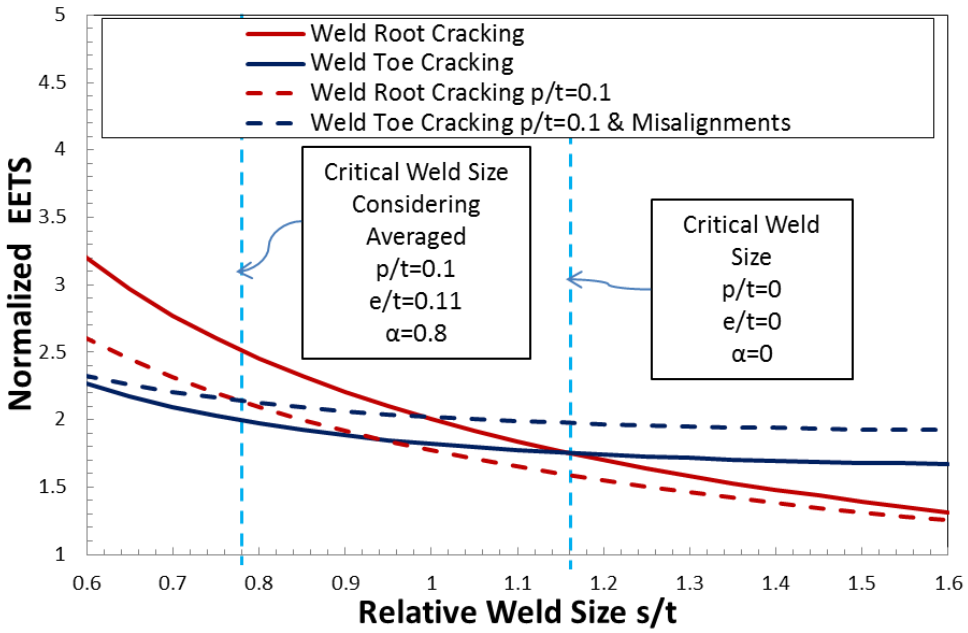

Figure 5.5: Critical weld size determination considering weld penetration and misalignments

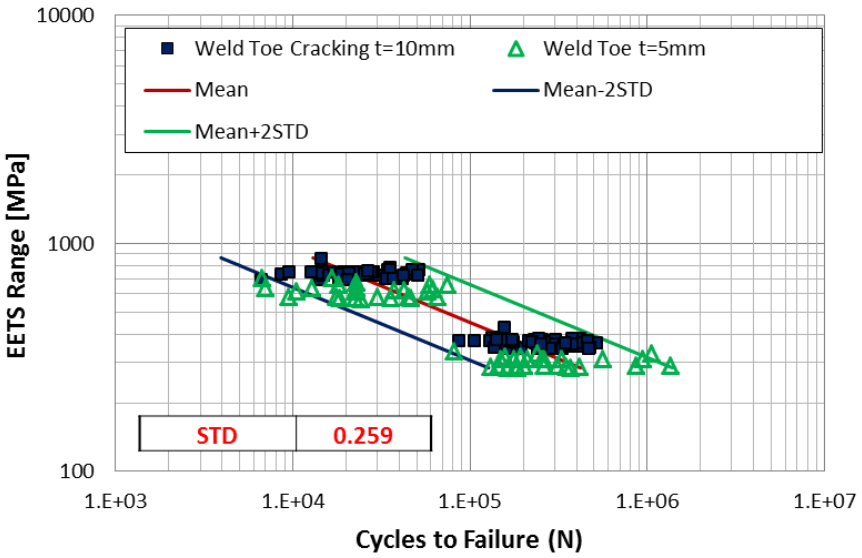

Figure 5.6: Weld toe cracking S-N curves

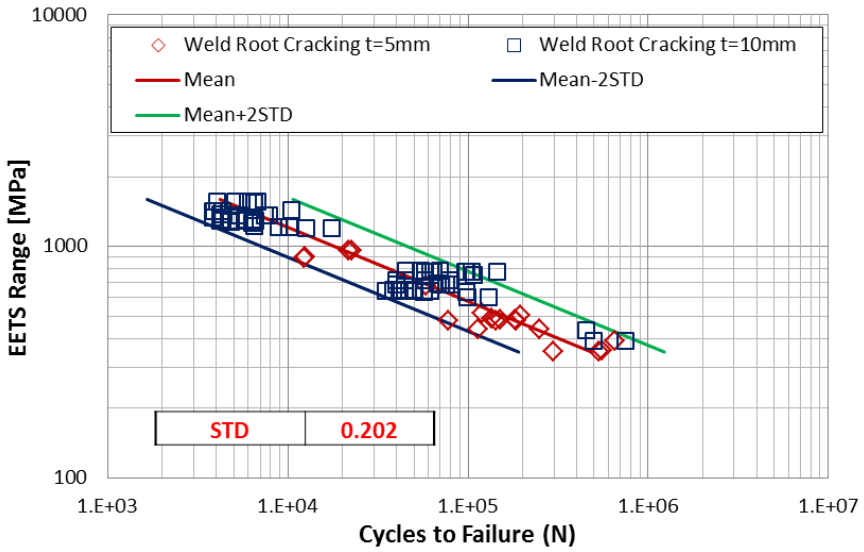

Figure 5.7: Weld root cracking S-N curves

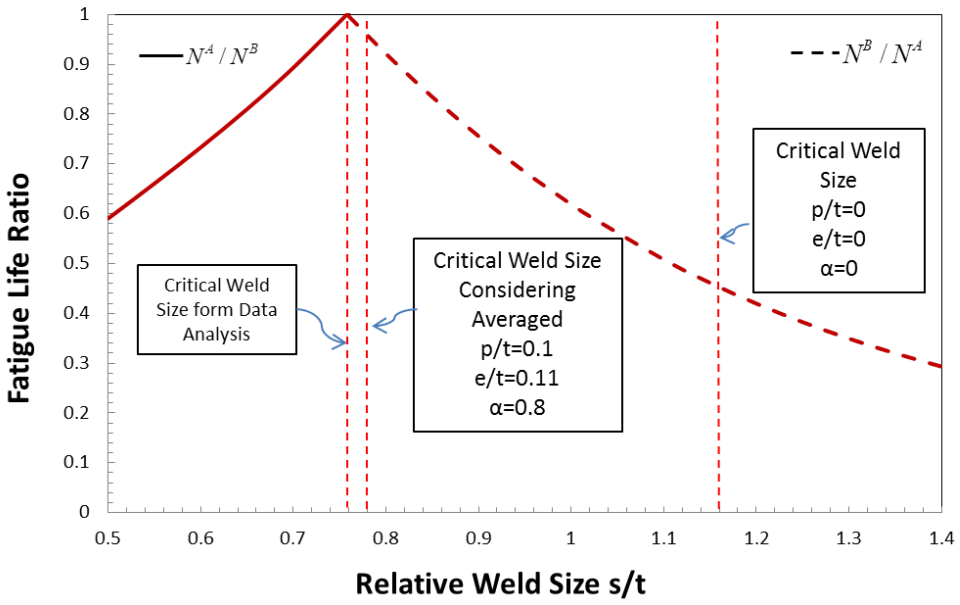

Figure 5.8: Critical weld size obtained from actual test data along with theoretical critical weld sizes

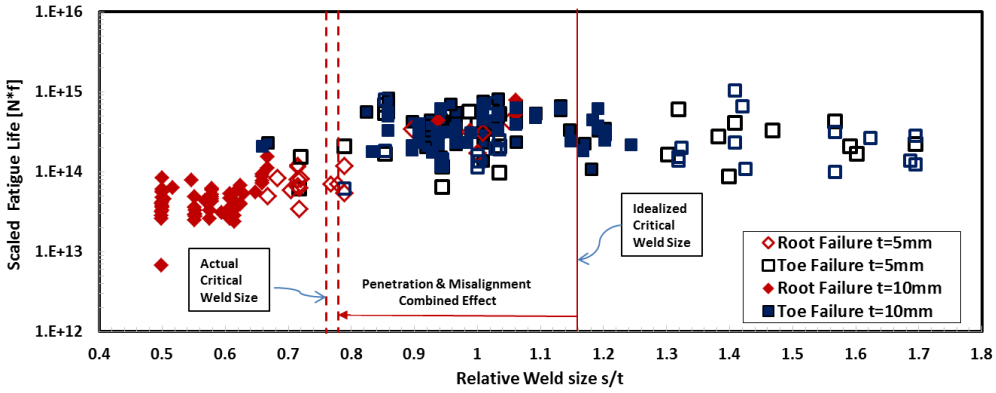

Figure 5.9: Scaled fatigue lives versus relative weld size

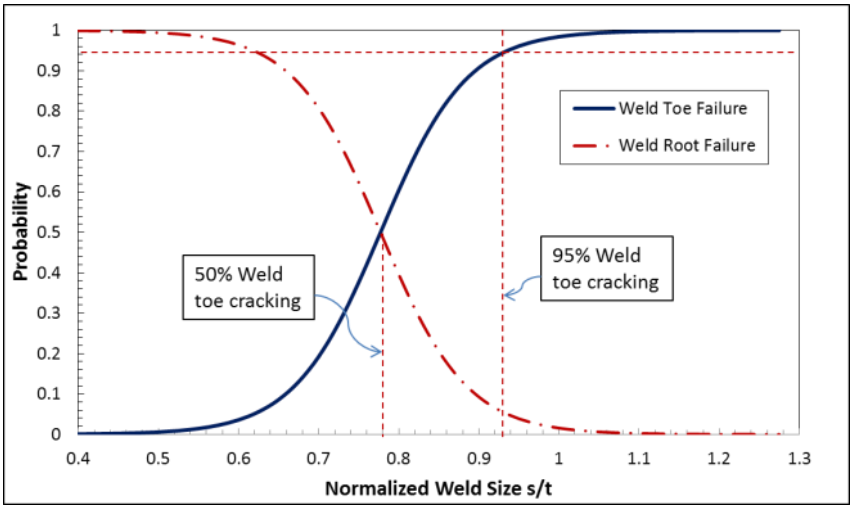

Figure 5.10: Probabilities of weld toe cracking and root cracking versus weld size

(a) (b)

Figure 5.11: Representative failure modes observed from fatigue testing: (a) weld toe cracking (Mode A); (b) weld root cracking (Mode B)

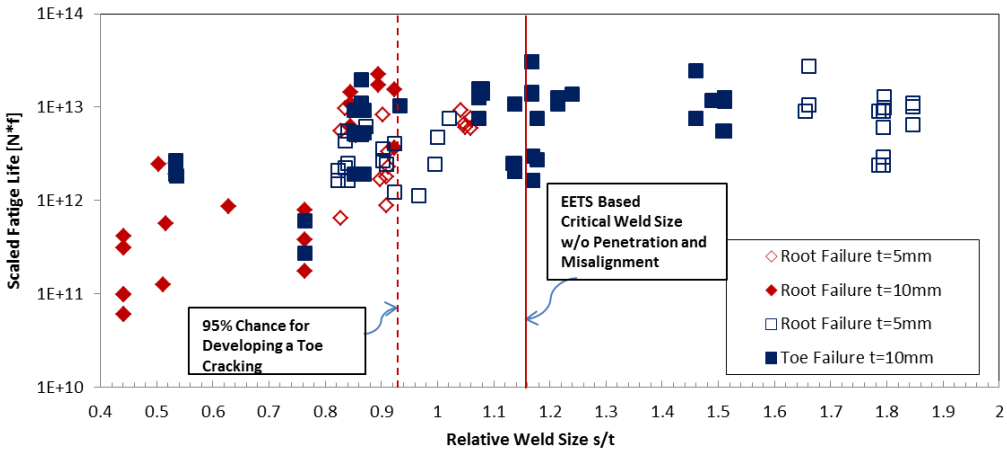

Figure 5.12: Scaled fatigue lives versus relative weld size

References

[1] Jakubczak, H., and G. Glinka. "Fatigue analysis of manufacturing defects in weldments." International journal of fatigue 8.2 (1986): 51-57.

[2] Andrews, R. M. "The effect of misalignment on the fatigue strength of welded cruciform joints." Fatigue & Fracture of Engineering Materials & Structures 19.6 (1996): 755-768.

[3] Wang P. et al. "Fatigue failure mode transition behavior in fillet welded connections in aluminum alloys". Under Preparation

[4] Huang, T. D., et al. "Reduction of Overwelding and Distortion for Naval Surface Combatants, Part 1: Optimized Weld Sizing for Lightweight Ship Structures." Journal of Ship Production and Design 30.4 (2014): 184-193.

[5] Mesa, Jos é Luis. "Understanding data in clinical research: a simple graphical display for plotting data (up to four independent variables) after binary logistic regression analysis." Medical hypotheses 62.2 (2004): 228-232.

[6] Hosmer Jr, David W., and Stanley Lemeshow. Applied logistic regression. John Wiley & Sons, 2004.

Chapter 6
Conclusions and Recommendations for Future Work

In this thesis, we have presented a systematic theoretical analysis and a comprehensive experimental study on fatigue failure mode transition behavior of load carrying fillet welded connections. In this chapter, all findings and analysis results are summarized as follows:

6.1 Theoretical Developments

A closed-form weld throat stress solution is developed based on traction based structural stress definition. Then, effective traction stress (ETS) and equivalent effective traction stress (EETS) based critical weld root cracking plane angle θ_c are precisely determined. It is then found that the critical plane angle θ_c (with respect to base plate) increases with increasing weld size (*s/t*) and penetration depth (*p/t*) according to both effective traction stress (ETS) (see Figure 2.9) and equivalent effective traction stress (EETS) based criteria (see Figure 2.13). The differences between the two criteria are insignificant, considering inherent variability in fatigue test data.

Two traction stress based failure mode transition criteria, i.e., ETS and EETS, are examined in detail and compared with a large number of test data involving failure mode transition from weld throat cracking to weld toe cracking as fillet weld size varies. As a result, the critical weld size and failure mode transition region when considering expected variations in weld penetration according ETS seem to provide a good estimation of the

lower bound transition behavior of actual test data, while those according to EETS seems to provide a good estimation of the upper bound, see Figure 2.23. Therefore, it is reasonably conservative to adopt the critical weld size according to the EETS based criterion, which gives a critical relative weld size of $s/t = 1.16$ with no penetration ($p/t = 0$) and $s/t = 0.85$ for an averaged relative penetration of $p/t = 0.2$.

The analytical developments presented in this work suggest that base plate thickness should not have any noticeable effects on failure mode transition behavior, as long as a relative fillet weld size (*s/t*) is used, unlike some of the previous studies suggest.

An analytical SCF calculation method is presented for treating misalignments in a general cruciform connection with its ends being subjected to maximum possible boundary constraints by means of a potential energy formulation. With such a solution method, a comprehensive set of analytical SCF solutions under various boundary conditions are obtained and validated by finite element solutions. These analytical SCF solutions cover a great deal of more geometric and boundary conditions of practical interest than what have been available to date. The analytical method is also applied for treatment of stress concentration development in fatigue specimens subjected to typical test conditions. As a result, the validity of the proposed analytical method has been further confirmed in its effectiveness in the interpretation of fatigue test data generated as a part of this study. Finally, with the aid of these new analytical solutions, both applicability and limitations of some of the existing SCF equations for treating joint misalignments such as those given in BS 7910 and DNV-RP-C203 are discussed.

6.2 Experimental Study

A comprehensive fatigue testing with a focus on lightweight applications for

surface combatants is performed, after a careful review of US Navy's existing fatigue design requirements and testing protocol. Load-carrying cruciform fillet-welded specimens are considered for investigating fatigue failure mode transition from weld root to weld toe cracking. The relative weld size *s/t* is arranged from 0.5 to 1.6, and base plate and attachment plate are of the same thicknesses (5*mm* and 10*mm*). A comprehensive analysis is performed based on this set of data, and the experimental findings are listed as follows:

- Taking advantage of the closed-form weld throat stress solution developed in Chap. 2 and analytical misalignment-induced SCF solutions developed in Chap. 3, a theoretical critical weld size is determined at $s/t = 0.78$ incorporating measured weld penetration and joint misalignments. It is much smaller than the ideal critical weld size $s/t = 1.16$ without weld penetration and joint misalignments involved.
- An experimental based critical weld size is captured at $s/t = 0.76$ through introducing fatigue life ratio curves. It is consistent with the theoretical critical weld size $s/t = 0.78$ determined by incorporating weld penetration and joint misalignment.
- Logistic regression analysis on the whole set of fatigue test data is performed to facilitate developing fillet weld sizing criterion. As a result, a statistical model is constructed, which can estimate a probability of developing weld toe cracking for a given fillet weld. One representative weld size $s/t = 0.78$ has 50% confidence for developing weld toe cracking, which is consistent with both fatigue life based critical weld size $s/t = 0.76$ and theoretical critical weld

size $s/t = 0.78$ considering typical shop floor conditions. The other representative one is $s/t = 0.93$ with respect to 95% chance for developing weld toe cracking mode.

To investigate fatigue failure mode transition behavior of other lightweight materials, a large amount of fatigue testing also is carried out using load carrying cruciform joints made of aluminum alloy (AL6082). Through a comparison between aluminum alloys and steels, it is found that fatigue behaviors are extremely similar (see Figure 5.12), which confirms that fatigue failure mode transition behavior of fillet welded connections is independent of materials.

A large number of fatigue tests on TIG and MIG welded cruciform joints made of Ti-CP (Grade 2) and Ti-6-4 (Grade 5) are carried out. Then, a new traction stress parameter with thickness correction is proposed for test data analysis. It is found that the proposed thickness-corrected traction stress parameter can be used to effectively correlate lab specimen test data in the form of a single S-N curve with a narrow scatter band regardless joint type and base late plate thickness, which has been demonstrated for both MIG and TIG weldment test data performed in this study and reported in the literature. The validity of the thickness-corrected traction stress parameter is then further confirmed by its ability in correlating full-scale structural component test data with lab specimen test data. Finally, with a detailed analysis focusing on base plate materials (TI-CP versus TI-6-4), it is found that both Ti-CP and Ti-6-4 data fall into essentially same scatter band in both TIG and MIG cases. This is consistent with historical observations on a large amount of steel weldment test data that have been used as a basis in well-known Codes and Standards. With the fundamental fatigue behavior obtained above, we can extend the

theoretical and experimental developments on fatigue failure mode transition to MIG welded titanium alloys. For TIG welded fillet joints, fatigue failure mode transition behavior remains to be investigated in the future study.

6.3 Proposed Fillet Weld Sizing Criterion

In conjunction with all theoretical and experimental findings and analysis results, a good understanding of fatigue failure mode transition behavior in fillet welded connections has been achieved. A set of quantitative fatigue based weld sizing criteria for preventing weld root fatigue cracking are recommended as follows:

- For fillet connections with idealized geometry and weld conditions, the EETS based ideal critical weld size s/t=1.16 should be met.
- For fillet connections with typical shop floor condition for lightweight ship construction, the relative weld size $s/t \approx 0.93$ should be met. However, while considering welding-induced distortion mitigation, the relative weld size $s/t \approx 0.78$ should be considered as a lower limit to assure the designed weld size situated in the weld toe cracking dominant regime.
- As weld penetration can be precisely controlled in fillet connection, the EETS based critical weld sizes (Figure 2.17) should be met with respect to the various status of weld penetration.

6.4 Recommendations for Future Work

6.4.1 Fatigue Failure Mode Transition

In this thesis, the fatigue failure mode transition criteria are developed by solely considering load carrying fillet connections under transverse tension loading. In the future, both remote bending and longitudinal shear loading should be considered. The

loading mode effect on both critical weld root cracking plane (angle) and failure mode transition point should be theoretically and experimentally investigated. Furthermore, the effect of weld bead shape such as TIG welds on failure mode transition should be investigated. TIG weld shapes can be readily investigated theoretically based on the closed-form solution developed in this thesis.

6.4.2 Misalignment-Induced Stress Concentration Factor

In this thesis, a generalized analytical solution method for calculating SCF resulted from joint misalignments has been developed. A comprehensive series of stress concentration factor solutions for the treatment of joint misalignment effects have been provided, which cover more boundary conditions than given in existing Codes and Standards (e.g., BS 7910, DNV-RP-C203, etc.). However, in practice, there will be additional combinations of boundary conditions at the ends of cruciform connections. The generalized analytical solution method has the capability to consider any permutations of boundary conditions. In the future, to facilitate both fitness for service assessment and fatigue design, robust tools will be developed for computing the misalignment-induced SCFs for any given cruciform structures with joint misalignments and boundary conditions. In addition, more quantitative misalignment acceptance criteria should be developed for construction of lightweight ship structures to ensure a minimum detrimental effect on fatigue performance.